NASA Contractor Report 3672

Synthesized Airfoil Data Method for Prediction of Dynamic Stall and Unsteady Airloads

Santu T. Gangwani

CONTRACT NAS1-16803
FEBRUARY 1983

NASA

NASA Contractor Report 3672

Synthesized Airfoil Data Method for Prediction of Dynamic Stall and Unsteady Airloads

Santu T. Gangwani
United Technologies Research Center
East Hartford, Connecticut

Prepared for
Langley Research Center
under Contract NAS1-16803

National Aeronautics
and Space Administration

**Scientific and Technical
Information Branch**

1983

Synthesized Airfoil Data Method for Prediction of Dynamic Stall and Unsteady Airloads

TABLE OF CONTENTS

TABLE OF CONTENTS (Cont'd)

Synthesized Airfoil Data Method for Prediction of Dynamic Stall and Unsteady Airloads

SUMMARY

A detailed analysis of dynamic stall experiments has led to a set of relatively compact analytical expressions, called synthesized unsteady airfoil data, which accurately describe in the time-domain the unsteady aerodynamic characteristics of stalled airfoils. Under the present study, an analytical research program was conducted to expand and improve this synthesized unsteady airfoil data method using additional available sets of unsteady airfoil data. The primary objectives were to reduce these data to synthesized form for use in rotor airload prediction analyses and to generalize the results. A secondary objective of the study was to apply the resulting empirical data to calculations of full-scale helicopter blade loads and stresses.

The synthesized unsteady airfoil data method is based on a relatively simple semi-empirical formulation, involving a compact set of dynamic parameters, which accurately predicts the unsteady aerodynamic coefficients of airfoils during dynamic stall. One of the main features of the formulation is that it adequately accounts for the effects of the formation and streamwise movement of the vortex shed from the airfoil leading edge during dynamic stall. It has been shown that the synthesized unsteady lift, drag, and pitching moment hysteresis loops compare well with the two-dimensional test data. Based upon this formulation, a new method has been developed to determine the unsteady aerodynamic loading acting on rotor blades operating both below and in stall. The effects of azimuthal variation in aerodynamic angle of attack, sweep angle, and Mach number are incorporated in the method. The resulting computer program module based on this method is especially suited for convenient implementation in rotor airloads analyses.

The results obtained clearly indicate that it is feasible to generalize the empirical parameters embedded in the present method over a range of angle of attack, Mach number, airfoil shape and sweep angle. However, the empirical parameters, corresponding to the various data sets synthesized to date were found to be insufficient for generalization of the parameters, and synthesization of additional unsteady airfoil data is recommended.

Under the present study, unsteady drag data were synthesized which provided the basis for successful expansion of the formulation to include computation of the unsteady pressure drag of airfoils and rotor blades. Also, an improved prediction model for airfoil flow reattachment was incorporated in the method. Application of this improved unsteady aerodynamics model has resulted in an improved correlation between analytic predictions and measured full scale helicopter blade loads and stress data.

LIST OF FIGURES

LIST OF FIGURES (Cont'd)

LIST OF FIGURES (Cont'd)

LIST OF FIGURES (Cont'd)

LIST OF TABLES

LIST OF SYMBOLS

A	nondimensional pitch rate, $c\dot{\alpha}/2U$
a_{oL}	static lift curve slope
a_{om}	static pitching moment curve slope at zero angle
c	chord
C_A	empirical parameter for prediction of stall events, Eqs. (18)-(20)
C_b	airfoil camber
C_{Du}	unsteady drag coefficient
C_{Lu}	unsteady lift coefficient
C_{Mu}	unsteady pitching moment coefficient
C_T	rotor thrust coefficient
C_w	empirical parameter for prediction of stall events, Eqs. (18), (20)
C_α	empirical parameter for prediction of stall events, Eq. (19)
k	reduced frequency
M	Mach number, normal to leading edge
N_ℓ	number of hysteresis loops in a data set
N_p	number of steps per loop used
P_1, P_2, P_3	empirical parameters for C_{Lu}
$Q_1, Q_2 \ldots, Q_7$	empirical parameters for C_{Lu}
r_o	airfoil leading edge radius
R_n	Reynolds number
$R_1, R_2 \ldots R_8$	empirical parameters for C_{Du}

LIST OF SYMBOLS (Cont'd)

s	nondimensional time, $2Ut/c$
s_m	nondimensional time measured from instant of stall onset
s_{mt}	predicted value of s_m when vortex leaves T.E., Eq. (19)
t	time in seconds
t_{dm}	time when dynamic stall first occurs
t/c	airfoil thickness ratio
U	freestream velocity
V	helicopter velocity in knots
α	instantaneous angle of attack
$\dot{\alpha}$	time derivative of α
α_{Dm}	dynamic moment stall angle
α_E	effective aerodynamic angle of attack
α_{RE}	angle of dynamic reattachment
α_{TE}	angle of attack when vortex near trailing edge
α_{qs}	quasi-static stall angle
α_{ss}	static stall angle
α_w	aerodynamic parameter defined by Eq. (3)
$\bar{\alpha}$	amplitude of oscillation, deg
α_o	mean angle of oscillation, deg
β_1	empirical constant in Eq. (27), normally equals 0.18
δ_1, δ_2 δ_3, δ_4	dynamic parameters defined by Eqs. (29), (30), (35), (36), respectively
ΔC_D	incremental drag coefficient

$\Delta C_{L1}, \Delta C_{L2}$	incremental lift coefficient
ΔC_M	incremental moment coefficient
$\Delta\alpha_1$	shift in angle defined by Eq. (24), deg
$\Delta\alpha_2$	shift in angle defined by Eq. (25), deg
$\Delta\psi$	incremental azimuth angle, deg
ϵ	empirical parameter $(\alpha_{qs}-\alpha_{ss})/\alpha_{ss}$
ϵ_{rms}	root mean square error
γ_1, γ_2	functions defined by Eqs. (8), (9), respectively
ϕ	blade section inflow angle, deg
ϕ_c	compressible Wagner function
θ	blade section pitch angle, deg
$\eta_1, \eta_2 \ldots \eta_7$	empirical parameters for C_{Mu}
Λ	aerodynamic sweep angle, deg
Ω	rotor rotational speed, rad/sec
σ	rotor solidity

Subscripts

DS	dynamic stall
k	indicates time step number k
m	at time of dynamic moment stall
n	indicates time step number n
qs	quasi-static
R	at time of dynamic reattachment
RE	reattachment

S	static coefficient
t	at time of vortex leaving airfoil trailing edge
TE	trailing edge

INTRODUCTION

During helicopter high speed flight, the occurrence of retreating blade stall causes a significant increase in the pitch link loads and blade stresses which may limit the operating regime of the helicopter. For efficient design of a helicopter, its high speed operating regime should be known in the early design and development stage. Therefore, a helicopter designer should have analytical tools available to him to determine accurately the occurrence of the retreating blade stall and associated blade loads. Due to the unavailability of a simple general method that predicts these dynamic stall airloads, most of the aeroelastic analyses continue to employ quasi-steady aerodynamic theories to compute them. However, quasi-steady aerodynamics are highly inadequate during dynamic stall. A new analytical capability to accurately predict the effects of blade stall is therefore a highly desirable development in advancing the state-of-the-art in helicopter design.

Recently a methodology involving use of synthesized data has been successfully developed with the main objective of providing a workable prediction procedure for analytically computing unsteady airloads of helicopter rotor blades operating in stall (Ref. 1). The synthesized data essentially consist of semi-empirically obtained analytical expressions, and in general, they represent simple quantitative approximations to the various observed physical features associated with the dynamic stall of airfoils.

Typically, a helicopter rotor blade encounters a highly variable aerodynamic environment as it moves around the azimuth. More specifically, for the helicopter in forward flight, the blade sections are subjected to azimuthal variation in not only the angle of attack but also in aerodynamic sweep angle and Mach number. As a result, the prediction of stall occurrence on helicopter rotors is much more involved than on conventional aircraft. Even if only static conditions are involved, it is known that the type of stall and separation characteristics associated with each different airfoil section vary widely. In addition, wind tunnel test results on oscillating airfoils have clearly demonstrated the sensitivity of the airfoil dynamic stall behavior to the various parameters of the unsteady motion (Refs. 2-6). Beyond the direct measurement of unsteady pressures, recent dynamic stall experiments (Ref. 4) used flow visualization and other advanced measurement techniques to yield a more accurate picture of the aerodynamic environment that exists in the vicinity of the stalled airfoils. One of the main features of this flow environment is the formation and streamwise movement of the vortex shed from the airfoil leading edge during dynamic stall. Indeed, the difficulties of including important features like the stall vortex led to a belief that the development of a purely theoretical method for the prediction of dynamic stall and unsteady airloads for helicopter rotor blades was beyond the scope of the

present state of the art. Because of this reason, the procedure followed here (Ref. 1) involved using the available unsteady oscillating airfoil test data and a new semi-empirical technique to develop a simple general method that could predict these airloads accurately. Currently, in the helicopter industry, there do exist several empirical unsteady airloads prediction methods (e.g., Refs. 7-10), but these methods do not include many important features of dynamic stall phenomenon, such as modeling of the stall vortex. Hence, the analytical predictions of unsteady airloads based on these methods do not show accurate correlation with the original oscillating airfoil test data. However, the present method incorporates an analytical model of dynamic stall that adequately accounts for the effects of formation and streamwise travel of the dynamic stall vortex. As a result, the synthesized or computed unsteady lift and pitching moment hysteresis loops were shown in Ref. 1 to closely coincide with the two-dimensional airfoil test data. Furthermore, the prediction technique employed herein is such that it can be easily extended to simulate the aerodynamic loads on a helicopter rotor blade including the effects of azimuthal variation in angle of attack, Mach number and sweep angle.

The present report describes the results of the analytical research program that was undertaken to expand the Ref. 1 synthesized unsteady airfoil data method using additional available sets of unsteady airfoil data. These sets of data are the NASA Ames data (Ref. 5), UTRC data (Ref. 2), and Boeing-Vertol data (Ref. 6). The primary objective was to reduce these data to synthesized form within the established Ref. 1 framework, and to generalize the results. A secondary objective of the study was to apply the resulting methodology to a limited number of correlation calculations of full-scale helicopter blade stresses and airloads.

The results in Ref. 1 had included only normal force and pitching moment coefficient synthesization. Hysteretic unsteady drag data are available in Refs. 2 and 5 for a number of Mach numbers and for various airfoils, and the present program has been expanded to include the computation of the unsteady pressure drag coefficient data. The new version of the program is now capable of simultaneous synthesis of all three unsteady coefficients (C_L, C_M, C_D). Additionally, an improved model of reattachment-prediction (Ref. 1) has been incorporated in the present program. Inclusion of these improvements in the unsteady aerodynamic model has resulted in a better correlation between analytic predictions and the full scale helicopter blade stress test data.

The present report describes in detail the various features of the synthsized unsteady airfoil data method. For completeness, some of the features originally discussed in Ref. 1 are repeated in the present report.

DYNAMIC STALL MODEL

The analytical model of dynamic stall, described herein, includes some main physical features of the dynamic stall phenomenon as observed in oscillating airfoil tests. A brief description of dynamic stall events is given below.

When an airfoil experiences an unsteady increase in angle of attack beyond the static stall angle, a vortex starts to grow near the leading edge region. As the angle continues to increase, the vortex detaches from the leading edge and is convected downstream near the surface. These events are shown schematically in Fig. 1. The suction associated with the vortex normally causes an initial increase in lift. The magnitude of the increase depends on the strength of the vortex and its distance from the surface. The streamwise movement of the vortex depends on the airfoil shape, angle of attack and the pitch or plunge rate. The relative distance between the vortex and the airfoil varies according to the motion of the airfoil. That is, it depends on characteristics such as the pitch rate and the instantaneous angle of attack. As the vortex leaves the trailing edge, a peak negative pitching moment is obtained. The airfoil then remains stalled until the angle of attack drops sufficiently so that reattachment of the flow can occur. The present method incorporates all of these events. For example, the strength of the vortex is made a function of the angle when the vortex leaves the leading edge (moment stall angle). The higher the moment stall angle, the higher the strength of the vortex.

Discussion of Parameters Influencing Dynamic Stall

The unsteady lift, drag, and pitching moment coefficients of the airfoils obtained from the two-dimensional oscillating airfoil tests show a large degree of hysteresis when plotted as functions of angle-of-attack, particularly when the maximum angle of attack is above the static stall angle. Figure 2 shows an example of typical loop data obtained from the oscillating airfoil test. The amount of hysteresis and the shape of the loops seem to vary in a highly nonlinear fashion with the test parameters such as the amplitude, the mean angle and the reduced frequency. However, when the effects of the vortex shed from the leading edge are separated out, the loop data variation with the test parameters is of relatively simpler nature and shows a much more consistent pattern. Analysis of the data presented in Ref. 4 substantiates this assertion. As a result it becomes much easier to synthesize the unsteady data from the static airfoil data. The synthesization process used herein essentially involves curve-fitting of the test loop data to the prescribed analytical expressions, with the objective of determining the unknown parameters or coefficients embedded in the analytical expressions. The analytical expressions are obtained mostly by mathematical or empirical means and in general they

represent simple quantitative approximations to the various observed physical features of the dynamic stall phenomenon. Thus, the present method involves development of new and simple formulations that utilize a compact set of appropriate dynamic parameters and determine the unsteady dynamic stall airloads accurately. The identification and the selection of the parameters that are relevant to the helicopter blade airloads prediction methodology is discussed next.

The results of the pitch oscillation airfoil tests clearly indicate that the dynamic characteristics of an airfoil depend on the following main parameters: 1) airfoil shape and sweep; 2) Mach number; 3) Reynolds number; 4) reduced frequency, k; 5) oscillation amplitude, $\bar{\alpha}$; and 6) mean angle of attack, α_o.

The first three of these parameters affect both the static and the dynamic characteristics of the airfoil, while the last three parameters represent purely dynamic parameters. Since many of the rotor aeroelastic analyses employ the time history solution techniques for computation of the aerodynamic loading acting on the helicopter rotor blades, the frequency domain parameters such as reduced frequency or amplitude, etc., are inappropriate for use in these time domain simulations. Moreover, it is difficult to describe the reduced frequency, the amplitude of oscillation, or the mean angle of attack of a helicopter blade section in a precise manner. As a result, an alternative set of dynamic parameters that are appropriate for the time domain simulations is defined. The parameters replacing k, $\bar{\alpha}$, and α_o in the present method are: 4) the instantaneous angle of attack, α; 5) the nondimensional pitch rate A; and 6) the decay parameter α_w, which accounts for the time history effects of the change in α, and is based upon the Wagner function.

For the sinusoidally oscillating airfoil, these three parameters can be easily expressed in terms of the reduced frequency, the amplitude, and the mean angle of attack. Also, they can be easily evaluated for a helicopter blade section in a stepwise manner and are very convenient to use for the prediction of onset of dynamic stall and for the determination of the unsteady airloads. Thus, the present method determines, through the synthesization process, the effect of these selected parameters (α, A, α_w) on the dynamic stall characteristics of the airfoils by utilizing the data from the oscillating airfoil tests.

Finally, since under the present study the dynamic characteristics are to by synthesized from static airfoil data, some effects of the first three parameters (airfoil shape/sweep, Mach number and Reynolds number) are directly accounted for through the use of static data. The remaining effects of these parameters, those related to dynamic stall, are accounted for separately. As will be shown later, the empirical coefficients or constants obtained through the synthesization process are allowed to vary with these parameters. Thus, the variation in the values of the empirically obtained constants represents the dynamic effects of the first three parameters. It may be noted that

whatever parameter (e.g., Mach number, Reynolds number, etc.) conventionally affects the static stall characteristics also affects the values of empirical constants embedded in the empirical relationships.

Definition of Parameter α_w

For a two-dimensional airfoil going through an arbitrary change in angle of attack, one can describe an instantaneous effective angle of attack, α_E, by using Duhamel's integral (Ref. 11) as given below:

$$\alpha_E(s) = \alpha(0)\,\phi_C(s,M) + \int_0^s \frac{d\alpha}{d\sigma}\,\phi_C(s-\sigma, M)\,d\sigma \tag{1}$$

where α (o) corresponds to the initial angle of attack, M represents Mach number, $\phi_C(s,M)$ is the response to a step change in α (i.e., the Wagner function) and s is the nondimensional time given by

$$s = \frac{2Ut}{C} \tag{2}$$

The parameter α_w, to be used extensively in the present method, is defined as follows:

$$\alpha_w = \alpha(s) - \alpha_E(s) \tag{3}$$

The parameter α_w used in the present method represents physically the difference between the instantaneous angle, α and the effective angle, α_E, and therefore accounts for the time history effects of the change in α. This physical description of α_w is valid for attached flow conditions only. In the present method, the parameter α_w is most useful for predicting the onset of dynamic stall, but for convenience it is also used to approximately describe the unsteady coefficients after the stall. This being an empirical method, the continuing use of α_w beyond stall does not seem to adversely affect the results.

The effects of compressibility are incorporated in the definition of α_w by the use of the general or compressible Wagner function (see also Ref. 10) obtained from the following approximate relationship

$$\phi_C(s,M) = \left[1.0 - 0.165e^{-0.0455\,s\,(1-M^2)} - 0.335\,e^{-0.3s\,(1-M^2)}\right] / \sqrt{1-M^2} \tag{4}$$

Computation of Dynamic Parameters

For the sinusoidally oscillating airfoil, where the motion of the airfoil is completely known, the parameters α, A and α_w can be obtained analytically as given below:

$$\alpha = \alpha_0 + \bar{\alpha} \sin ks \tag{5}$$

$$A = k\bar{\alpha} \cos ks \tag{6}$$

$$\alpha_w = \gamma_1 (k, M)\, k\bar{\alpha} \cos ks + \gamma_2 (k, M)\, \bar{\alpha} \sin ks \tag{7}$$

where k, s and M represent reduced frequency, nondimensional time and Mach number, respectively. The complete derivation of Eq. (7) is described in Appendix A. Here the functions γ_1 and γ_2 are described by

$$\gamma_1 (k, M) = \frac{0.165(1-M^2)(0.0455)}{k^2 + (1-M^2)^2 (0.0455)^2} + \frac{0.335(1-M^2)(0.3)}{k^2 + (1-M^2)^2 (0.3)^2} \tag{8}$$

$$\gamma_2 (k, M) = \frac{0.165k^2}{k^2 + (1-M^2)^2 (0.0455)^2} + \frac{0.335k^2}{k^2 + (1-M^2)^2 (0.3)^2} \tag{9}$$

The variation of the functions γ_1 and γ_2 with reduced frequency are shown in Fig. 3 for M = 0.3.

In contrast to the closed form evaluation for sinusoidal oscillations, the motion of a helicopter blade is not known a priori, and the blade section dynamic parameters must be evaluated numerically in a stepwise manner by utilizing the following recursive relationships at step n

$$\alpha_n = \theta_n + \phi_n \tag{10}$$

$$A_n = (\Delta\theta)_n / (\Delta s)_n + (1.5\phi_n - 2.0\phi_{n-1} + 0.5\phi_{n-2})/(\Delta s)_n \tag{11}$$

$$(\alpha_w)_n = X_n + Y_n \tag{12}$$

where

$$X_n = X_{n-1}\, e^{-0.0455(1-M^2)(\Delta s)_n} + 0.165(\alpha_n - \alpha_{n-1}) \tag{13}$$

$$Y_n = Y_{n-1}\, e^{-0.3(1-M^2)(\Delta s)_n} + 0.335(\alpha_n - \alpha_{n-1}) \tag{14}$$

$$(\Delta s)_n = \frac{2U_n}{\Omega c}(\Delta\psi) \tag{15}$$

Here $\Delta\psi$ is azimuthal stepsize, Ω is rotor speed, c is chord length, and U_n is tangential velocity component.

The instantaneous angle of attack, α_n, is described in the tip-path-plane system, θ_n and ϕ_n being the pitch angle and inflow angle, respectively. It should be noted that the time derivative of pitch angle in Eq. (11), $(\Delta\theta/\Delta s)$, may be computed analytically from the known cyclic or harmonic inputs, while the time derivative of ϕ has to be computed by the backward difference scheme. The derivation of Eqs. (12)-(15) for α_w is described in Appendix A.

Prediction of Dynamic Stall Events

In the present method it is considered important to accurately predict three major events associated with dynamic stall. These events, as shown in Fig. 2b, are the stall onset, the vortex at the trailing edge and the reattachment. A comprehensive description of these events is presented in Ref. 4. The next section describes the semi-empirical equations that are used to predict these events.

Onset of Stall

Because the dynamic stall airloads acting on an airfoil are highly influenced by the leading edge vortex, an accurate prediction of the instant the vortex breaks away from the leading edge (moment stall point) becomes very important. The occurrence of moment stall depends on factors such as Mach number, the airfoil shape and the pitch rate.

Under the conventional quasi-static theory formulation, the stall is assumed to occur when the effective angle of attack reaches the static stall angle,

$$\alpha_{Em} = \alpha_{ss} \tag{16}$$

In general, α_{ss} is assumed to vary with the airfoil shape, Mach number and Reynolds number. To some extent, the value of α_{ss} also depends on the criterion followed for stall.

Under the present formulation, the relationship represented by Eq. (16) is extended to include dynamic stall effects, and an assumption is made that at the dynamic stall point, in general, the effective angle of attack, α_{Em}, is not only a function of α_{ss}, but also depends on the pitch rate at stall, A_m, and the instantaneous angle of attack at stall. That is,

$$\alpha_{Em} = F(\alpha_{ss}, A_m, \alpha_{Dm}) \tag{17}$$

The actual functionality F depends on the type of stall and on the criterion followed for stall. It is assumed that F varies with airfoil shape, Mach number, and the Reynolds number, and can be established empirically. Linearization of the relationship of Eq. (17) with respect to parameters A_m and α_{Dm} (see Appendix B) around quasi-steady conditions ($\alpha_{ss}(1+\epsilon)$) leads to the following simple expression for α_{Dm}, the instantaneous angle at which dynamic moment stall first occurs:

$$\alpha_{Dm} = (1+\epsilon + C_{Am} A_m + C_{wm}\alpha_{wm})\alpha_{ss} \tag{18}$$

Here α_{wm} represents the value of the parameter, α_w, at the point of moment stall. Thus, instead of the function F, one can determine empirically the coefficients ϵ, C_{Am} and C_{wm} for various Mach numbers, Reynolds numbers and airfoils. In Eq. (18), the last two terms represent the delay in dynamic stall when compared with quasi-static stall. Most other current methods (e.g., Ref. 8) represent this delay in stall by a constant time delay. However, Eq. (18) is a much more general relationship that predicts the onset of dynamic stall quite accurately for airfoils experiencing unsteady motion.

Vortex at Trailing Edge

Normally, after the occurrence of moment stall, there is a significant increase in negative pitching moment due to the travel of the stall vortex. The maximum negative pitching moment occurs when the vortex is near the trailing edge of the airfoil. For the case shown in Fig. 2, the instant when the vortex leaves the trailing edge is marked by 'α_{TE}'. Preliminary results

indicate that the following empirical relationship can be utilized to predict the instant when the vortex leaves the airfoil

$$s_{mt} = 1.0 / (C_{At}\ A_m + C_{\alpha t}\ \alpha_{Dm}) \tag{19}$$

Here s_{mt} is the total nondimensional time for the vortex to travel from the leading edge to the trailing edge. Once again, the coefficients C_{At} and $C_{\alpha t}$ vary with Mach number, airfoil shape, sweep, and Reynolds number.

Reattachment

The instant when the reattachment of the flow occurs is marked in Fig. 2. Normally, for low Mach numbers ($M \leq 0.4$) the reattachment occurs at an angle α_{RE} which is less than the static stall angle. At higher Mach numbers, where the static stall may be induced by shocks, the reattachment angle α_{RE} can be higher than the static stall angle α_{ss}. In the present formulation, a general expression for α_{RE} is assumed and it is given by

$$\alpha_{RE} = (1 - \epsilon + C_{AR}\ A_m + C_{wR}\ \alpha_{wm})\ \alpha_{ss} \tag{20}$$

In general, for a given airfoil, the values of C_{AR} and C_{wR} (Eq. (20)) are quite different from those of C_{Am} and C_{wm} (Eq. (18)). However, the value of the parameter ϵ is the same in both of these equations.

This completes the description of all the events associated with dynamic stall that are required to compute the unsteady stall aerodynamic characteristics of an airfoil. It should be noted that the present formulation does not require explicit prediction of so-called 'dynamic lift stall'. Normally a sudden loss of lift occurs due to an increase in the relative distance between the stall vortex and the airfoil surface. This generally happens when the vortex is over the aft portion of the airfoil and the airfoil is pitching up, but sometimes it so happens that the vortex is still over the aft portion of the airfoil when the airfoil starts pitching down. As a result, there may be a sharp increase in lift even when the airfoil is pitching down. A good example of this is illustrated by the test data of Fig. 4. Therefore, the maximum dynamic lift coefficient obtained is a function of strength of the vortex as well as the relative distance of the vortex from the airfoil surface. These effects are included implicitly in the formulation of the unsteady lift coefficient which is described in a later section.

Occurrence of Dynamic Stall on Rotor Blades

Figure 5 illustrates how the prediction of dynamic stall is extended to the case of a rotor blade. Figure 5 shows the azimuthal variation of angle of attack of a helicopter blade section. The variation corresponds to a full scale rotor blade section at 60 percent radius. The flight condition corresponds to that of a forward flight at 152 knots. The corresponding Mach number and the aerodynamic sweep angle variation with azimuth are also shown in Fig. 5. Knowing the Mach number and sweep angle at each instant, as will be discussed later, one can determine the instantaneous values of α_{ss} and the coefficients ϵ, C_{Am} and C_{wm}. Also at each instant the values of the parameters A and α_w are known. As a result an angle α_{SB} can be defined at each time step as shown on Fig. 5 and given below

$$\alpha_{SB} = (1+\epsilon + C_{Am} A + C_{wm}\alpha_w)\,\alpha_{ss} \tag{21}$$

The angle α_{SB} represents physically the stall boundary at each instant. When α exceeds α_{SB}, onset of stall occurs. The values of dynamic parameters α and A corresponding to the point 'α_{Dm}' in Fig. 5 are utilized for computing the incremental unsteady airloads after the occurrence of stall. For example, the empirical relationship (Eq. (19)) is utilized to predict the instant when the vortex leaves the blade trailing edge. The coefficients C_{At} and $C_{\alpha t}$ used in Eq. (19) are calculated using the Mach number and sweep angle at the time of stall.

The instant when the reattachment of the flow occurs is marked as 'α_{RE}' in Fig. 5. An angle α_{RB}, similar to the one in Eq. (20), is defined as described here

$$\alpha_{RB} = (1-\epsilon + C_{AR} A_m + C_{WR}\alpha_{wm})\,\alpha_{ss} \tag{22}$$

The reattachment of the flow on the blade section is assumed to occur when the instantaneous angle α equals α_{RB}.

ESTABLISHMENT OF SEMI-EMPIRICAL EQUATIONS

As mentioned earlier, the available oscillating airfoil test data are used to determine the various empirical parameters or constants (e.g., ϵ, C_{Am} and C_{wm} in Eq. (18)) embedded in the empirical relationships. For an airfoil, the test data are normally available in frequency domain. At each Mach number, the test data are normally obtained over a limited range of reduced frequencies, mean angles of attack and oscillatory amplitudes. Since the present method is formulated for time-domain simulation, Eqs. (5)-(7) are used to convert the test data into a time-domain representation.

The first step in the present procedure for synthesis normally involves preparing a data set consisting of the loop data obtained for an airfoil at the same Mach number, Reynolds number, and sweep angle. Normally, a set of fifteen loops, consisting of both unstalled and stalled data, is found to be sufficient to establish the values of the empirical coefficients. The second step of the synthesis procedure consists of determining the empirical coefficients through least squares fitting. The final step involves reconstructing the data from the empirical relations and comparing the synthesized data with the test data.

Test Data Used for Present Synthesis

Table I provides a list of all the data sets that have been successfully synthesized under the present study. The results corresponding to all these sets have been included in the present report. The data sets listed in Table I were acquired from three different sources: 1) AVRADCOM (Ref. 5)* provided data sets 1 through 6; 2) USAAVLABS TR-68-13B (Ref. 6) contained data sets 7 through 11; and 3) UTRC (Ref. 2) supplied data sets 12 through 17. The data sets 14 and 15 designated as yawed 0012 correspond to the data of the NACA 0012 airfoil obtained at 30 degrees sweep.

Each of the seventeen data sets represents a unique combination of test conditions. As a result, the values of the various empirical coefficients obtained are, in general, different for each of these data sets. Also, it should be noted that each of these data sets have, in general, a different static airfoil characteristic associated with them (steady state C_L, C_M, C_D variation with α).

---

* Actual data, described in Ref. 5, were made available to UTRC in magnetic tape form for use in this study. Future publication of the data is expected by AVRADCOM.

Validation of Predicted Stall Events

This section describes the comparison between the test and the predicted values for the various stall events associated with the occurrence of dynamic stall. These stall events designated as α_{Dm}, α_{TE}, and α_{RE} have been shown in Fig. 2 for a typical set of test loops (data set 1 in Table I). Figure 6 collects all of these stall events onto a single chart, in which the three quantities, α_{Dm}, α_{TE}, and α_{RE} are plotted as points for a sequence of loop numbers, displayed horizontally below the data points. Accompanying each loop number is a set of values of α_o, $\bar{\alpha}$, and k. Although not primarily used to show the variation of α_{Dm}, α_{TE}, and α_{RE} with any of the abscissa parameters, this type of presentation will be found to be useful in evaluating the ability of Eqs. (18)-(20) to reproduce the original data with accuracy. Figure 6 shows the variation of these stall events with various test parameters, those being the mean angle (α_o), the amplitude ($\bar{\alpha}$) and the reduced frequency (k). All the loops represented in Fig. 6 correspond to the test data obtained for the SC 1095 airfoil at the same Mach number (M = 0.3) and Reynolds number ($R_n = 3.8 \times 10^6$). At these conditions the static stall angle is 12.5 degrees and the quasi-steady stall angle is 14.0 degrees. When various values of α_{Dm} are curve-fitted (in least squares sense) to the semi-empirical relationship described by Eq. (18), the values of empirical constants C_{Am} and C_{wm} are obtained. Similarly, curve-fitting of the various values of α_{TE} (Fig. 6) to Eq. (19) and matching of α_{RE} values in Fig. 6 to Eq. (20) determines the values of the parameters C_{At}, $C_{\alpha t}$, C_{AR} and C_{wR}. The values of these parameters for the condition of Fig. 6 are provided in Table II.

The accuracy of Eqs. (18)-(20) to model analytically the various stall events is illustrated by Fig. 7 in which the data points and identifying abscissa parameters have been repeated from Fig. 6, but with the addition of synthesized values of α_{Dm}, α_{TE}, and α_{RE}, which are connected by dashed, solid, and dash-dot lines, respectively. As indicated by Fig. 7, the synthesized α_{Dm} (Eq. (18)), α_{TE} (Eq. (19)) and α_{RE} (Eq. (20)) compare very well with the corresponding test values. The difference between the synthesized and test values are small and these differences are comparable to the precision ($\pm$ 0.5 deg) with which these stall events are described by the present method. It should be noted that for the description of various stall events the present method uses the test loop data for C_{Mu} (an example is shown in Fig. 2b).

To further illustrate the accuracy, and also to demonstrate the generality of Eqs. (18)-(20) to model the various stall events, Figs. 8-11 show similar results obtained for the NACA 0012 airfoil at various Mach numbers and Reynolds numbers (data sets 2, 13, 9 and 15, respectively in Table I). The agreement between test and synthesized data in Fig. 10 is especially noteworthy because it shows that even at high Mach numbers (M = 0.6), where the stall is shock induced, Eqs. (18)-(20) accurately predict the various dynamic stall events. The results obtained for the remaining data sets (corresponding

values of the empirical coefficients for these data sets are also provided in Table II) were similar to the sample results shown in Figs. 6-11. The excellent agreement between the test results and empirical relationships, as illustrated by Figs. 7-11, clearly demonstrates the generality of the present method to adequately represent the effects of variation in type of stall (associated with the variation in Mach number, sweep and airfoil shape). These effects are implicitly represented by the variation in the value of the empirical parameters (such as ϵ, C_{A_m}, C_{wm}) corresponding to the different data sets (Table II).

Now that the present formulation for predicting the major dynamic stall events has been validated, the next section provides the empirical relationships that are used to describe the unsteady aerodynamic characteristics of an airfoil in the time-domain between these discrete stall events.

COMPUTATION OF UNSTEADY AERODYNAMIC CHARACTERISTICS

This section describes the unsteady aerodynamic characteristics (C_{Lu}, C_{Mu}, and C_{Du}) of an airfoil in terms of the dynamic parameters (α, A and α_w) that have been defined in an earlier section. It should be understood that the equations were obtained empirically, and many of the terms have been established by an heuristic process. Therefore, a traditional derivation based on physical first principles does not apply to all the equations that follow, and the physical associations of the terms with stall events (for example) were made through the empirical process.

Unsteady Lift Coefficient

The unsteady lift coefficient, C_{Lu}, of an airfoil in the time domain under the present synthesization is described by the following expressions:

$$C_{Lu} = C_{LS}(\alpha - \Delta\alpha_1 - \Delta\alpha_2) + a_{OL}\Delta\alpha_1 + \Delta C_{L1} + \Delta C_{L2} \tag{23}$$

$$\Delta\alpha_1 = (P_1 A + P_2 \alpha_w + P_3)\alpha_{ss} \tag{24}$$

$$\Delta\alpha_2 = \delta_2 \alpha_{ss} \tag{25}$$

$$\Delta C_{L1} = Q_1 A + Q_2 \alpha_w + Q_3(\alpha/\alpha_{ss}) + Q_4(\alpha/\alpha_{ss})^2 \tag{26}$$

$$\Delta C_{L2} = Q_5 \delta_1 + Q_6 \Delta\alpha_2 + Q_7(\alpha_{Dm})^2 \left[\frac{1-e^{-(\beta_1 s_m)^3}}{(\beta_1 s_m)^2}\right] \tag{27}$$

$$s_m = \frac{2U(t-t_{dm})}{C} \tag{28}$$

$$\delta_1 = \begin{cases} 0 & \alpha \le \alpha_{ss} \\ (\alpha/\alpha_{ss} - 1) & \alpha_{ss} \le \alpha \le \alpha_{Dm} \\ (\alpha_{Dm}/\alpha_{ss} - 1)\left[1.0 - (s_m/s_{mt})^2\right] & 0 \le s_m \le s_{mt} \\ 0 & s_m > s_{mt} \end{cases} \tag{29}$$

$$\delta_2 = \begin{cases} 0 & \alpha \le \alpha_{ss} \\ (\alpha/\alpha_{ss} - 1) & \alpha_{ss} \le \alpha \le \alpha_{Dm} \\ (\alpha_{Dm}/\alpha_{ss} - 1) & 0 \le s_m \le s_{mt} \\ (\alpha_{Dm}/\alpha_{ss} - 1)\dfrac{\alpha - \alpha_{RE}}{\alpha_{TE} - \alpha_{RE}} & \alpha_{RE} \le \alpha \le \alpha_{TE} \\ 0 & \alpha \le \alpha_{RE} \end{cases} \tag{30}$$

The synthesized unsteady lift coefficient (Eq. (23)) has been expressed as a sum of static C_{LS} at some shifted angle $(\alpha-\Delta\alpha_1-\Delta\alpha_2)$ plus an incremental lift coefficient $(\Delta C_{L1}+\Delta C_{L2})$. The shift in angle is given by Eqs. (24)-(25) and the incremental lift coefficient by Eqs. (26)-(27). (The quantity a_{oL} in Eq. (23) is the conventional static lift curve slope.) The $\Delta\alpha_1$ shift in angle (Eqs. (24)) is present even when no stall occurs, and the $\Delta\alpha_2$ shift in angle (Eq. (25)) is mainly associated with the occurrence of dynamic stall and subsequent reattachment. Similarly, the ΔC_{L1} (Eq. (26)) represents essentially the unsteady effects over static C_{LS} for dynamically unstalled airfoils, and ΔC_{L2} (Eq. (27)) represents the effects associated with the dynamic stall events such as vortex formation and reattachment. In fact, the last term in Eq. (27) represents explicitly the suction effects of the leading edge vortex and equals zero when no vortex exists. Thus, Eq. (23) is a general expression for unsteady C_L even when no dynamic stall occurs. For unstalled cases, the magnitudes of $\Delta\alpha_2$ and ΔC_{L2} are essentially zero.

The parameter β_1 in Eq. (27) is an empirically determined constant and it equals 0.18 for all the data used in the present study. The quantity s_m, as described by Eq. (28), represents the nondimensional time measured from the instant of the occurrence of dynamic moment stall. The unknown parameters P_1 through P_3 and Q_1 through Q_7 are determined empirically by means of least squares curve-fitting of Eq. (23) with the test data. It should be noted that most of the terms in Eq. (23) are linear in parameters α, A, and α_w. However, since the argument of one of the terms (C_{LS}) in Eq. (23) involves unknowns P_1, P_2 and P_3, a nonlinear least squares curve-fitting technique must be used. The nonlinear least squares technique employed here for C_{Lu} is similar to the one described on page 82 of Ref. 12.

Unsteady Moment Coefficient

The unsteady pitching moment coefficient, C_{Mu}, has been established to follow the relationships similar to those for C_{Lu} and it is described as given below:

$$C_{Mu} = C_{MS}(\alpha - \Delta\alpha_2) + a_{0m}\,\Delta\alpha_2 + \Delta C_M \tag{31}$$

$$\Delta C_M = \eta_1 A + \eta_2\,\alpha_w + \eta_3(\alpha/\alpha_{ss}) + \eta_4\,|\alpha_w| + \eta_5\,\delta_1 + \eta_6\,\Delta\alpha_2 + \eta_7\,\alpha_{Dm}\,A_{Dm}\,s_m \tag{32}$$

Here a_{0m} represents the static pitching moment slope at zero angle of attack and it normally equals zero. The last term in Eq. (32) represents the vortex effects. For unstalled airfoils, the last three terms in Eq. (32) are zero.

The unknown parameters η_1 through η_7 once more are determined by the least-square curve-fitting of Eq. (31) to the test data. However, since the shift in angle $\Delta\alpha_2$ does not have any unknowns (unlike $\Delta\alpha_1$ in Eq. (23)), the nonlinear least-squares technique is not required for Eq. (31). The conventional linear least squares technique will suffice.

Unsteady Drag Coefficient

The unsteady drag coefficient, C_{Du}, appears to vary with the dynamic parameters in the same way as C_{Mu} and is described as follows:

$$C_{Du} = C_{Ds}(\alpha - \Delta\alpha_2) + \Delta C_D \tag{33}$$

$$\Delta C_D = R_1 A + R_2\,\alpha_w + R_3(\alpha/\alpha_{ss}) + R_4\,|\alpha_w| + R_5\,\delta_3 + R_6\,\delta_4 + R_7\,\Delta\alpha_2 + R_8\,\alpha_{Dm}\,A_{Dm}\,s_m \tag{34}$$

where

$$\delta_3 = \begin{cases} 0 & \alpha \le \alpha_{ss} \\ (\alpha/\alpha_{ss} - 1) & \alpha_{ss} \le \alpha \le \alpha_{Dm} \\ (\alpha_{Dm}/\alpha_{ss} - 1)\left[1. - (s_m/s_{mt})^{.25}\right] & 0 \le s_m \le s_{mt} \\ 0 & s_m > s_{mt} \end{cases} \tag{35}$$

$$\delta_4 = \begin{cases} 0 & \alpha \le \alpha_{ss} \\ (\alpha/\alpha_{ss} - 1)^2 & \alpha_{ss} \le \alpha \le \alpha_{Dm} \\ (\alpha_{Dm}/\alpha_{ss} - 1)^2 \left[1. - (s_m/s_{mt})^{.25}\right] & 0 \le s_m \le s_{mt} \\ 0 & s_m > s_{mt} \end{cases} \tag{36}$$

The last term in Eq. (34) represents the effects of the stall vortex on the unsteady drag. For unstalled conditions, the last four terms in Eq. (34) are essentially equal to zero. Once more, the unknown parameters R_1 through R_8 are computed by using the linear least squares curve fitting of Eq. (34) to the unsteady drag test data.

Improvements Over Earlier Representations

Equations (23)-(36), representing the unsteady aerodynamic characteristics of an airfoil in the present report, differ slightly from the corresponding equations presented in Ref. 1. These modifications, as described next, were carried out mainly to improve correlation between the test data and theory. Equation (30), describing a parameter δ_2, had to be modified to incorporate a new improved model of reattachment. In the earlier representation (Ref. 1), two empirical parameters (Q_7 and Q_8)were used to model the incremental lift due to the stall vortex. The resulting values of these parameters were such that it was impossible to generalize these parameters. As a result, in the present formulation, the number of parameters for the vortex lift were reduced from two to one (Q_7 only). This simplification was achieved with negligible loss in accuracy.

The number of empirical parameters for unsteady pitching moment coefficient (Eqs. (31)-(32)) were increased from six to seven. This modification was necessary for improving correlation between the test data and theory in the aft-reattachment part of hysteresis loops. Finally, to improve the post stall matching of calculated unsteady drag coefficient values with test data, the parameter δ_1 (Eq. (29)) used in C_{Du} was removed and replaced by two modified parameters δ_3 and δ_4 (described in Eqs. (35)-(36)).

COMPARISON OF SYNTHESIZED LOOP DATA WITH TEST DATA

This section discusses the results obtained from the curve fitting of Eqs. (23), (31), and (33) to the test loop data corresponding to lift coefficient, pitching moment coefficient, and drag coefficient, respectively. As a typical case, consider all the lift coefficient loop data contained in data set number 1 (Table I). When these loop data are curve fitted to Eq. (23) in a least squares sense, the values of unknown parameters P_1 through P_3 and Q_1 through Q_7 are obtained. These computed values for the present case (data set no. 1) are described in the first row of Table III. When these values of the parameters P_1, P_2, P_3 and Q_1 through Q_7 are inserted in Eq. (23), the resulting time-domain equation represents the two-dimensional unsteady lift coefficient of the SC 1095 airfoil at Mach number 0.3 for essentially all dynamic conditions.

To illustrate the accuracy of the resulting equation, a sample of the loop data for this case has been reconstructed from the equation and the comparisons of these synthesized C_{Lu} loops with test data are shown in Fig. 12a. The differences between the test data and the synthesized data are small and these differences are comparable to test data accuracy.

Similarly, when all the pitching moment coefficient loops contained in the data set number 1 in Table I are curve fitted to Eq. (31), the values of unknown parameters η_1 through η_7 are obtained. These computed values are given in the first row of Table IV. The comparison of the synthesized C_{Mu} loops with test data is shown in Fig. 12b. Most of the reconstructed loops match with the test data within $\pm$ 0.01 in the unstalled region. The maximum negative C_{Mu} is generally predicted within $\pm$ 0.05 for 85 percent of all the stalled loops.

Following the same procedure for C_{Du}, the values of the unknown parameters R_1 through R_8 are obtained by curve fitting the unsteady drag loops of data set number 1 to Eq. (33), and these values are provided in the first row of Table V. The comparison of the computed unsteady drag loops with test data is shown in Fig. 12c. The peak values of the unsteady drag coefficient are predicted within $\pm$ 0.03 by Eq. (33).

The similar computations for the other sixteen data sets contained in Table I have been successfully carried out, and the resulting values of the various empirical parameters are given in rows 2-17 of Tables III through V. Table III contains the values of the parameters P_1, P_2, P_3 and Q_1 through Q_7 (Eq. (23)) for all the data sets. The corresponding values of the parameters η_1 through η_7 (Eq. 31)) and R_1 through R_8 (Eq. (33)) for all the data sets are described in Tables IV and V, respectively. Also, to provide some quantitative measure of the differences between the synthesized and the test data, the last

column in each of these tables gives values of the root-mean-square (RMS) error corresponding to each of the data sets. This RMS error, ϵ_{RMS}, is obtained by using the following expression

$$\epsilon_{Rms} = \sqrt{\frac{\sum_{1}^{N_\ell} \sum_{1}^{Np} (C_s - C_t)^2}{N_\ell * Np}} \tag{37}$$

where C_s and C_t represent the synthesized and the test values of an aerodynamic coefficient (C_{Lu}, C_{Mu} or C_{Du}), respectively; N_ℓ corresponds to the number of loops in the data set; and N_p represents the number of points per loop. For data sets 1 through 6, N_p used was 200 and for data sets 7 through 17, the value of N_p equalled 100.

Figures 12-28 illustrate the good agreement obtained between the synthesized loop data and the test data corresponding to all the data sets (Table I).

Figures 12 through 17 essentially represent the Ref. 5 data obtained through the tests performed in the U.S. Army 2- by 3-m atmospheric-pressure, solid-wall wind tunnel. The Figs. 18 through 22 correspond to the published data contained in Ref. 6 and obtained in the Boeing two-dimensional, variable-density wind tunnel. It should be noted that Figs. 18 through 22 show only the lift and pitching moment loops because no drag computations were included in Ref. 6.

Of particular interest are the comparisons between the synthesized and test data acquired at high Mach numbers (M = 0.6), shown in Figs. 20 and 22 for the V0012 and V2301-1.58 airfoils, respectively. This excellent correlation of the synthesized lift and pitching moment coefficients with test data clearly demonstrates the capability of the present method to successfully model these high Mach number unsteady airfoil characteristics.

Finally, Figs. 23 through 28 illustrate the comparison of the synthesized data with test data corresponding to the Ref. 2 experiments which were carried out in the UTRC 2.44 m octagonal wind tunnel. The results presented in Figs. 25 and 26 should be especially noted because they show the correlation between test and theory for swept wings to be as good as for unswept wings.

In conclusion, the excellent correlation between the test and synthesized results, as illustrated by Figs. 12-28, clearly demonstrates the generality of the present method to adequately represent the effects of variations in Mach number, sweep and airfoil shape.

Further Validation of Method

The synthesized unsteady lift and pitching moment coefficients as expressed by Eqs. (23) and (31) have been further tested by comparison with different kinds of data bases. Specifically, the test data for NACA 0012 airfoil obtained from the ramp tests of Refs. 13 and 14 have been compared with the corresponding results from Eqs. (23) and (31). The objective here was to test how well the synthesized data compares with the test data for those cases where the airfoil goes through nonsinusoidal motions.

The first set of ramp data was obtained from Ref. 13. These unsteady data (C_{Lu} and C_{Mu}) are presented in Fig. 29 as a function of the instantaneous angle of attack. Also shown in Fig. 29 are the computed values of unsteady C_{Lu} and C_{Mu} by utilizing Eqs. (23) and (31) and assuming the data in Ref. 13 were obtained at a constant pitch rate of A = 0.0058. For these computations, the static data presented in Ref. 13 were utilized together with the empirical data corresponding to the NACA 0012 at M = 0.3 (data set no. 12).

The excellent correlation between the ramp test data and computed data demonstrates that the empirical relations based on sinusoidal test data can be extended and used for nonsinusoidal cases. The results of an additional correlation case are presented in Fig. 30 with test data from Ref. 14. Here, the α, C_{Lu} and C_{Mu} distributions are presented as functions of time. The correlation is quite good except for the deep stall region. This may be attributed to the fact that the exact static data for this case were not available and that the use of an equivalent static data set from a different wind tunnel, particularly in the deep stall region, is expected to introduce some discrepancies in the computed values.

GENERALIZATION OF EMPIRICAL PARAMETERS

As the results presented in Tables II through V indicate, the values of the empirical parameters, in general, vary significantly with Mach number, Reynolds number, airfoil shape and sweep angle. With each data set of Table I, there is a distinct set of magnitudes of these empirical parameters as given in Tables II through V. If the magnitudes of these empirical parameters are known, say at a sufficient number of Mach numbers, it may be possible to generalize the empirical parameters for all Mach numbers. Similarly, if the empirical parameters are available for a large number of airfoils, they could be generalized and related to various distinguishing characteristics such as leading edge radius, camber and thickness ratio of the airfoils. Alternatively, these empirical parameters may be related to static airfoil characteristics such as the static lift curve slope and static stall angle. As a result, in future tests only the static data of the airfoils would have to be obtained. This is attractive because the determination of the static airfoil characteristics is both technically simpler and considerably less expensive than the acquisition of dynamic loop data. Furthermore, by using the generalization based on present methodology, it may be feasible to tailor the airfoil shape and thus design airfoils that have desired dynamic characteristics. The results of a limited effort to generalize these empirical parameters are discussed next.

Variation with Airfoil Shape

The computed empirical parameters corresponding to the first four data sets in Tables II through V represent the unsteady airfoil data for four distinct airfoil shapes (SC 1095, NACA 0012, VR-7 and NLR-1) obtained under identical test conditions (Mach number, Reynolds number, etc.). Because computation of the empirical parameters based on present methodology involves use of static airfoil characteristics, the resulting values of some of these empirical parameters may be dependent on the static airfoil characteristics. Figure 31a shows the various geometric characteristics for the four airfoils. The corresponding static airfoil characteristics are shown in Fig. 31b. At present, it is believed that the effects of airfoil shape can be adequately accounted for by a generalization of the various empirical parameters in terms of the Fig. 31a geometric characteristics (C_b, r_o, t/c) obtained from Table 2 of Ref. 5. Among the four airfoils represented in Fig. 31a, there is only one uncambered airfoil (NACA 0012). Also, the VR-7 airfoil referred in Fig. 31a has a -3.0 degree tab. This tab represents an additional geometric parameter, but it is assumed here that effects of the tab are indirectly represented through camber.

Figure 32a and 32b illustrate the variation of the computed empirical parameters P's and Q's (corresponding to the unsteady lift coefficient, Table III) with these four airfoil shapes, which are seen to have a significant effect on the magnitude of these parameters. Since there are at least three geometric parameters (C_b, r_o and t/c) and there are only four available values of each P or Q, determination of the correct generalized P's and Q's from the present data is not feasible. It is believed that the empirical parameters for additional airfoils are required to establish and verify the resulting generalized parameters. For example, the available NASA Ames test data (Ref. 5) for airfoils AMES-01, WORTMAN 098, HUGHES HH02 and NLR-7301 can be utilized to obtain the additional sets of empirical data. At present, the synthesis results for these airfoils are not available.

Even though the generalization with the geometric parameters such as camber, leading edge radius, and thickness ratio is not feasible at the present stage, Figs. 32a and 32b can be used to study the trends of the empirical coefficients. A further analysis of the results in Figs. 32a and 32b indicates that variation of the parameters P_1, P_2, Q_1, Q_2, Q_3 and Q_4 with airfoil shape is similar to the variaion of the static lift-curve slope with the airfoil shape (Fig. 31b). This result suggests that an alternative procedure may be utilized to generalize some of the parameters. Under this procedure the generalized parameters can be expressed in terms of the static airfoil characteristics (e.g., a_{oL}, α_{ss}, etc.) instead of the geometric characteristics (C_b, r_o, t/c). The alternate procedure is expected to be simpler but less accurate than the original procedure. Furthermore, the alternate procedure may not work for some of the empirical parameters (e.g., Q_5, Q_6 and Q_7 in Fig. 32b), becuase these parameters physically do not relate to the airfoil static characteristics in any way, but are solely associated with the dynamic stall phenomenon. For example, as previously mentioned, the parameter Q_7 is associated with the leading edge stall vortex, and therefore, its value is expected to depend significantly on geometric characteristics such as the leading edge radius or the thickness ratio.

The similar variation of unsteady pitching moment empirical parameters (η's in Table IV) for various airfoils are shown in Fig. 33. Once more the values of the η's, in general, vary significantly with the airfoil shape, but the results in Fig. 33 also indicate that contribution of some of the η's (like η_2, η_3, η_4) to the total unsteady C_{Mu} (Eqs. (31)-(32)) is very small. The only significant η's seem to be η_1, η_5, η_6 and η_7. Therefore, only four η's need to be generalized. The same argument is also valid for the unsteady drag parameters (R's in Table V). The only R's that need to be generalized are the R_1, R_5, R_7 and R_8 with the vortex-related parameters R_8 being of the most significance.

The variation of the leading-edge stall-vortex-related parameters Q_7, η_7 and R_8 (corresponding to unsteady lift, pitching moment and drag coefficient respectively) with airfoil shape is further illustrated in Fig. 34. The

important thing to note in Fig. 34 is that all three parameters (Q_7, η_7 and R_8) vary in a similar fashion with the airfoil shape; especially the variation of R_8 which is almost the same as that of $-\eta_7$. This reiterates the fact that incremental loads corresponding to the parameters Q_7, η_7 and R_8 are mainly due to the suction effect of the leading-edge stall-vortex.

Variation with Mach Number and Reynolds Number

An analysis of the results presented in Tables II through V indicates that the values of the empirical parameters, in general, vary significantly with Mach number and Reynolds number. The value of Mach number directly affects the nature or type of stall (e.g., leading edge, trailing edge or shock-induced stall) that occurs on the airfoil. At low values of Reynolds number (e.g., $R_n < 4 \times 10^6$), the effect of Reynolds number seems to be significant. At high values, the Reynolds number effects normally level out. For most of the data sets given in Table I, Reynolds number is less than 4.0×10^6.

In the case of oscillating airfoil experiments conducted in wind tunnels, the Reynolds number normally varies with Mach number. For example, in data sets 1 through 6 presented in Table I, the variation in Reynolds number with Mach number is $R_n \simeq 14 \times 10^6$ M. As a result, it becomes difficult to determine individual effects of Mach number and Reynolds number on the values of the various empirical parameters presented in Tables II through V. Figure 35 illustrates some of the effects of variation in Reynolds number and Mach number on the dynamic stall behavior of an airfoil. It is seen that the airfoil dynamic stall angle, α_{Dm} varies significantly with both of these parameters (Mach number and Reynolds number). At very low Mach numbers ($M \leq 0.18$, in panels a, b, and c), the increase of α_{Dm} from 17.9 degrees to 21.1 degrees is mainly due to the increase of R_n from 0.5×10^6 to 2.5×10^6. The effect of the variation in M on α_{Dm} is negligible in this range of Mach numbers ($M \leq 0.18$), but when Mach number is increased from 0.18 (panel c, $R_n = 2.5 \times 10^6$) to 0.30 (panel d, $R_n = 3.8 \times 10^6$) the value of α_{Dm} drops from 21.1 degrees to 17.0 degrees although there is a further increase in Reynolds number. Thus, in this range ($M > 0.18$, $R_n > 2.5 \times 10^6$), the Mach number effect on α_{Dm} is relatively much more significant than the Reynolds number effect.

Figure 36 shows a typical case of the variation in static aerodynamic characteristics with Mach number. The results presented here correspond to data sets 7 through 9 in Table I. Also shown in Fig. 36 is the variation of Reynolds number with Mach number. As these results indicate, the lift-curve slope normally increases with increasing Mach number and the static stall angle normally decreases with increasing Mach number. The corresponding variation in unsteady aerodynamic characteristics with Mach number is shown in Fig. 37. In the case of the results presented in Fig. 37, most of the

empirical parameters (all P's and Q's, except P_1 and Q_1) vary smoothly with Mach number (or Reynolds number), but at present the available bodies of synthesized data (sets 1 through 17 in Table I) are insufficient for the generalization with Mach number or Reynolds number. Therefore, no such generalization of the data has been successfully completed.

Variation with Aerodynamic Sweep

It has been shown before by empirical means (Ref. 2) that the aerodynamic sweep has a significant effect on unsteady stalled airfoil characteristics. Under the present formulation, the effects of sweep are represented by an appropriate variation in the values of the various empirical parameters (P's, Q's, η's and R's). For example, when the values of the empirical parameters corresponding to data set number 12 are compared with those corresponding to data set number 14, the change in the values of these parameters represents the net effect of sweeping the NACA 0012 wing by 30 degrees at Mach number of 0.3.

An analysis of the results corresponding to data sets 12 through 14 in Tables III-V indicates that the values of the empirical parameters associated with the nondimensional pitch rate A (P_1, Q_1, η_1 and R_1) are significantly affected by the sweep. This fact is further illustrated by the results shown in Fig. 38. This figure also shows the variation of the dynamic stall vortex-related parameters (Q_7, $-\eta_7$, R_8) with the sweep. Physically, Q_7 (for example), represents the effects of the distance between the stall vortex and airfoil surface on integrated lift coefficient. This is so because the effects of the vortex strength (proportional to α_{Dm}^2) on the integrated lift coefficient have been already accounted for by the appropriate normalization of Q_7 with α_{Dm}^2 (Eq. 27). The absolute value of all the vortex-related parameters decreases with the inclusion of sweep. This result implies that the overall integrated vortex distance effects for the swept airfoils are lower in magnitude than those for the unswept wing. Physically, the value of this integrated effect depends on the nature of interaction between the stall vortex and the airfoil geometry. In the case of two-dimensional unswept wings, the axis of the vortex at initiation is parallel to the wing leading edge. The evidence above suggests that the one way the swept wing can produce smaller values of the parameter associated with the distance effects is that the vortex at initiation is now skewed relative to the wing leading edge. Since airloads for both the swept and unswept cases have been computed by integrating pressures along a line normal to the leading-edge, the computed vortex suction airloads corresponding to the same strength vortex should be relatively less for the case of the swept airfoil. Therefore, the values of the empirical parameters like Q_7, $-\eta_7$ and R_8 are expected to decrease with the increasing wing sweep angle.

DEVELOPMENT OF UNSTEADY AERODYNAMICS MODULE FOR ROTOR APPLICATIONS

As shown earlier, a practical model for the unsteady aerodynamic characteristics of two-dimensional airfoils has been established, and this methodology was extended to the prediction of helicopter rotor blade airloads as a next logical step. For this purpose a general computer module has been developed that simulates the rotor blade section in a realistic way and accurately computes the unsteady airloads. The module accounts for the fact that the rotor blade section goes through time varying changes in not only the angle of attack but also in Mach number and the aerodynamic sweep angle. The module has been developed in such a way that it can be coupled to any rotor airloads analysis with a time history solution. To check the operation of the module, and also to demonstrate the capabilities of the present model of the unsteady aerodynamics, this unsteady aero-module was incorporated in the G400 (G400PA version for SIMVIB, Ref. 15) aeroelastic rotor analysis developed at UTRC. Also a limited correlation of the predicted results with the flight test data has been carried out. The G400 computer program is a normal modes analysis, and detailed information on the analysis can be found in Ref. 16.

Description of Unsteady Aerodynamics Module

This section describes briefly the basic structure of the computer module and also provides a procedure for incorporating the module in various rotor airloads analyses. Figure 39 describes the flow chart of the computer module and its coupling with an aeroelastic analysis (G400, for example). It should be remembered that the present method computes, in the time domain, the unsteady lift, pitching moment, and drag coefficients of a blade airfoil section by utilizing instantaneous values of the dynamic parameters (the instantaneous angle of attack, α, the nondimensional pitch rate, A, and the unsteady decay, α_w) together with the static airfoil data (Eqs. (23)-(36)). The angle of attack, α is computed conventionally for the blade section (See Eq. (10)), and in the present example (Fig. 39), it is computed in subroutine SPANS. Subroutines ALFDOT and ALWCOM calculate the dynamic parameters A and α_w, respectively, according to Eqs. (11)-(15). Subroutine UNSTCF uses the instantaneous parameters α, A and α_w and Eq. (18) to predict the possible occurrence of dynamic stall (See Fig. 5). It also acquires appropriate empirical parameters (the P's, Q's, η's, etc. corresponding to the section airfoil shape, Mach number and aerodynamic sweep angle) by calling subroutine COEFF3. The actual computation of the unsteady aerodynamic coefficients (C_{Lu}, C_{Mu}, C_{Du}) is carried out in subroutines SYNTH3 according to Eqs. (23)-(36). The static data (C_{LS}, C_{MS}, C_{DS}) required in Eqs. (23), (31), and (33) are obtained from the built-in data by calling subroutines GETCLS, GETCMS and CETCDS, respectively. Or optionally a user can provide

his own static data instead of using the built-in static data (Option 2 in Fig. 39). The built-in static data are the static data that were used during synthesization for obtaining the empirical parameters.

Application to Full Scale Helicopter

The present model of the unsteady aerodynamics has been used to compute the CH-53A helicopter rotor blade airloads (Ref. 17) for a 137 knots condition. The CH-53A blade section airfoil (NACA 0011) is similar to the NACA 0012 airfoil; therefore it was assumed that the empirical parameters corresponding to the NACA 0012 can be utilized to compute the airloads. However, for accurate prediction of these unsteady airloads (specifically during the high speed forward flight operation), the NACA 0012 empirical parameters (P's, Q's, η's, R's, etc.) at a full range of Mach numbers, Reynolds numbers and sweep angles are required. Most of the wind tunnel data that have been analyzed (Table I) are in the 0.2 to 0.6 Mach number range. During high speed forward flight, Mach numbers of some blade sections were expected to reach values below 0.1. Before the present method was applied to the CH-53A helicopter, it was considered necessary to obtain the NACA 0012 empirical parameters at lower Mach numbers. Reference 5 contains a limited amount of test data for the NACA 0012 airfoil obtained at Mach numbers 0.04 and 0.07. These test data were utilized to obtain the approximate values of the required low Mach number empirical parameters.

Because the empirical parameters at full scale Reynolds numbers were, in general not available, the Reynolds number effects were essentially neglected during the present computations. Furthermore, the aerodynamic sweep effects were confined to the Mach number range of 0.3 to 0.4 and the sweep angle range of 0 to 30 degrees. More specifically, the present computations have been carried out with the empirical parameters corresponding to data sets 5, 9 and 12-15 in Table I. In general, when the blade section aerodynamic parameters fell outside the available empirical data range, the conventional quasi-steady methods were used to compute the airloads even though this procedure caused discontinuities in the time histories of the lift, pitching moment and drag coefficients.

The computations for the CH-53A aircraft rotor were carried out at a high blade load $C_T/\sigma = 0.083$, gross weight = 41,000 lbs, high speed ($\mu = 0.323$, V = 137 knots) condition; and the helicopter was assumed to be flying at 3000 feet density altitude. These conditions were chosen for the computations because the flight test data for this case are available in Ref. 17 (case number 52) and also because the earlier analytical results (Ref. 1) corresponding to this case are available. As a result, the various improvements in the correlation between flight test data and the results of the analytical computations (using

the G400 Aeroelastic Analysis, Ref. 15) can be systematically demonstrated. It should be remembered that the earlier analytical computations (Ref. 1) were based on a preliminary model of unsteady aerodynamics that omitted the computation of unsteady drag coefficient, and also included the approximation that flow reattachment on an airfoil occurs when the angle of attack drops to the static stall angle. Normally for low Mach numbers ($M \leq 0.4$) the reattachment always occurs at an angle less than the static stall angle (see Figs. 6-8). The inclusion of the improved reattachment representation and unsteady drag calculations in the present model were expected to provide a better correlation between analytical predictions and the measured full scale helicopter blade data.

The correlation of the test CH-53A blade airloads (lift) with the predicted results is shown in Fig. 40. The predicted results match within $\pm$ 6 lb/in. with the test data when the blade is on the retreating side including when it goes through dynamic stall. A comparison of the present analytical results with those obtained earlier (Ref. 1) shows only a small change in the values of the computed airloads. The local lack of agreement near $\psi \cong 90$ and 180 deg appears to be associated with the sensitivity of the predicted airloads to small changes in the computed upwash ($\psi \cong 90$ deg) or to blade vortex interactions ($\psi \cong 180$ deg). These discrepancies in airloads are further discussed in the following paragraphs with reference to the results of flatwise stress correlations.

Figure 41 shows the pitch link load correlation between the test and theory. The occurrence of dynamic stall is predicted reasonably well as indicated by the correlation of the pitch link loads on the retreating side. The test data show a peak to peak variation in the dynamic stall azimuthal range (180° to 360°) of about 4,000 lbs. The theory underpredicts this by 20 percent, does not detect the minimum peak at $\psi = 230°$, but otherwise predicts both the magnitude and phase trends of the data. This figure also illustrates the significant improvement in the pitch link load correlation during dynamic stall due to the use of the correct dynamic reattachment angle instead of the static stall angle. These results clearly indicate that for predictions carried out with the proper reattachment model, the rotor blade emerges from the dynamic stall at a later time than that for the case of computations with α_{ss} as the reattachment angle.

Measured and computed blade stresses for the same condition are compared in Figs. 42 and 43. From the results shown for the edgewise stresses (Figs. 42a and 43a), it is seen that very good agreement between test and theory has been obtained over the complete range of azimuth. This excellent agreement is partly due to inclusion of unsteady drag in the present computations. The corresponding correlation obtained for flatwise stresses, as shown in Figs. 42b and 43b, is not as good as that for edgewise stresses. The magnitudes of the CH-53A flatwise stresses are normally smaller than those of edgewise

stresses, and flatwise stresses are much more sensitive to the blade airloads than the edgewise stresses. As mentioned earlier, the correlation for the blade airloads on the advancing side of the rotor is poor (Fig. 40). A further analysis of the results, however, indicates that the angle of attack distribution on the advancing side was not predicted accurately. For example, Fig. 44 shows the predicted angle of attack variation with azimuth corresponding to the blade section at 70 percent radius. The predicted value of the angle of attack at 90 degrees azimuth is close to zero, while the test data indicate a negative value of α. As discussed first in Ref. 1, the analysis includes a variable inflow based on a classical undistorted wake model which apparently over-predicts the amount of upwash on the advancing side for this case. For this case, the aircraft center-of-gravity position was such to produce a rotor tip path plane angle of attack less than 2 degrees, and thus a significant number of blade vortex interactions occurred and were predicted by the variable inflow program. The use of an undistorted wake model and limitations of the modeling of close blade vortex interactions introduces inaccuracies in the description of the variable inflow and resultant airloads. For example, the predicted airloads do not match test results near 180 degree azimuth as shown in Fig. 40.

Figure 44 also shows the Mach number variation with azimuth, and the corresponding computed azimuthal distributions of the unsteady aerodynamic characteristics of a representative blade section are shown in Fig. 45. Shown in both of these figures are the instants when the onsets of stall and the corresponding reattachments occur. For this blade section, stall first occurs at $\psi = 214°$ (S_1). The reattachment of the flow following this stall occurs at $\psi = 280°$ (R_1). Subsequent to this, this blade section experiences second stall at $\psi = 308°$ (S_2) and the reattachment of the flow again occurs at $\psi = 350°$ (R_2). As the results shown in Fig. 45a indicate, the blade section lift coefficient reaches a value as high as 1.7 after the inception of stall. Such large values of lift coefficient cannot be predicted from the conventional quasi-steady theories.

Shown in Fig. 45c are plots of the unsteady drag analytically computed by two different procedures, both using the same static data: the solid line represents the drag computed by using Eqs. (33)-(34), and the dashed line is the drag obtained from the conventional quasi-steady theory. This comparison further illustrates the failure of the quasi-steady theory to predict the large values of these airloads.

CONCLUSIONS AND RECOMMENDATIONS

The UTRC synthesized unsteady data method has been significantly expanded and improved under the present study. Nine sets of unsteady drag data were synthesized. This provided a basis for the successful expansion of the method to include the computation of unsteady pressure drag. Also, under the present study, an improved reattachment prediction model was incorporated in the method. Application of this improved unsteady aerodynamics model has resulted in a better correlation of analytic predictions with measured full scale helicopter blade stress data. The following are specific conclusions obtained from an analysis of results presented in this report.

1. The present unsteady aerodynamic model predicts within $\pm$ 0.5 degrees the onset of dynamic stall for most of two-dimensional airfoils as well as for rotor blades.

2. The synthesized unsteady lift, pitching moment and drag coefficient hysteresis loops match very well with the two-dimensional test data.

3. The present prediction method is well suited for realistically simulating the aerodynamic loads on a rotor blade due to the azimuthal variation in angle of attack.

4. It is feasible to predict the empirical parameters embedded in the present method dependence on Mach number, airfoil shape and sweep angle if sufficient data were available.

5. The empirical parameters, corresponding to the various bodies of data sets synthesized to date, were found to be insufficient for successful generalization of the parameters.

6. In general, the predicted stall airloads for a CH-53A helicopter rotor blade correlation with the test data is improved by the present version of the unsteady aerodynamics model.

7. Inclusion of unsteady drag computations in the present method results in improved correlation between the predicted edgewise stresses and the measured data.

8. A significant improvement in the pitch link load correlation during dynamic stall is obtained through the use of the correct dynamic reattachment angle instead of the static stall angle.

The following future activities are recommended:

1. Reference 18 contains unsteady data for the NLR-1 airfoil in the Mach number range 0.2 to 0.7. It also contains data for a set of test conditions in which the Mach number was maintained constant while varying the Reynolds number. Thus the effect of Reynolds number on the empirical parameters can be determined explicitly. Therefore it is recommended the Ref. 18 test data should be synthesized.

2. The Ref. 5 test data for four additional airfoils are available. The synthesization of these data should be carried out and the results should be combined with those of the four present airfoils to determine the effect of airfoil shape on empirical coefficients.

3. Additional correlation studies involving use of the present method should be conducted.

REFERENCES

1. Gangwani, S. T.: Prediction of Dynamic Stall and Unsteady Airloads on Rotor Blades. Journal of the American Helicopter Society, Vol. 27, No. 4, October 1982, pp. 57-64. Also Preprint No. 81-1, American Helicopter Society, 37th Annual National Forum, New Orleans, May 1981.

2. St. Hilaire, A. O., F. O. Carta, M. R. Fink and W. D. Jepson: The Influence of Sweep on the Aerodynamic Loading on an Oscillating NACA 0012 Airfoil. Volume I - Technical Report. NASA CR-3092, 1979.

3. McAlister, K. W., L. W. Carr and W. J. McCroskey: Dynamic Stall Experiments on the NACA 0012 Airfoil. NASA TP-1100, 1978.

4. Carr, L. W., K. W. McAlister, and W. J. McCroskey: Analysis of the Development of Dynamic Stall Based on Oscillating Airfoil Experiments. NASA TN D-8382, 1977.

5. McCroskey, W. J., K. W. McAlister, L. W. Carr, S. L. Pucci, O. Lambert and R. F. Indergand: Dynamic Stall on Advanced Airfoil Sections. Preprint No. 80-1, American Helicopter Society, 36th Annual National Forum, Washington, D.C., May 1980.

6. Gray, L. and J. Liiva: Two-Dimensional Tests of Airfoils Oscillating Near Stall, Vol. II, Data Report, USAAVLABS TR-68-13B, USAAMRDL Ft. Eustis, Va., April 1968.

7. Gormont, R. E.: A Mathematical Model of Unsteady Aerodynamics and Radial Flow for Application to Helicopter Rotors. USAAMRDL TR 72-67, May 1973.

8. Carlson, R. G., G. L. Commerford and P. H. Mirick: Dynamic Stall Modeling and Correlation with Experimental Data on Airfoils and Rotors. Presented at the AHS/NASA Specialists' Meeting on Rotorcraft Dynamics, NASA SP-352, Rotorcraft Dynamics, Paper 2. February 1974.

9. Bielawa, R. L.: Synthesized Unsteady Airfoil Data with Applications to Stall Flutter Calculations. Preprint No. 935. Proceedings of the 31st Annual National Forum of American Helicopter Society, May 1975.

10. Beddoes, T. S.: A Synthesis of Unsteady Aerodynamic Effects Including Stall Hysteresis. Vertica, Vol. 1, pp. 113-123, 1976.

REFERENCES (Cont'd)

11. Bisplinghoff, R. L., H. Ashley, and R. L. Halfman: Aeroelasticity. Addision-Wesley Publishing Company, Inc., 1957.

12. Menzel, D. H.: Fundamental Formulas of Physics. Volume One, Dover Publications, Inc., 1960.

13. Beddoes, T. S.: Onset of Leading Edge Separation Effects Under Dynamic Conditions and Low Mach Number. Preprint No. 78-63, American Helicopter Society, 34th Annual National Forum, Washington, D. C., May 1978.

14. Lambourne, N. C.: Experimental Techniques in Unsteady Aerodynamics. AGARD Report No. 679, Special Course on Unsteady Aerodynamics, pp. 10, March 1980.

15. Sopher, R., R. E. Studwell, S. Cassarino and S. B. R. Kottapalli: Coupled Rotor/Airframe Vibration Analysis, NASA CR-3582, 1982.

16. Bielawa, R. L.: Aeroelastic Analysis for Helicopter Rotor Blades with Time-Variable, Nonlinear Structural Twist and Multiple Structural Redundancy. NASA CR-2638, 1976.

17. Beno, E. A.: CH-53A Main Rotor and Stabilizer Vibratory Airloads and Forces. SER 65593, Contract No. 63-1050-f, Department of the Navy, Naval Air Systems Command, Washington, D. C., June 1970.

18. Dadone, L. U.: Two-Dimensional Wind Tunnel Test of an Oscillating Rotor Airfoil - Volume II. NASA CR-2915, 1977.

19. Hildebrand, F. B.: Advanced Calculus for Applications. Prentice-Hall, Inc., 1962.

TABLE I

LIST OF TEST DATA USED IN SYNTHESIS

Data Set No.	Source Ref. No.	Airfoil Type	Mach No.	Reynolds No. x 10^{-6}	Parametric Range of Test Data Used		
					k	α_o	$\bar{\alpha}$
1	5	SC 1095	0.30	3.8	0.0-0.20	5-15	5-10
2	5	NACA 0012	0.30	3.8	0.0-0.20	5-15	5-10
3	5	VR-7	0.30	3.8	0.0-0.20	5-15	5-10
4	5	NLR-1	0.30	3.8	0.0-0.20	5-15	5-10
5	5	VR-7	0.18	2.5	0.0-0.25	5-15	10
6	5	NACA 0012	0.18	2.5	0.0-0.25	5-15	6-14
7	6	V0012	0.20	2.6	0.0-0.38	5-17.5	2.5-7.5
8	6	V0012	0.40	4.8	0.0-0.31	5-15	2.5-7.5
9	6	V0012	0.60	6.2	0.0-0.25	5-10	5.0-7.5
10	6	V2301-1.58	0.40	4.8	0.0-0.25	5-15	5.0-7.5
11	6	V2301-1.58	0.60	6.2	0.0-0.25	5-10	2.5-7.5
12	2	NACA 0012	0.30	2.8	0.0-.125	0-15	8-10
13	2	NACA 0012	0.40	3.7	0.0-.100	0-15	8-10
14	2	YAWED 0012	0.30	3.2	0.0-.125	0-15	8-10
15	2	YAWED 0012	0.40	4.3	0.0-.100	0-15	8-10
16	*	SC 1095	0.30	2.8	0.0-.125	0-15	8
17	*	SC 1095	0.40	3.7	0.0-.100	0-15	8

*Sikorsky Aircraft was kind enough to allow the use of data sets 16 and 17. These data sets are not available for general public use.

TABLE II

EMPIRICAL DATA FOR PREDICTING DYNAMIC STALL EVENTS
(See Eqs. (18)-(20))*

Data Set No.	α_{ss} deg	α_{qs} deg	ϵ -	$\bar{C}_{Am}$ /deg	$\bar{C}_{wm}$ /deg	C_{At} /deg	$C_{\alpha t}$ /deg	$\bar{C}_{AR}$ /deg	$\bar{C}_{wR}$ /deg
1	12.5	14.0	.120	2.29	0.52	.117	.0071	1.692	-1.238
2	12.0	13.5	.125	3.64	-.05	.084	.0073	1.790	-0.743
3	12.0	13.0	.083	4.76	0.45	.158	.0032	0.882	-0.674
4	11.5	12.5	.087	4.29	0.30	.122	.0111	3.884	-1.053
5	12.0	13.0	.083	1.87	1.36	.051	.0041	6.666	-2.769
6	12.0	14.5	.208	3.63	1.42	.135	.0016	-1.450	0.667
7	12.0	13.0	.083	8.86	0.22	.027	.0088	9.062	-3.527
8	9.0	10.0	.111	2.97	1.27	.065	.0090	2.979	-1.344
9	5.6	6.0	.071	2.66	1.98	-.09	.0218	3.365	-1.166
10	12.0	13.5	.125	4.14	0.28	.134	.0048	2.302	-1.520
11	6.0	7.0	.167	2.20	1.67	-.05	.0193	3.916	-0.830
12	11.0	12.5	.136	1.57	1.18	.024	.0093	3.385	-1.637
13	9.0	10.0	.111	3.17	0.79	.144	.0043	2.938	-1.084
14	12.0	13.0	.083	2.60	0.64	.060	.0036	-1.141	-0.411
15	10.0	11.0	.100	3.59	0.45	.078	.0026	-3.401	1.188
16	11.0	12.0	.091	1.67	0.85	.046	.0091	0.924	-0.897
17	9.5	10.5	.105	2.80	0.62	.128	.0063	2.022	-0.532

* $\bar{C}_{Am} = C_{Am}\,\alpha_{ss}$

$\bar{C}_{wm} = C_{wm}\,\alpha_{ss}$

$\bar{C}_{AR} = C_{AR}\,\alpha_{ss}$

$\bar{C}_{wR} = C_{wR}\,\alpha_{ss}$

TABLE III

EMPIRICAL DATA FOR PREDICTING UNSTEADY LIFT COEFFICIENT
(See Eqs. (23)-(27))

Data Set No.	P_1 /rad	P_2 /rad	P_3 -	Q_1 /rad	Q_2 /rad	Q_3 -	Q_4 -	Q_5 -	Q_6 /rad	Q_7 /rad^2	RMS Error
1	15.982	4.427	-.1554	-1.265	0.1585	0.1521	-.2107	0.3055	5.973	7.557	0.0957
2	17.988	2.410	-.1661	1.8347	0.2123	- .0307	-.0966	0.7754	2.842	5.298	0.1166
3	15.311	2.929	-0.0676	-2.206	0.7660	0.1166	-.2148	0.5522	4.509	5.507	0.0858
4	21.436	1.519	- .1038	0.3247	1.0748	0.0547	-.1167	0.4395	4.290	7.084	0.1024
5	3.3522	8.836	- .0266	3.7316	-1.662	- .0470	-.1088	0.2724	5.947	4.244	0.1149
6	6.5034	9.997	- .2430	-.8700	-0.081	0.1881	0.2558	1.0104	2.569	3.685	0.1255
7	17.443	3.568	0.0	0.7869	1.7627	0.4921	-.6769	2.3851	-.640	5.399	0.1268
8	3.8401	10.715	0.0	2.1279	0.7838	- .0085	-.1412	0.7192	1.862	4.934	0.0815
9	18.584	12.042	0.0	-3.808	-2.553	- .0895	-.0001	0.3187	2.734	3.144	0.0644
10	10.162	11.144	0.0	-2.245	0.1809	0.1800	-.3666	0.7132	5.372	3.070	0.0998
11	14.079	11.645	0.0	-4.793	-3.289	- .0627	-.0100	0.3829	3.021	2.001	0.0635
12	18.991	5.139	- .2249	-3.271	-0.476	- .0226	-.0289	0.4990	4.119	3.926	0.0740
13	31.337	0.4182	- .0426	-8.906	0.4284	- .0579	0.0145	0.3025	4.680	4.156	0.0564
14	31.311	-0.779	0.0423	-12.161	5.129	- .0870	-.1010	1.3346	0.509	2.300	0.0713
15	40.844	-1.7404	0.2219	-22.621	7.536	- .2104	-.0288	0.9563	2.030	0.1113	0.0755
16	36.011	-2.2911	- .2083	-11.986	4.395	- .0869	-.0626	0.7090	3.452	8.215	0.0899
17	40.874	-1.088	- .1038	-18.879	5.030	- .0139	-.0539	0.2298	6.491	5.482	0.0763

TABLE IV

EMPIRICAL DATA FOR PREDICTING UNSTEADY PITCHING MOMENT COEFFICIENT
(See Eqs. (31)-(32))

Data Set No.	η_1 /rad	η_2 /rad	η_3 -	η_4 /rad	η_5 -	η_6 /rad	η_7 /rad^2	RMS Error
1	-1.452	-0.211	0.0065	-.3997	0.2792	-.8536	-8.492	0.0260
2	-1.782	-0.191	- .0035	-.0082	0.3462	-1.405	-6.354	0.0244
3	-1.789	-0.264	0.0139	-.4148	0.1962	-0.868	-5.915	0.0174
4	-1.809	-0.207	0.0131	-.3290	0.1846	-0.991	-11.306	0.0235
5	-1.538	-0.252	0.0179	-.2629	0.2156	-1.118	-2.869	0.0216
6	-1.463	-0.498	0.0078	-.3870	0.3537	-1.534	-2.102	0.0309
7	-1.279	1.0528	- .0056	0.0936	0.1571	-0.992	-0.919	0.0354
8	-0.4749	0.4371	0.0019	0.7460	0.0836	-1.068	-5.635	0.0249
9	-1.8311	- .0451	0.0108	-.1719	0.0702	-1.072	-3.724	0.0137
10	-1.1443	0.3079	- .0174	0.2748	0.1984	-0.964	-5.328	0.0224
11	-1.1814	- .1402	0.0008	-.0629	0.0601	-0.780	-3.018	0.0116
12	-1.8915	- .3657	0.0098	-.5893	0.3774	-1.819	-6.079	0.0196
13	-2.9763	0.0949	- .0079	-.3673	0.1904	-1.156	-5.161	0.0158
14	-0.4993	- .2690	- .0100	0.6278	0.0719	-0.513	-3.036	0.0224
15	0.3807	-1.054	0.0226	0.1313	0.1224	-0.864	-2.597	0.0209
16	-2.581	0.0782	0.0144	-.1881	0.3876	-1.819	-8.755	0.0191
17	-3.372	0.1571	0.0067	-.3321	0.2923	-1.288	-10.109	0.0186

TABLE V

EMPIRICAL DATA FOR PREDICTING UNSTEADY DRAG COEFFICIENT
(See Eqs. (33)-(34))

Data Set No.	R_1 /rad	R_2 /rad	R_3 /rad	R_4 /rad	R_5 -	R_6 -	R_7 /rad	R_8 /rad^2	RMS Error
1	0.8610	0.7974	-.0157	1.1037	-.4229	-.0784	2.346	12.796	0.0295
2	1.1333	0.7570	-.0046	1.1165	-.5366	0.6137	2.070	8.298	0.0359
3	2.5221	0.4035	-.0349	1.4359	-.6120	0.3344	2.751	7.354	0.0397
4	1.5329	0.5075	-.0172	0.9445	-.3771	0.6837	2.271	16.718	0.0289
5	1.3772	0.3013	-.0081	0.3621	-.2334	- .3143	1.837	5.674	0.0655
6	-	-	-	-	-	-	-	-	-
7	-	-	-	-	-	-	-	-	-
8	-	-	-	-	-	-	-	-	-
9	-	-	-	-	-	-	-	-	-
10	-	-	-	-	-	-	-	-	-
11	-	-	-	-	-	-	-	-	-
12	0.5224	1.0909	-.0024	1.0522	-.6792	0.4779	2.660	9.047	0.0273
13	2.0415	0.3391	-.0295	0.9797	-.3438	0.3417	2.126	8.035	0.0202
14	1.9358	- .0448	-.0325	0.4700	-.4952	0.1161	2.983	4.481	0.0463
15	2.0700	0.0924	-.0340	0.3144	-.4800	0.4159	2.871	4.408	0.0321
16	-	-	-	-	-	-	-	-	-
17	-	-	-	-	-	-	-	-	-

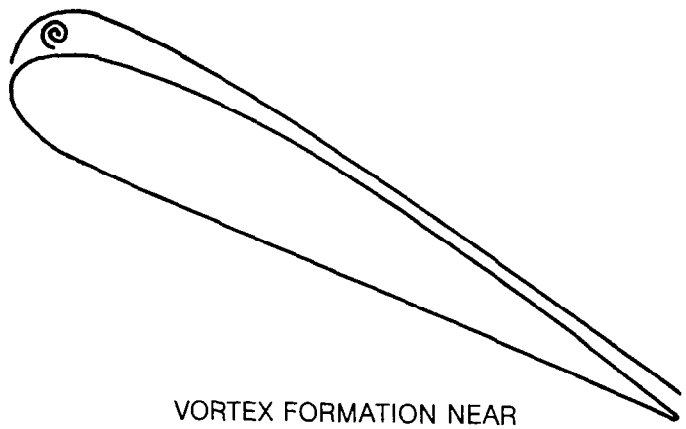

VORTEX FORMATION NEAR
LEADING EDGE

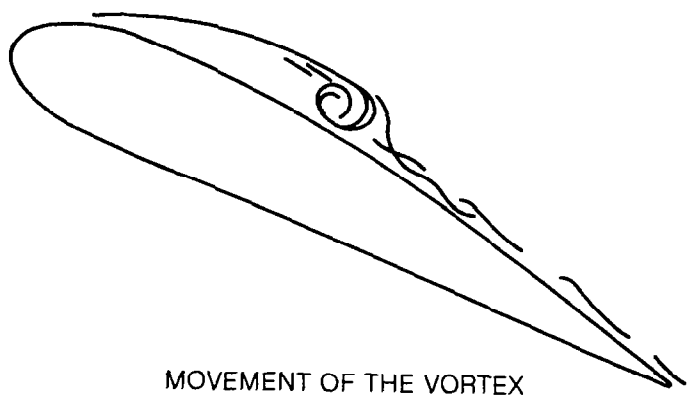

MOVEMENT OF THE VORTEX
OVER THE AIRFOIL

Figure 1. Dynamic Stall Modeling

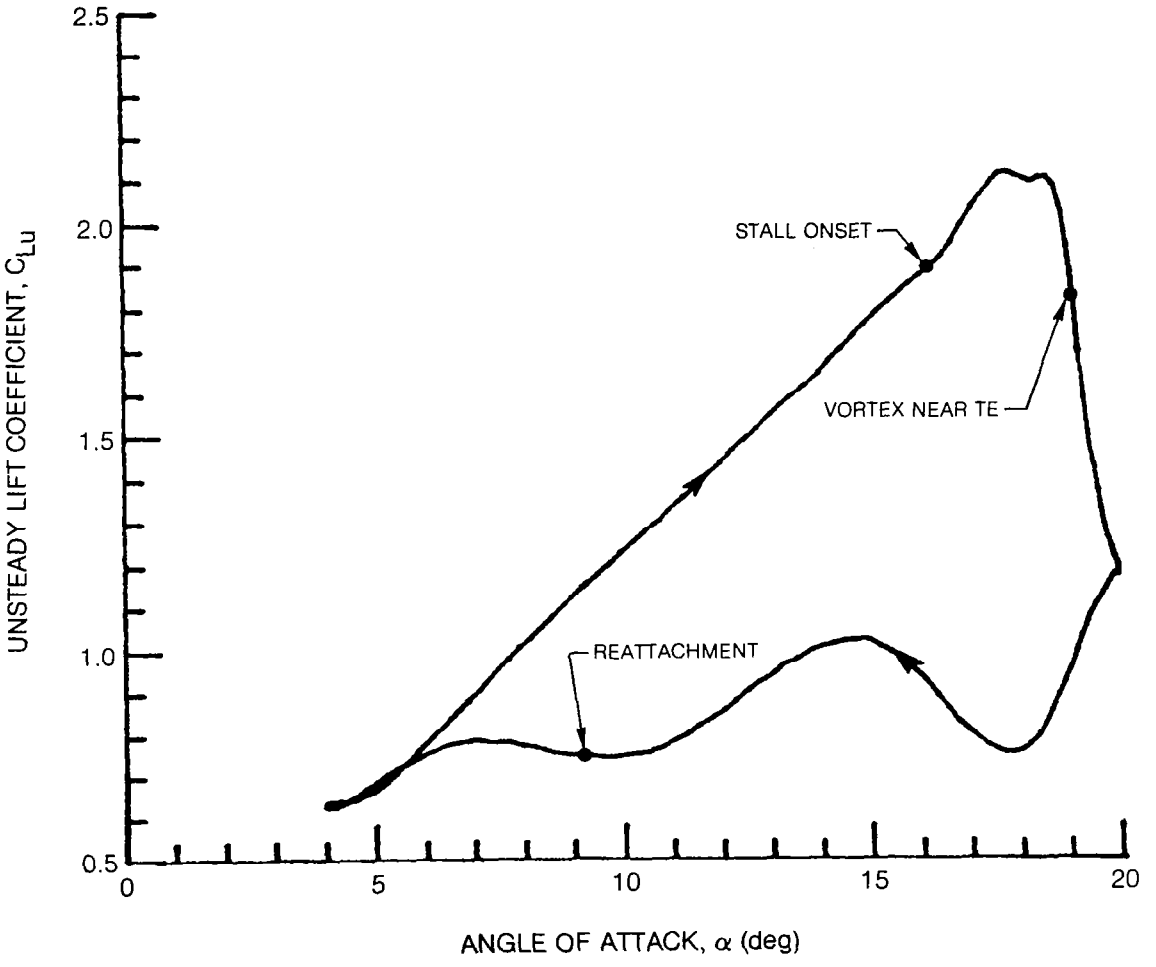

Figure 2a. Typical Unsteady Lift Coefficient Loop Data, SC 1095 Airfoil, M = 0.3, α_o = 12.0 deg, $\bar{\alpha}$ = 8.0 deg, k = 0.1

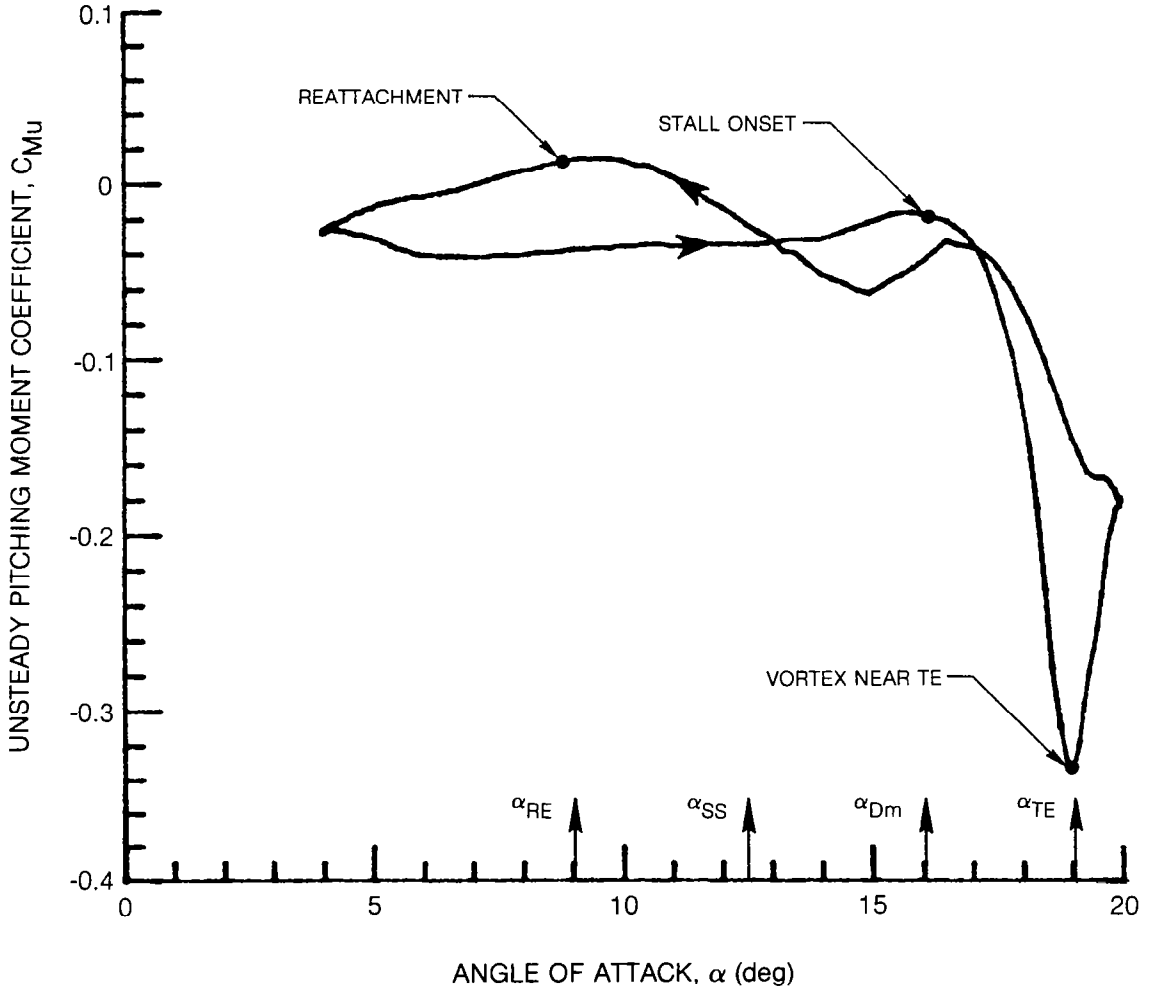

Figure 2b. Typical Unsteady Pitching Moment Loop Data, SC 1095 Airfoil, M = 0.3, α_o = 12.0 deg, $\bar{\alpha}$ = 8.0 deg, k = 0.1

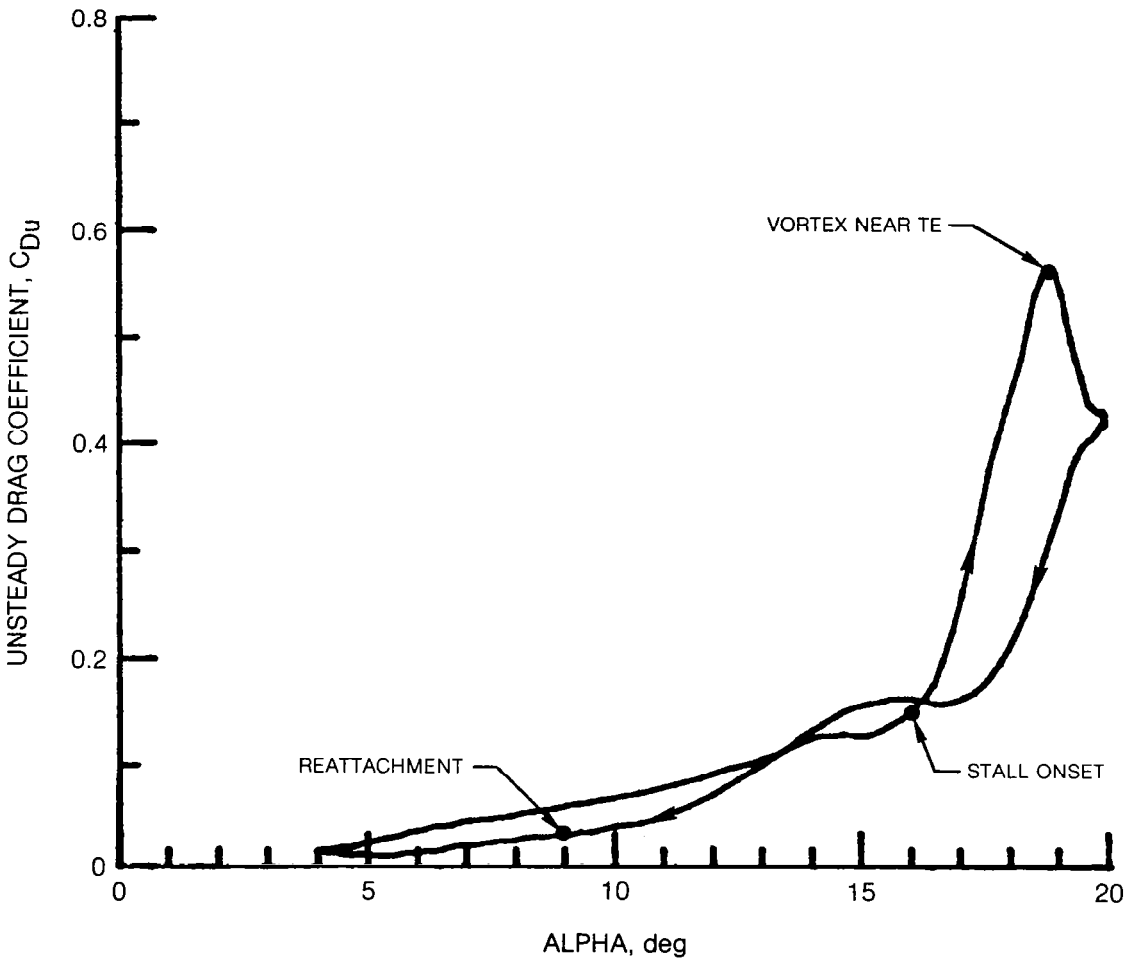

Figure 2c. Typical Unsteady Drag Coefficient Loop Data, SC 1095 Airfoil, M = 0.3, α_o = 12.0 deg., $\bar{\alpha}$ = 8.0 deg, k = 0.1

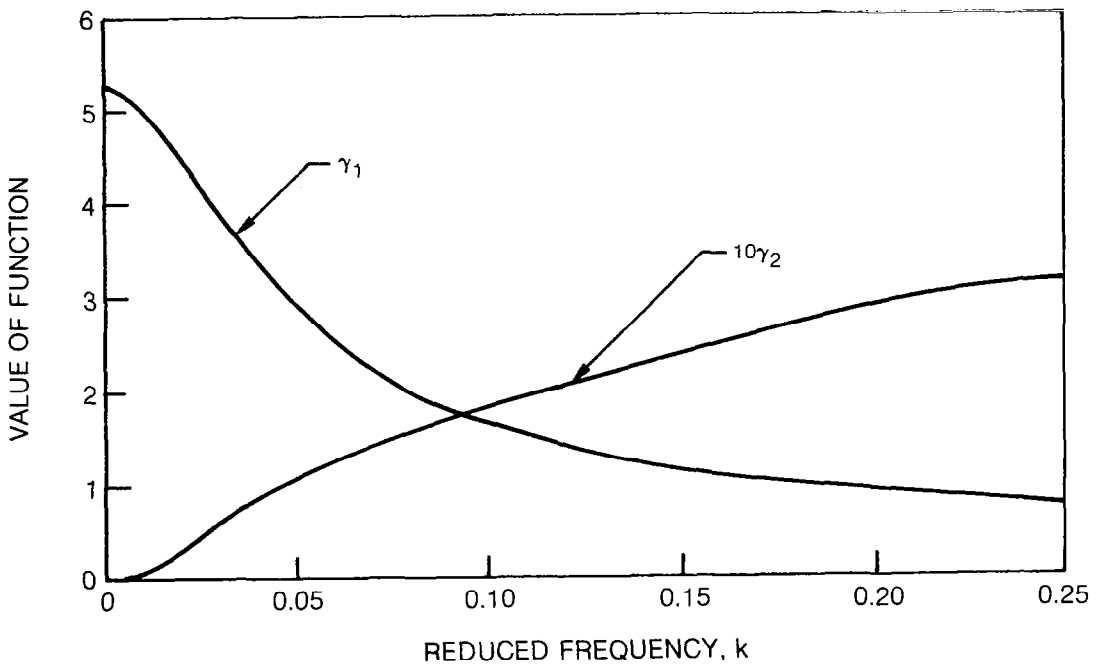

Figure 3. Variation of Functions γ_1 and γ_2 (Eqs. 8-9) with Reduced Frequency at Mach Number 0.3

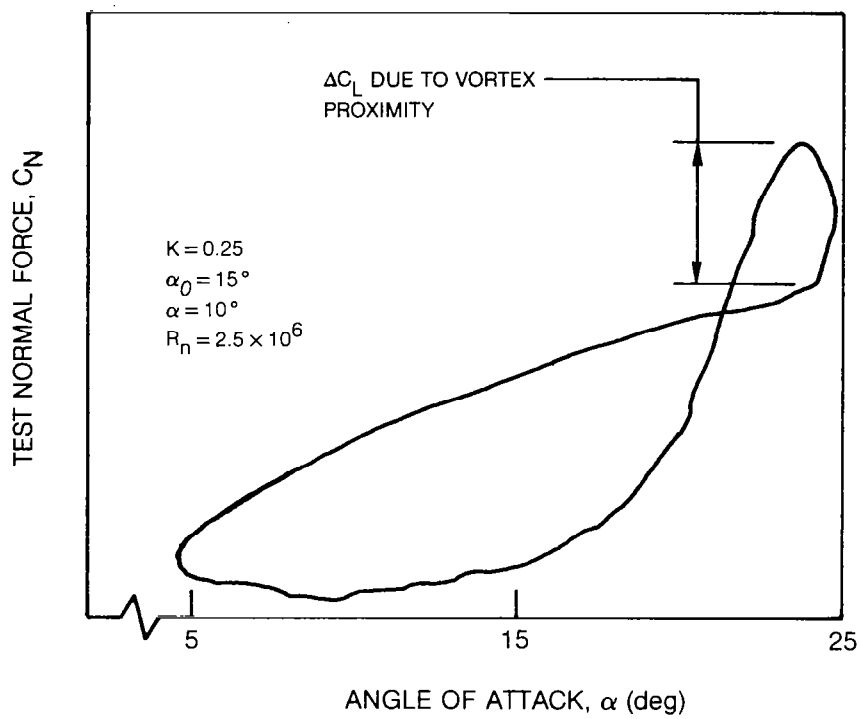

Figure 4. Test Normal Force on NACA 0012 at M = 0.09 (Reference 4)

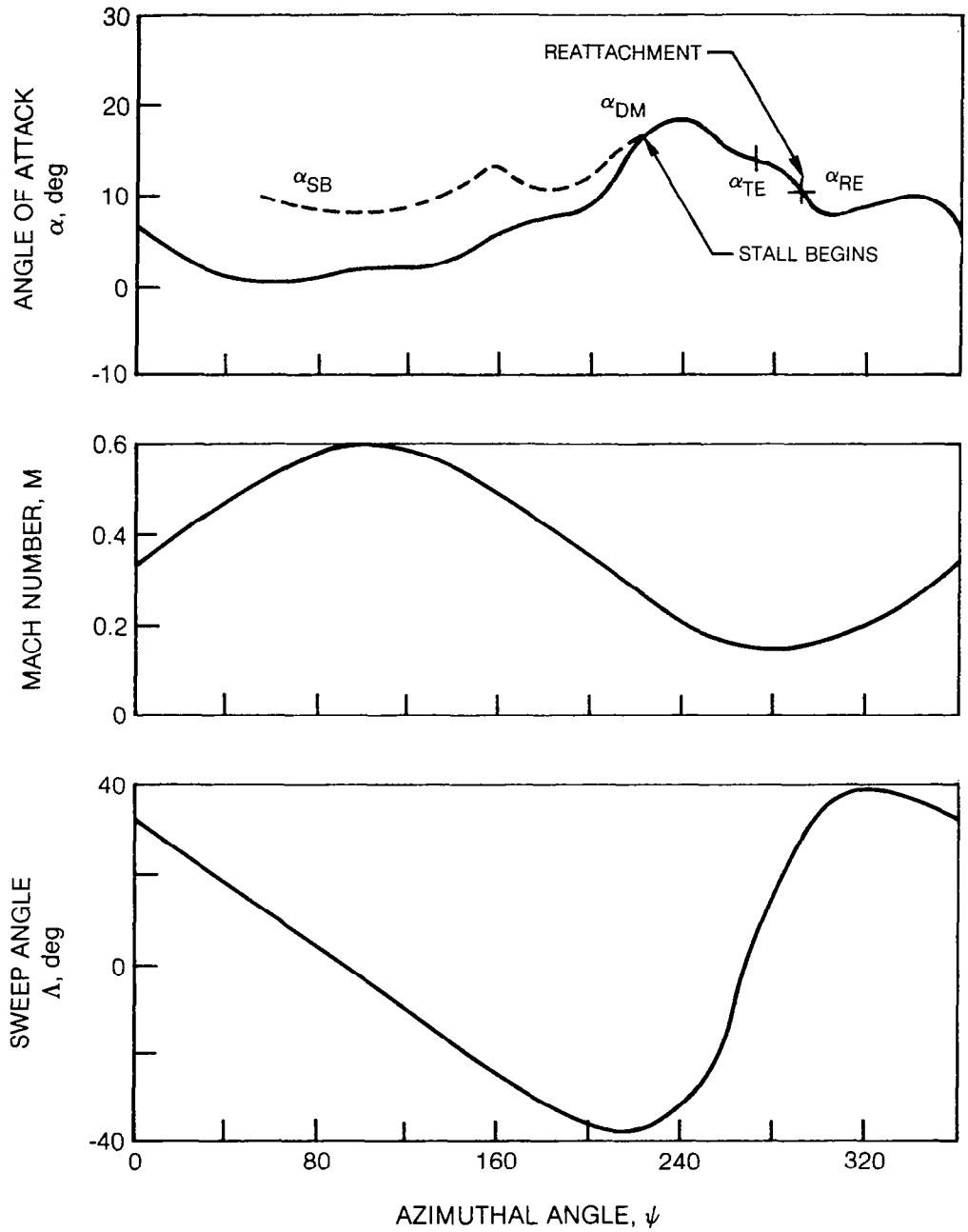

Figure 5. Prediction of Rotor Blade Dynamic Stall
V = 152 kts, ΩR = 685 fps, r/R = 0.6

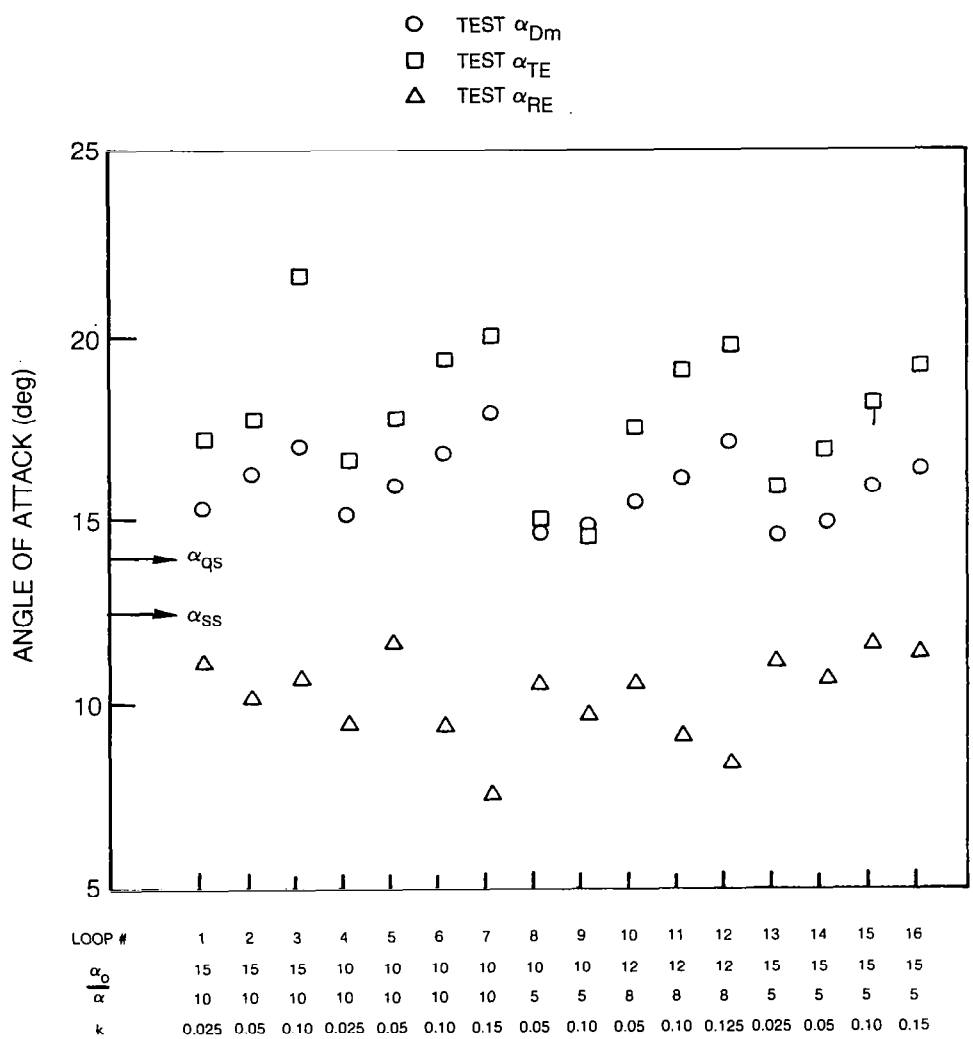

Figure 6. Variation of Stall Events with Test Parameters, SC 1095 Airfoil, M = 0.3, Data Set No. 1 in Table I

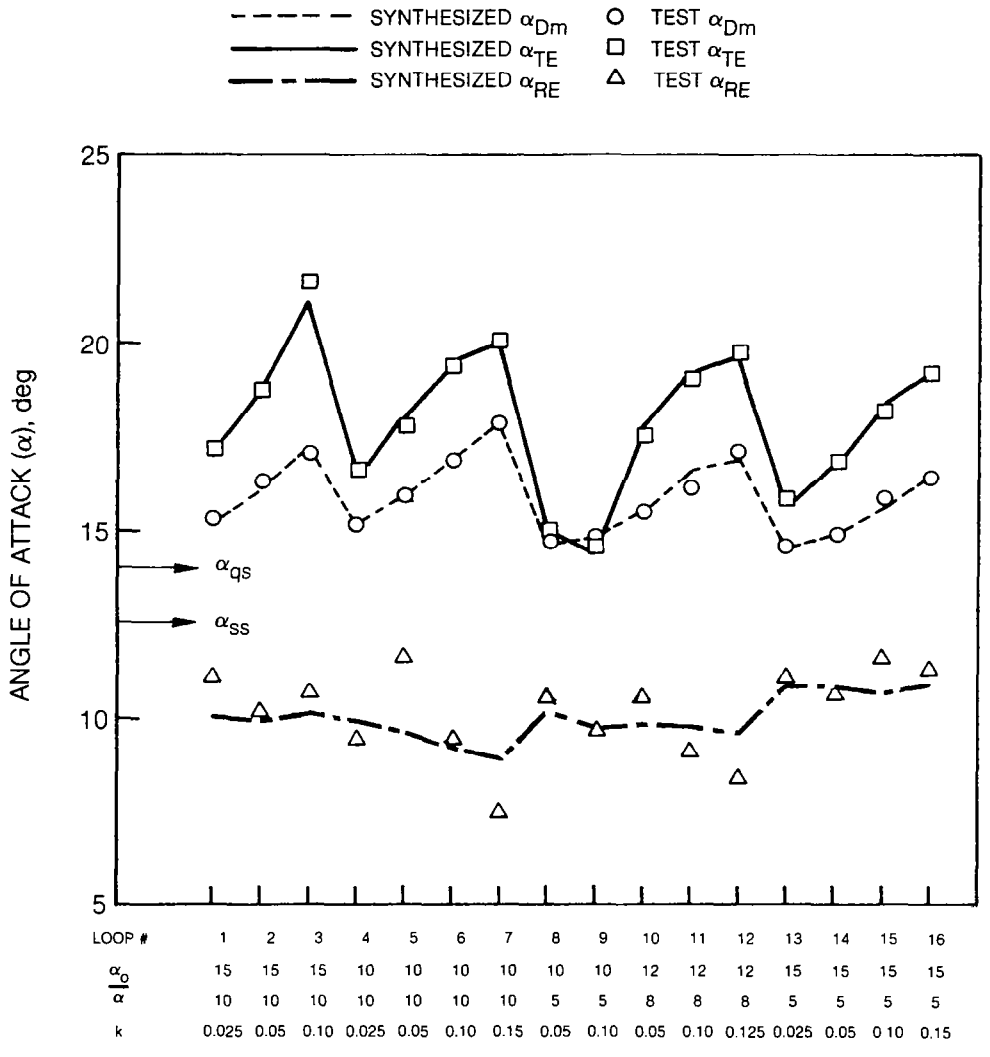

Figure 7. Comparison of Synthesized Stall Events with Test Data, SC 1095 Airfoil, M = 0.3, Data Set No. 1 in Table I

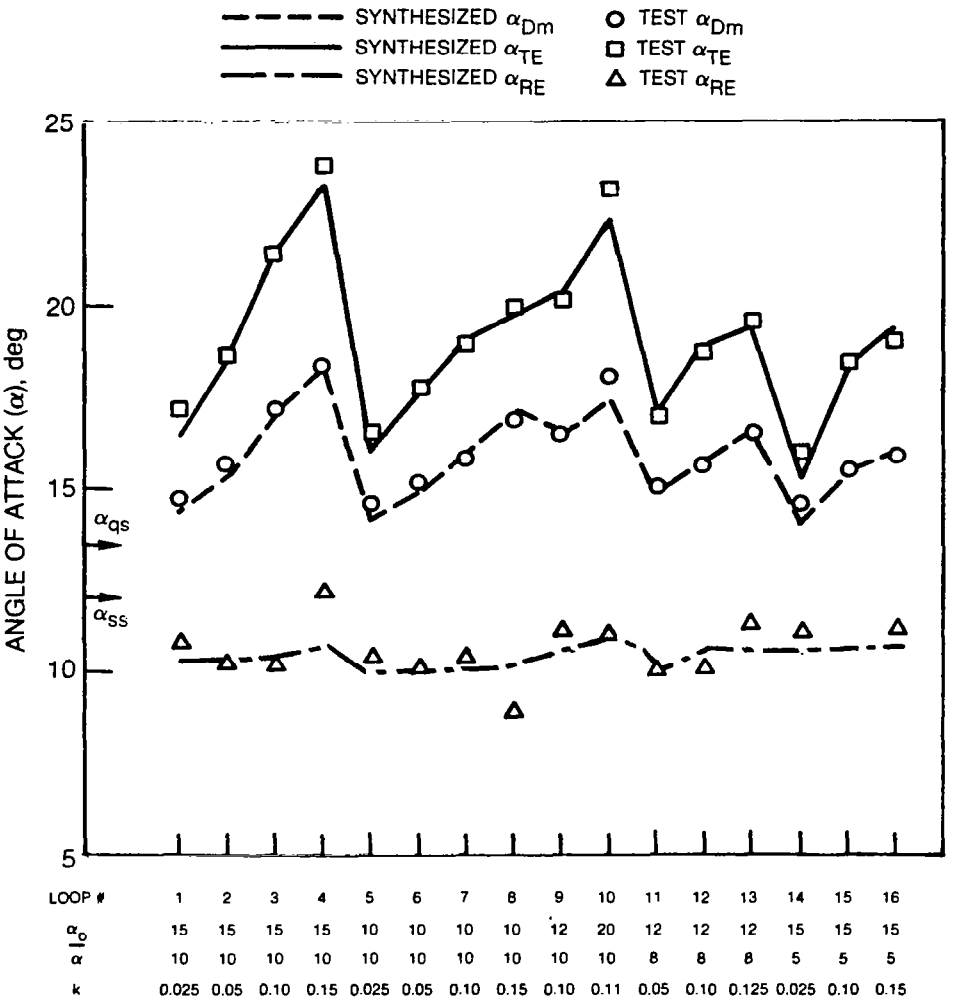

Figure 8. Comparison of Synthesized Stall Events with Test Data, NACA 0012 Airfoil, M = 0.3, Data Set No. 2 in Table I

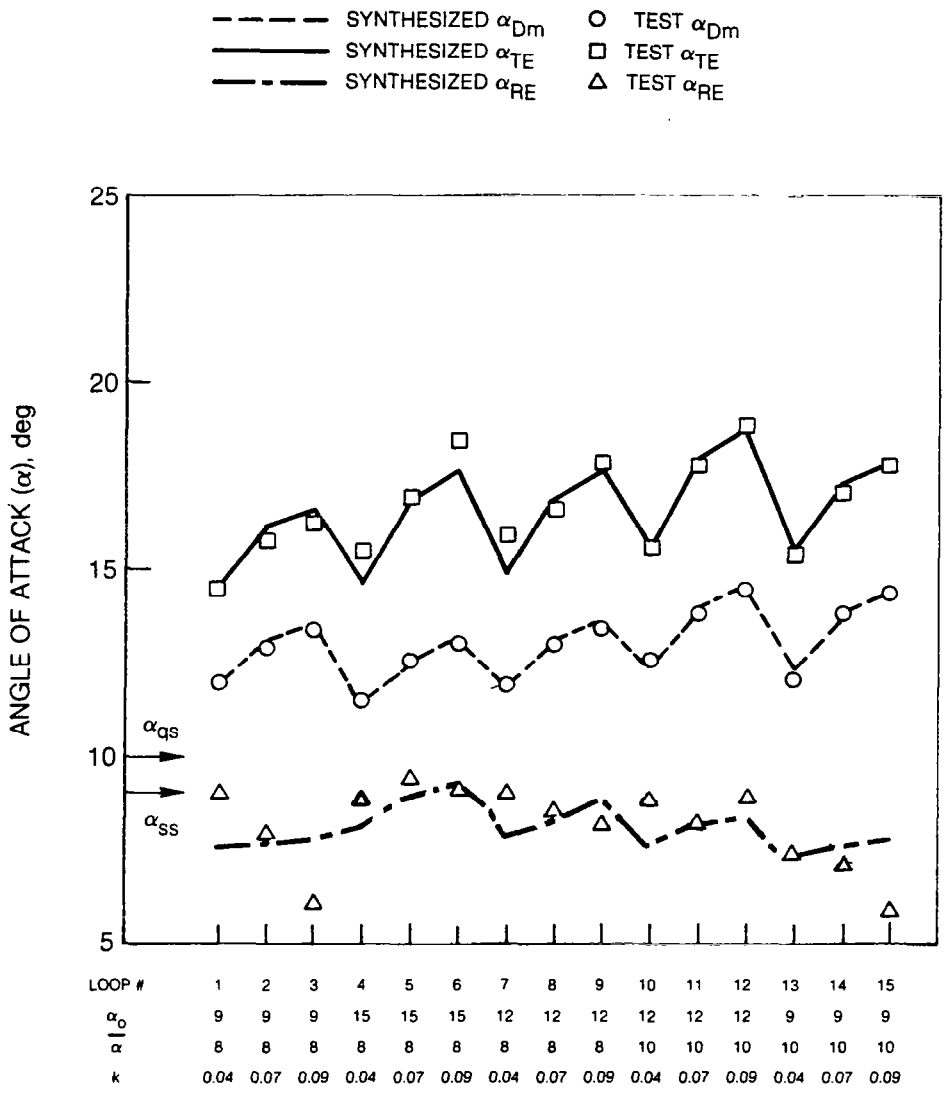

Figure 9. Comparison of Synthesized Stall Events with Test Data, NACA 0012 Airfoil, M = 0.4, Data Set No. 13 in Table I

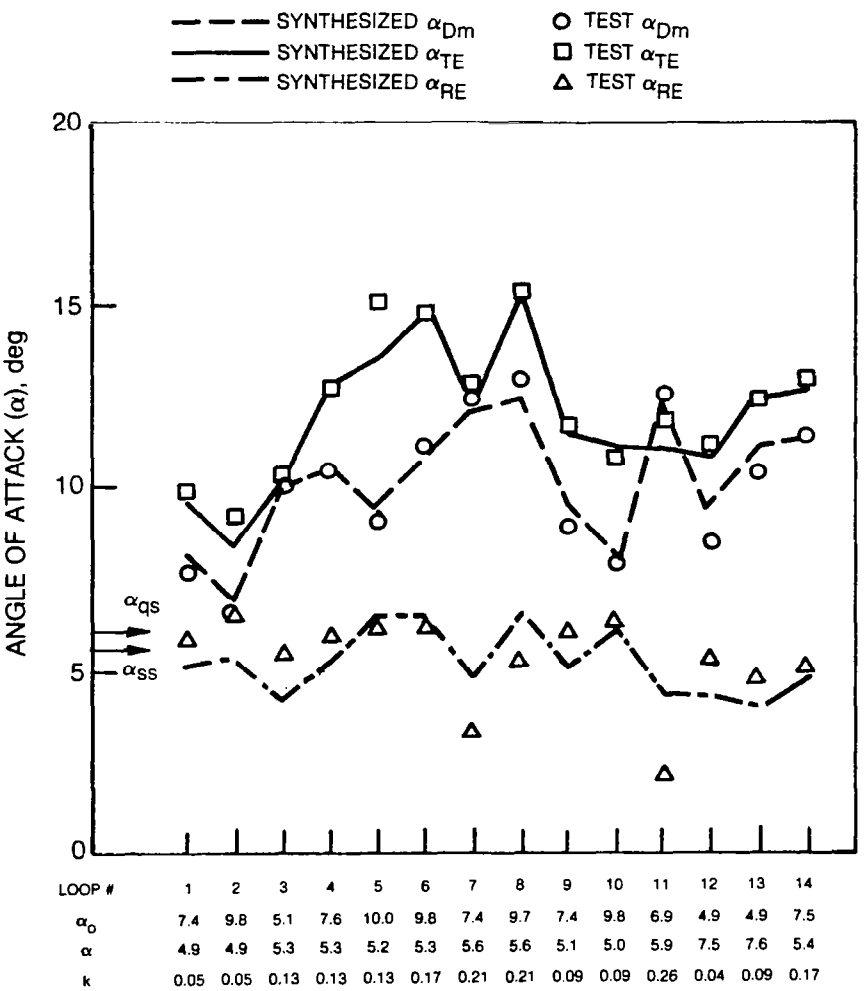

Figure 10. Comparison of Synthesized Stall Events with Test Data, Vertol 0012 Airfoil, M = 0.6, Data Set No. 9 in Table I

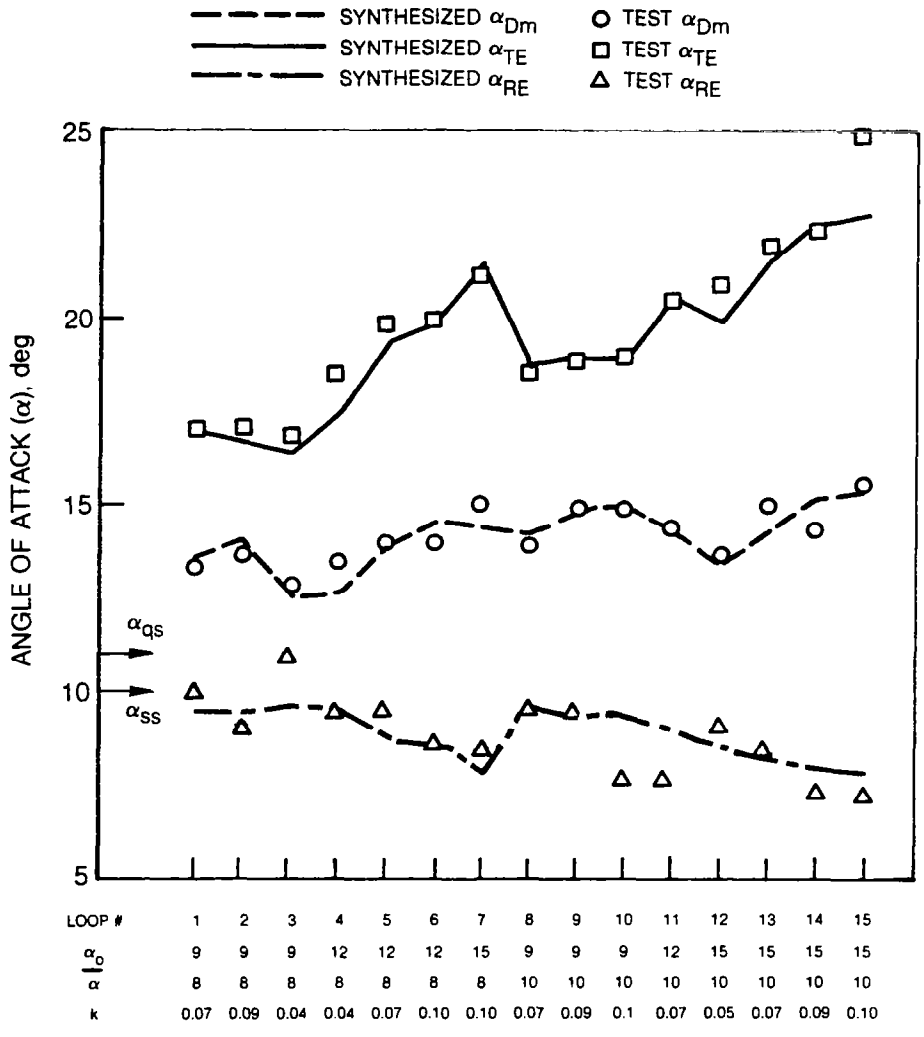

Figure 11. Comparison of Synthesized Stall Events with Test Data, NACA 0012 Yawed, Sweep of 30 deg, M = 0.4, Data Set No. 15 in Table I

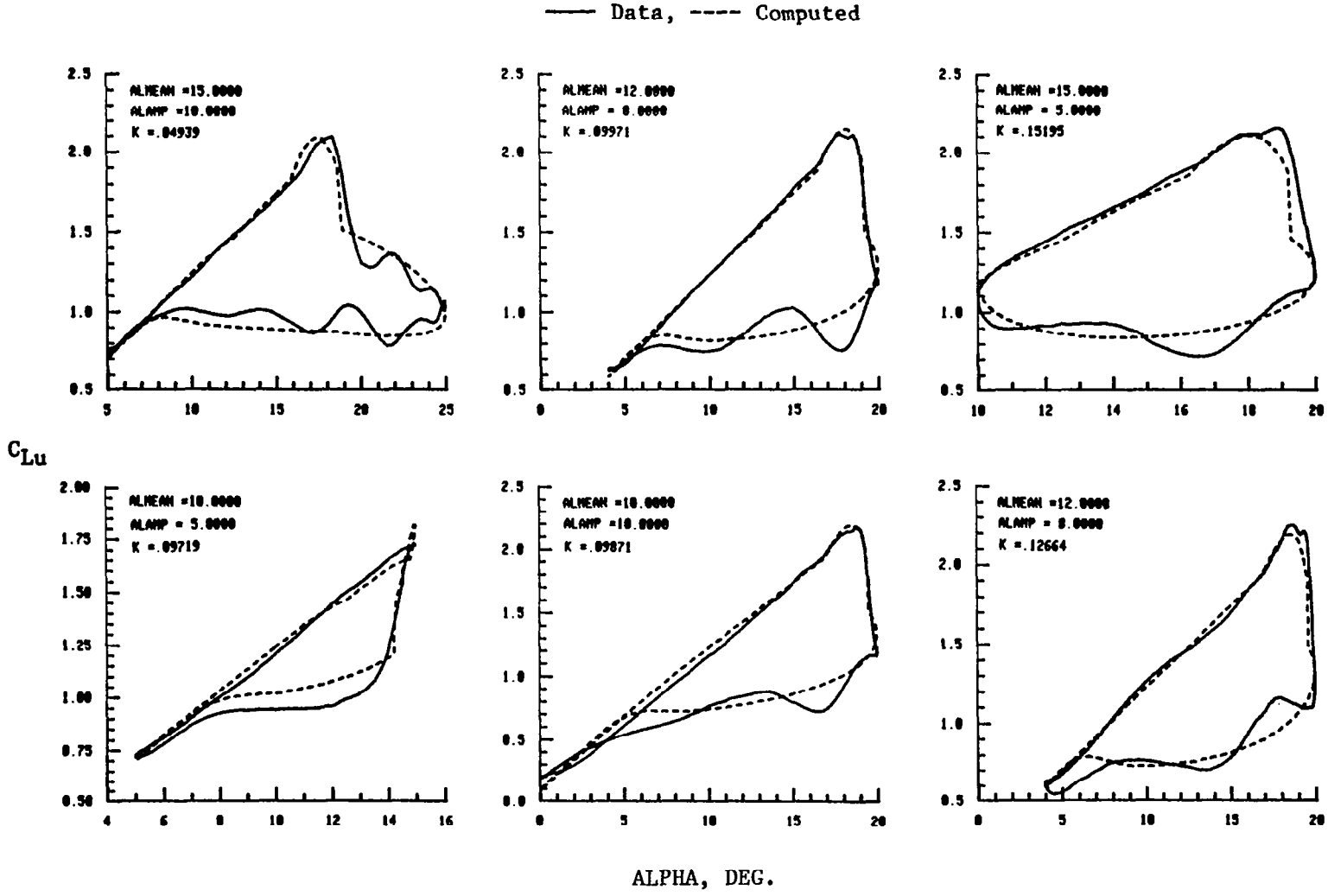

Figure 12a. Comparison of Synthesized Lift Coefficient Loops with Test Data

SC 1095 Airfoil, M = 0.30, R_n = 3.8 x 10^6, Λ = 0.0 deg

Data Set No. 1 in Table I

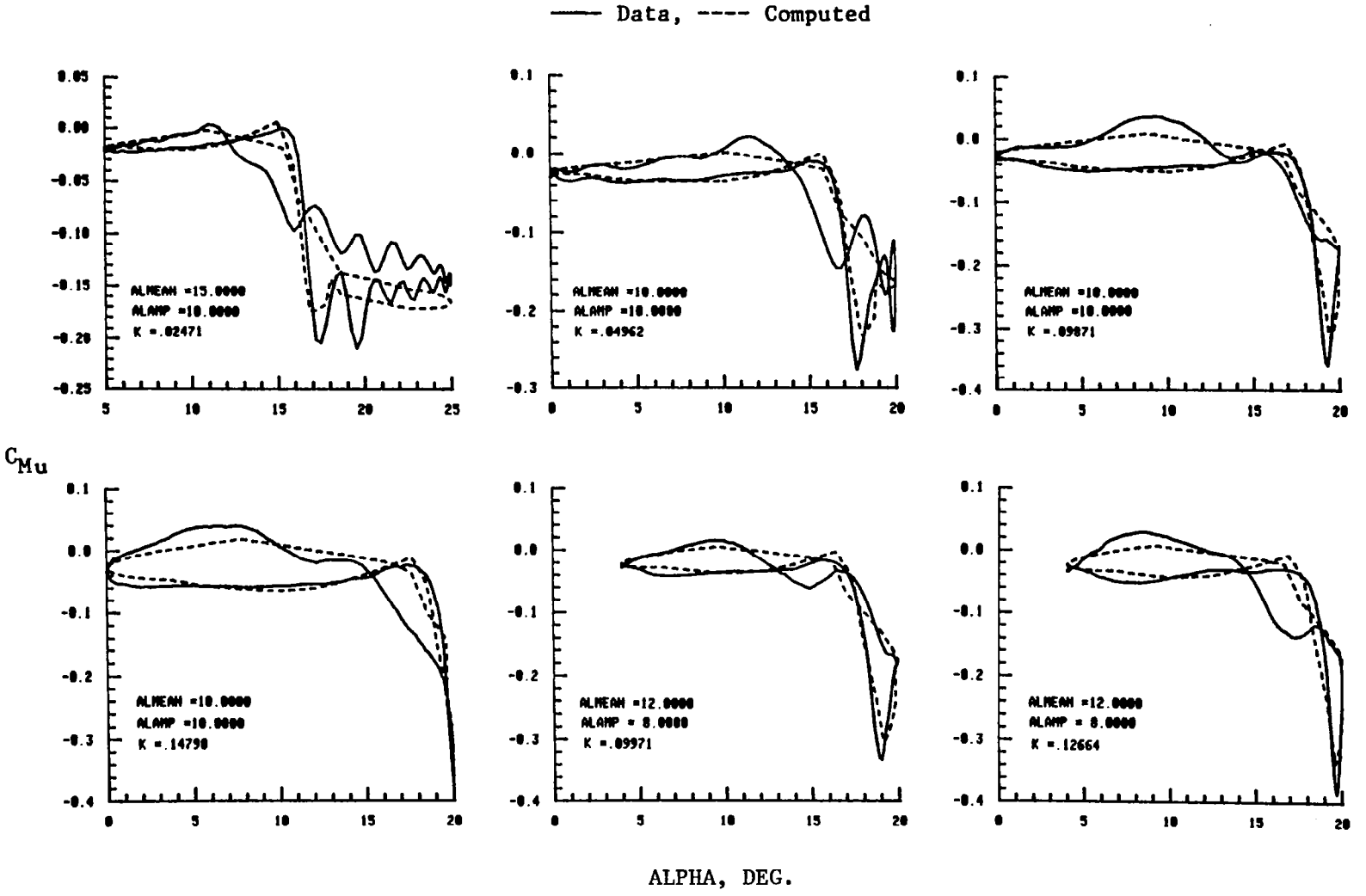

Figure 12b. Comparison Of Synthesized Pitching Moment Coefficient Loops with Test Data

SC 1095 Airfoil, M = 0.30, R_n = 3.8 x 10^6, Λ = 0.0 deg

Data Set No. 1 in Table I

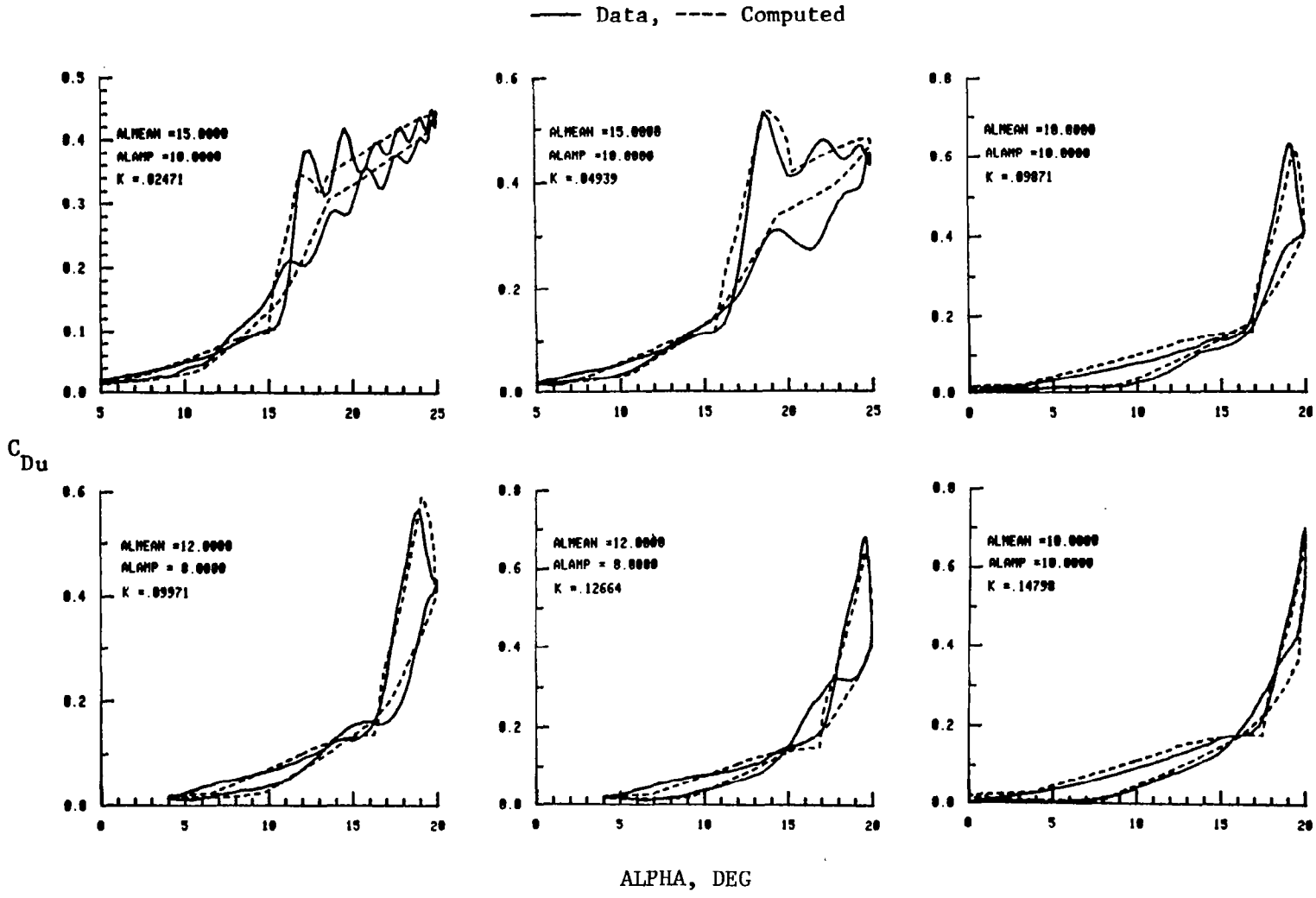

Figure 12c. Comparison Of Synthesized Drag Coefficient Loops with Test Data

SC 1095 Airfoil, M = 0.30, R_n = 3.8 x 10^6, Λ = 0.0 deg

Data Set No. 1 in Table I

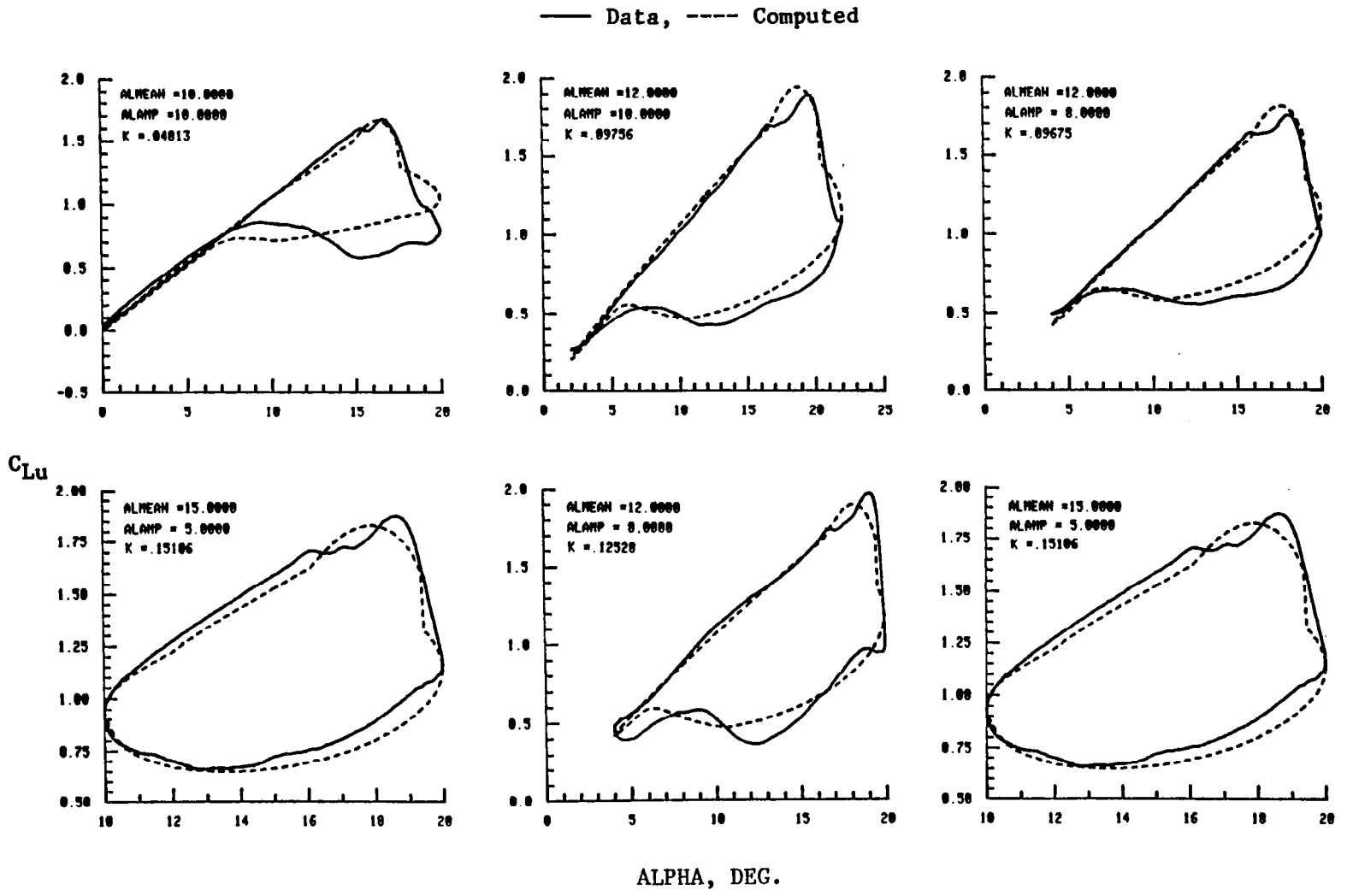

Figure 13a. Comparison of Synthesized Lift Coefficient Loops with Test Data

NACA 0012 Airfoil, M = 0.30, R_n = 3.8 x 10^6, Λ = 0.0 deg

Data Set No. 2 in Table I

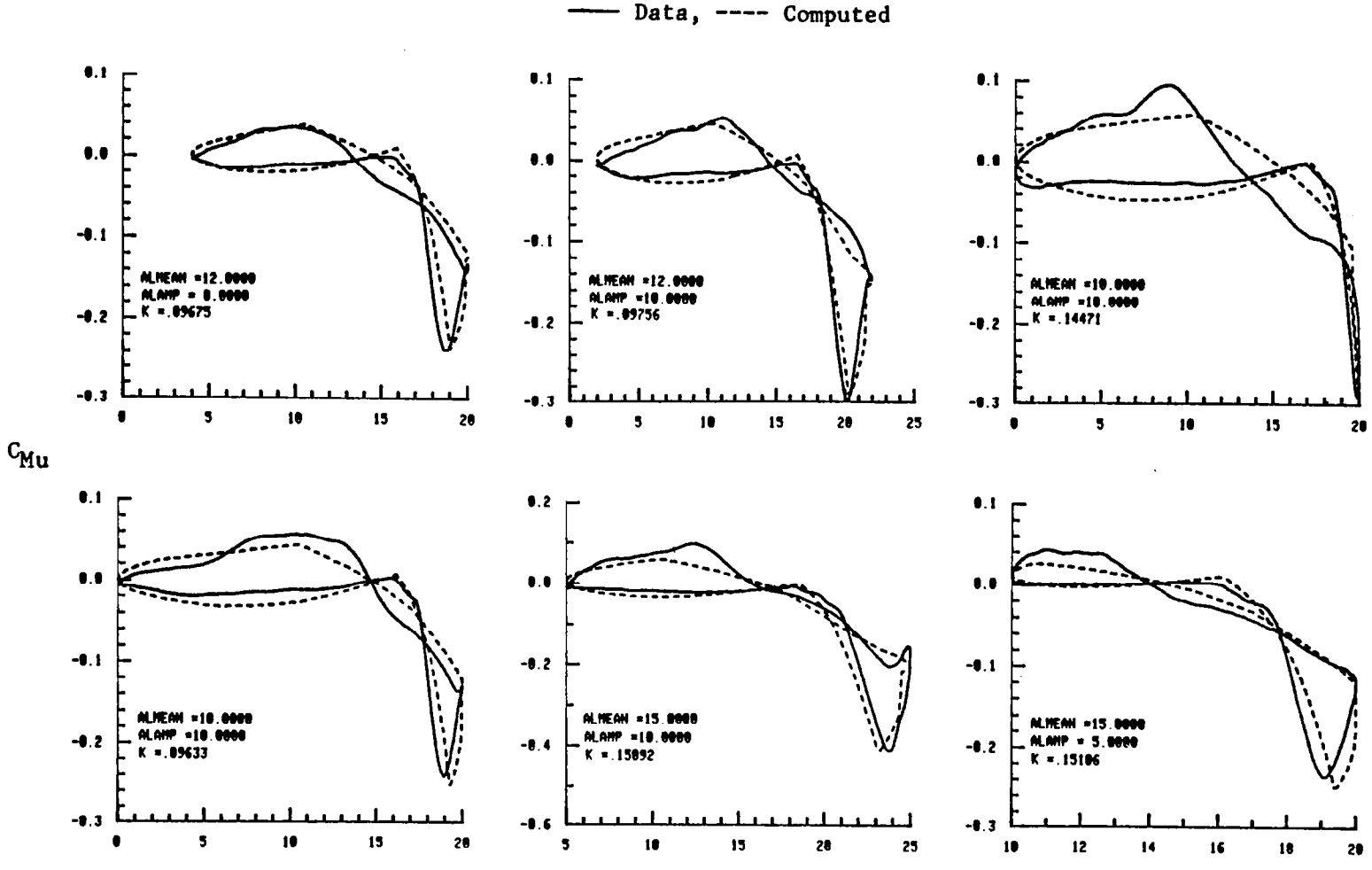

Figure 13b. Comparison Of Synthesized Pitching Moment Coefficient Loops with Test Data
NACA 0012 Airfoil, M = 0.30, R_n = 3.8 x 10^6, Λ = 0.0 deg
Data Set No. 2 in Table I

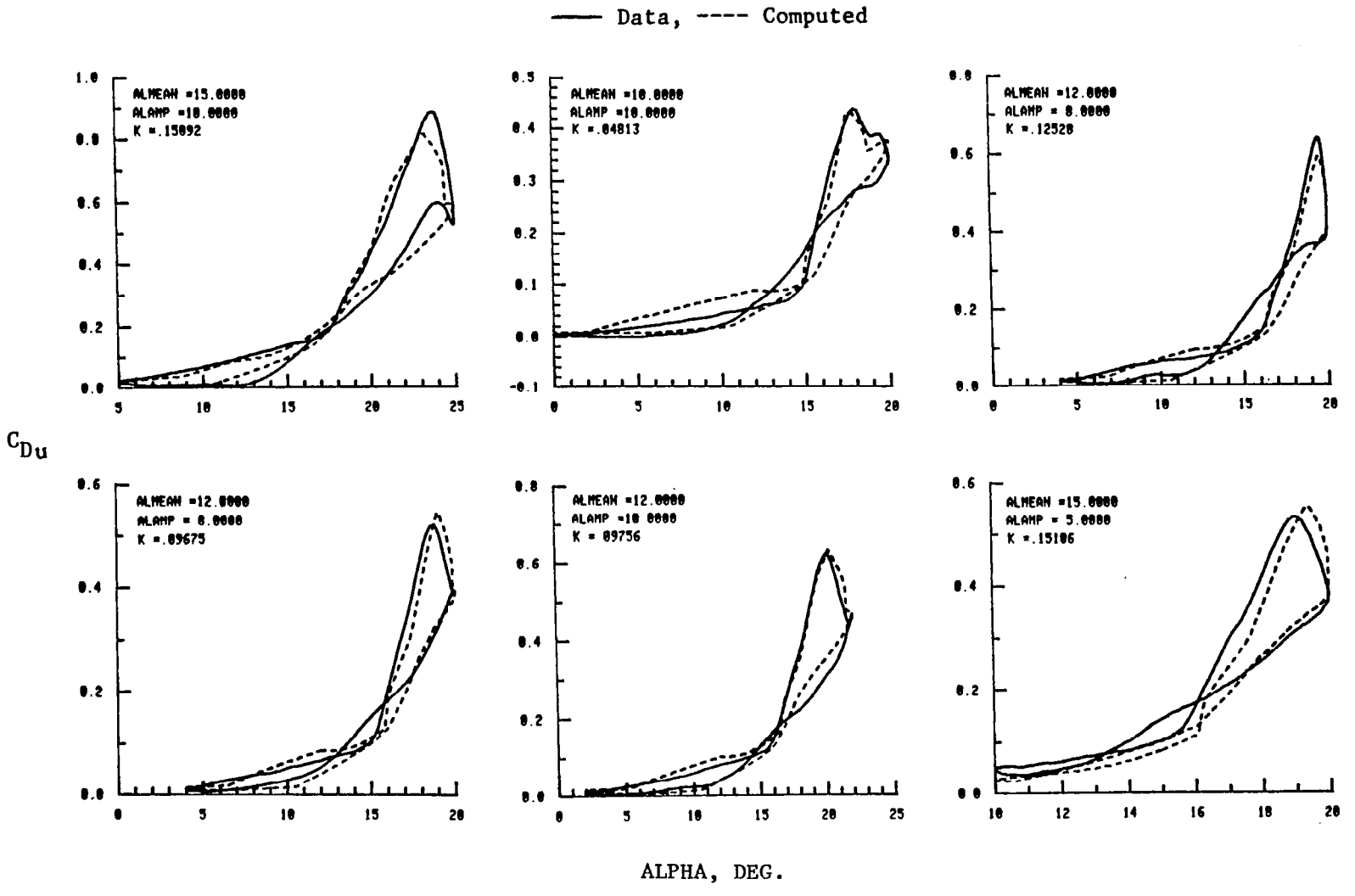

Figure 13c. Comparison Of Synthesized Drag Coefficient Loops with Test Data

NACA 0012 Airfoil, M = 0.30, R_n = 3.8 x 10^6, Λ = 0.0 deg

Data Set No. 2 in Table I

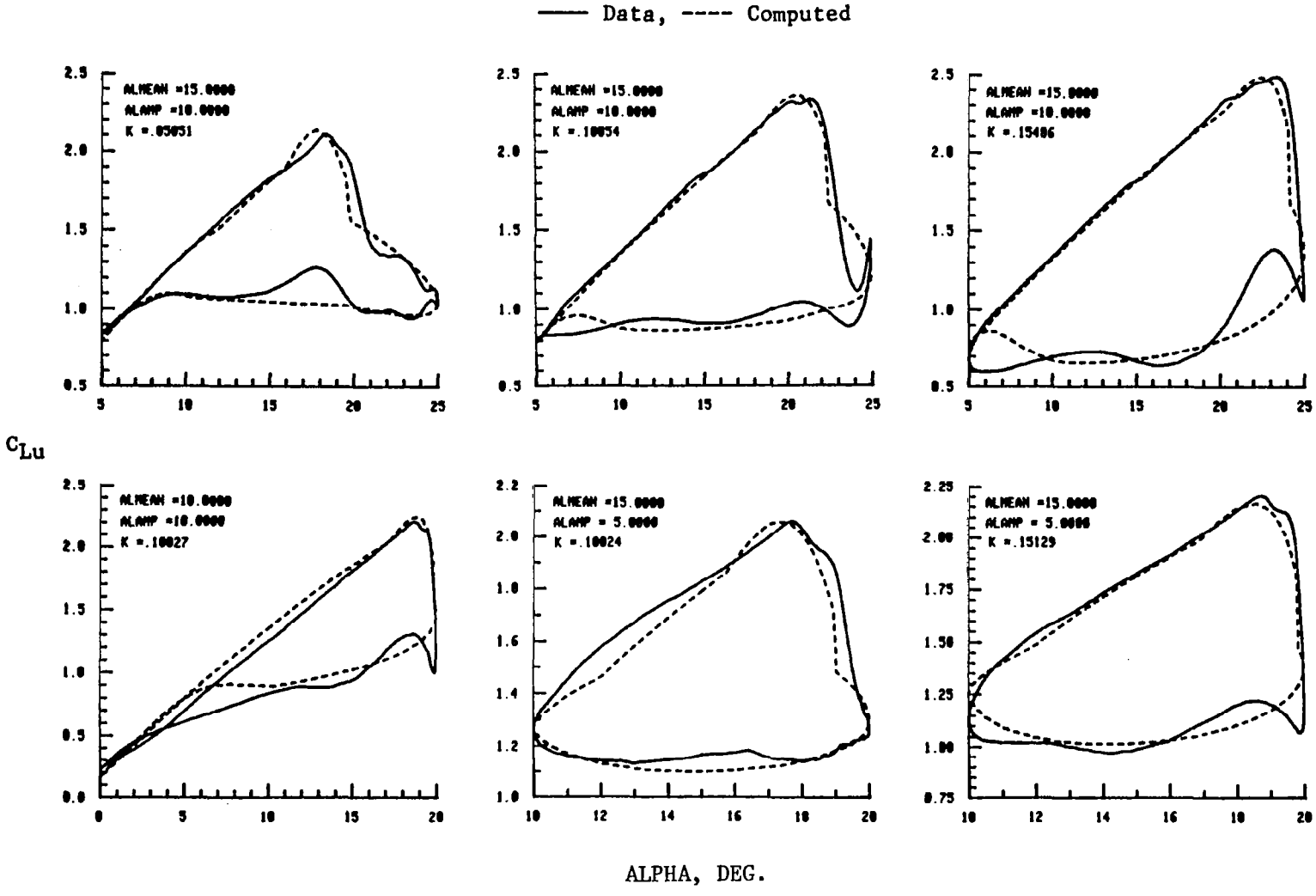

Figure 14a. Comparison of Synthesized Lift Coefficient Loops with Test Data

VR-7 Airfoil, M = 0.30, R_n = 3.8 x 10^6, Λ = 0.0 deg

Data Set No. 3 in Table I

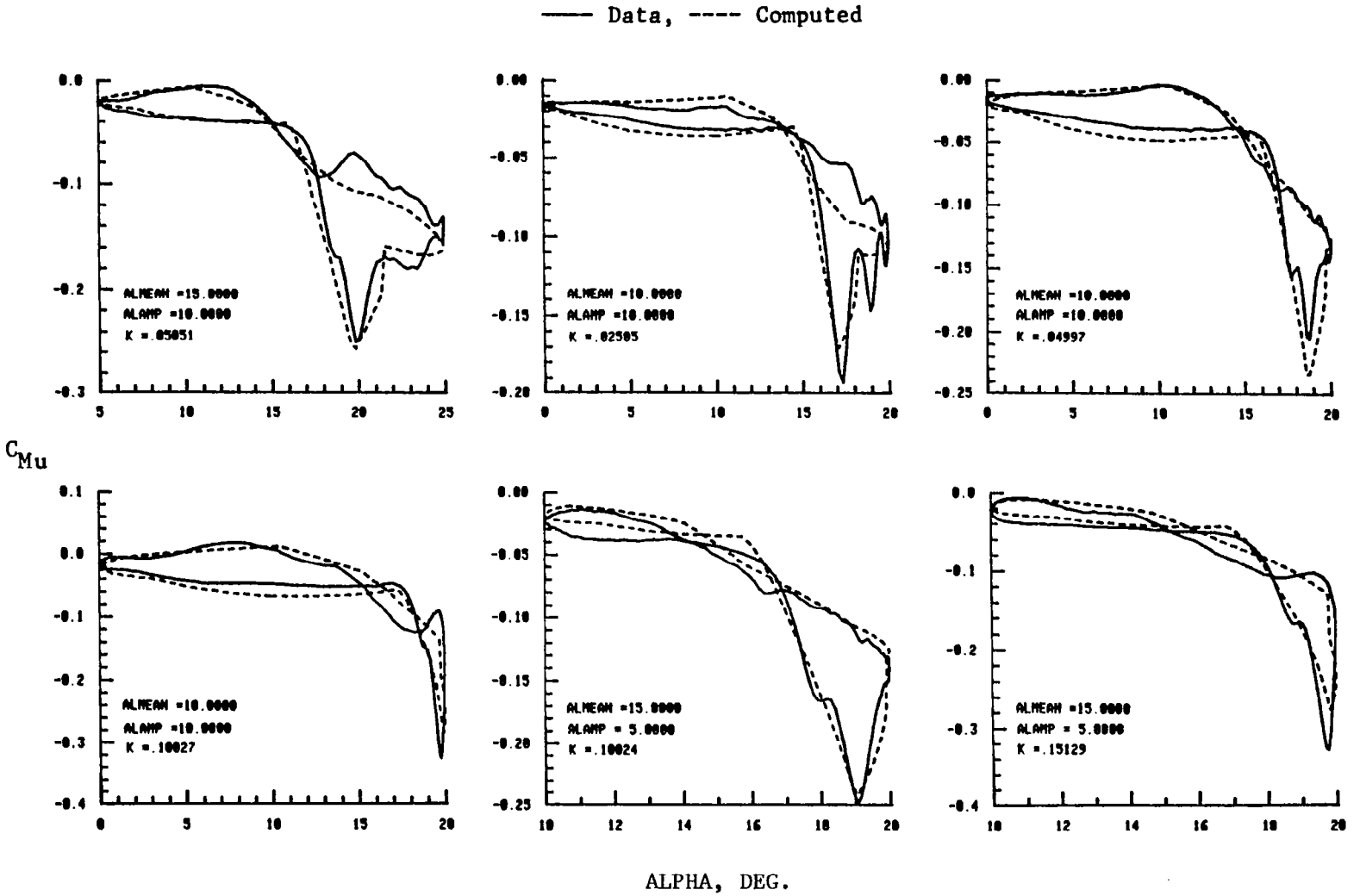

Figure 14b. Comparison Of Synthesized Pitching Moment Coefficient Loops with Test Data

VR-7 Airfoil, M = 0.30, R_n = 3.8 x 10^6, Λ = 0.0 deg

Data Set No. 3 in Table I

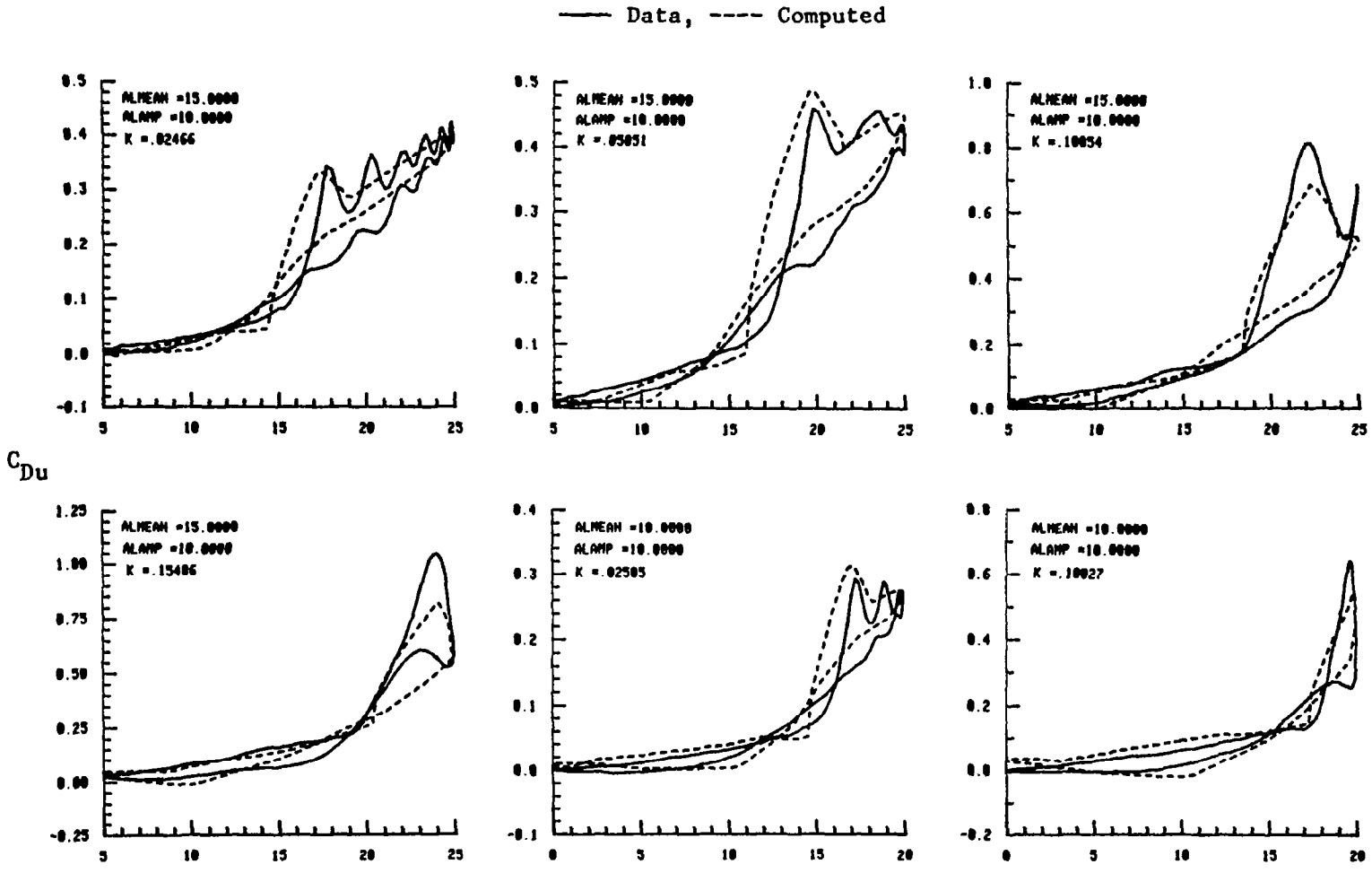

Figure 14c. Comparison Of Synthesized Drag Coefficient Loops with Test Data

VR-7 Airfoil, M = 0.30, R_n = 3.8 x 10^6, Λ = 0.0 deg

Data Set No. 3 in Table I

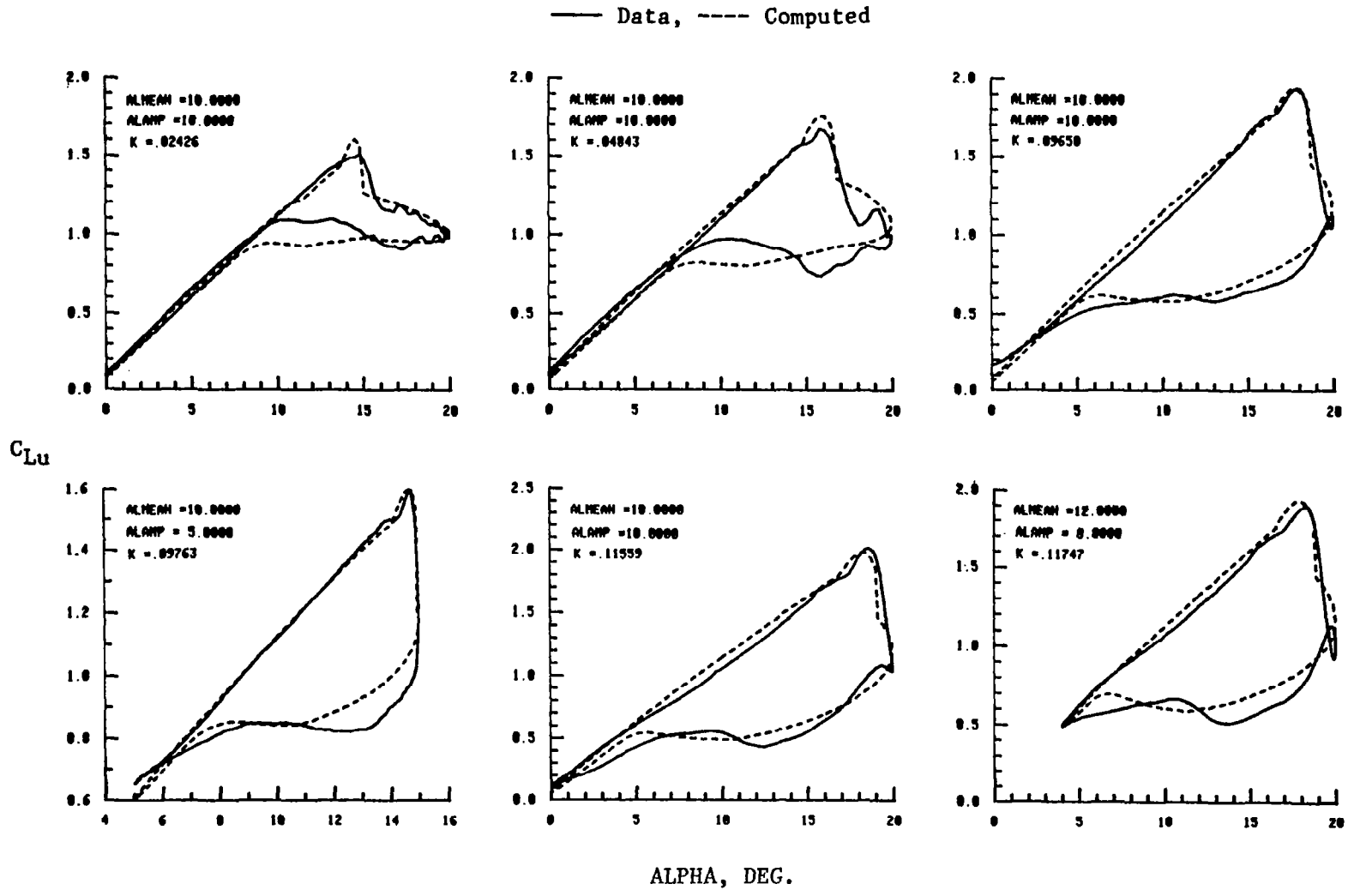

Figure 15a. Comparison of Synthesized Lift Coefficient Loops with Test Data

NLR-1 Airfoil, M = 0.30, R_n = 3.8 x 10^6, Λ = 0.0 deg

Data Set No. 4 in Table I

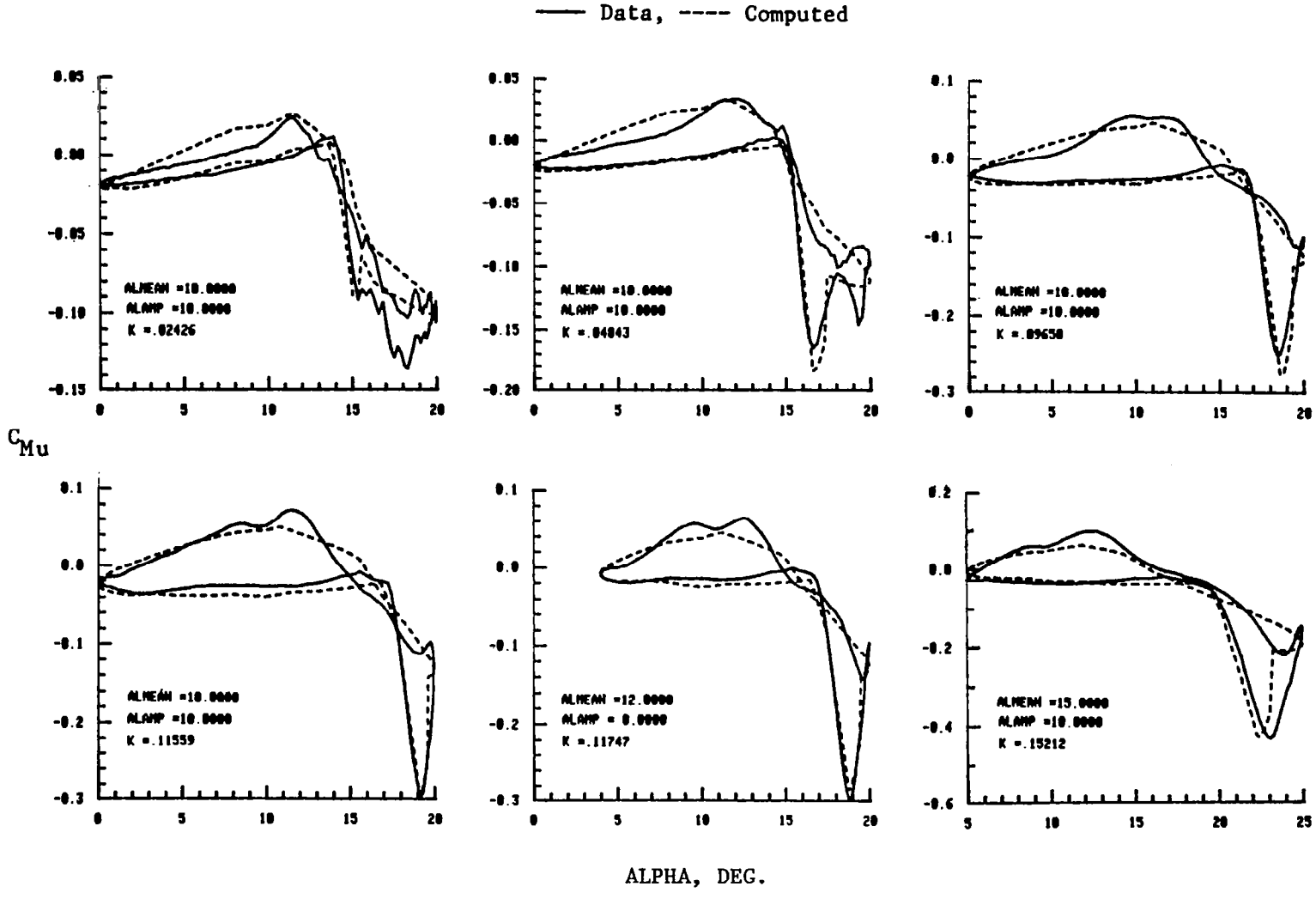

Figure 15b. Comparison Of Synthesized Pitching Moment Coefficient Loops with Test Data

NLR-1 Airfoil, M = 0.30, R_n = 3.8 x 10^6, Λ = 0.0 deg

Data Set No. 4 in Table I

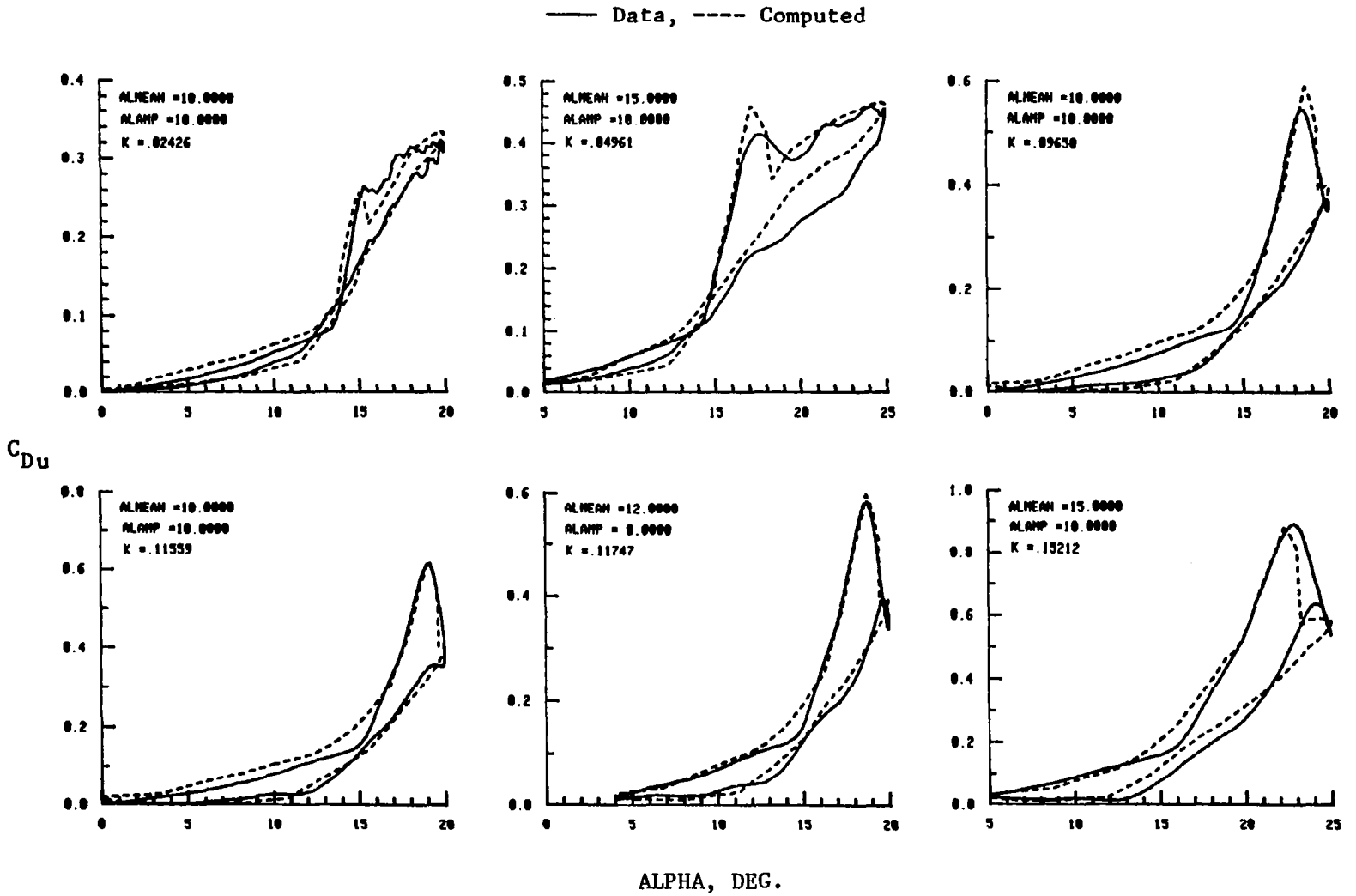

Figure 15c. Comparison Of Synthesized Drag Coefficient Loops with Test Data

NLR-1 Airfoil, M = 0.30, R_n = 3.8 x 10^6, Λ = 0.0 deg

Data Set No. 4 in Table I

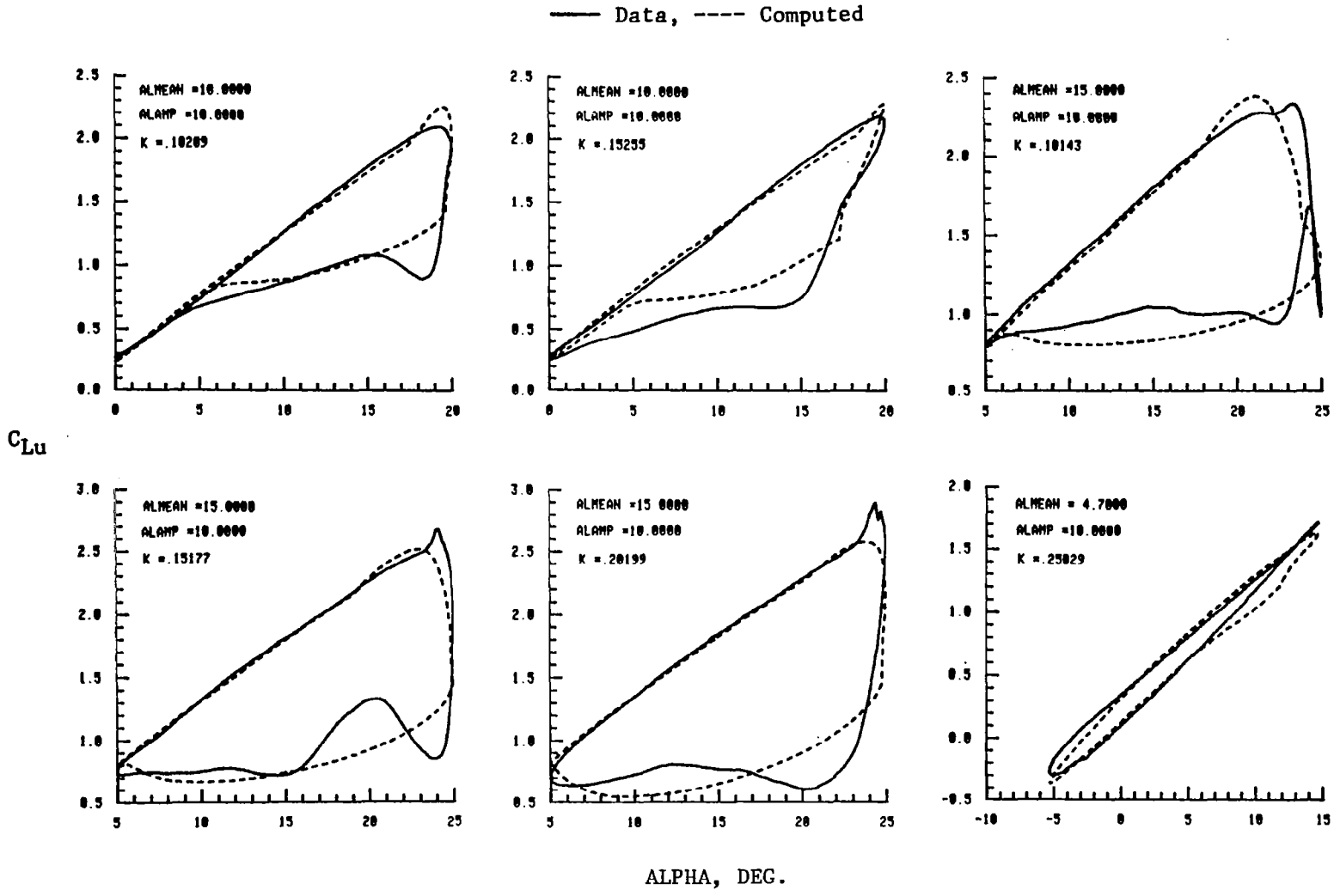

Figure 16a. Comparison of Synthesized Lift Coefficient Loops with Test Data

VR-7 Airfoil, M = 0.18, R_n = 2.5 x 10^6, Λ = 0.0 deg

Data Set No. 5 in Table I

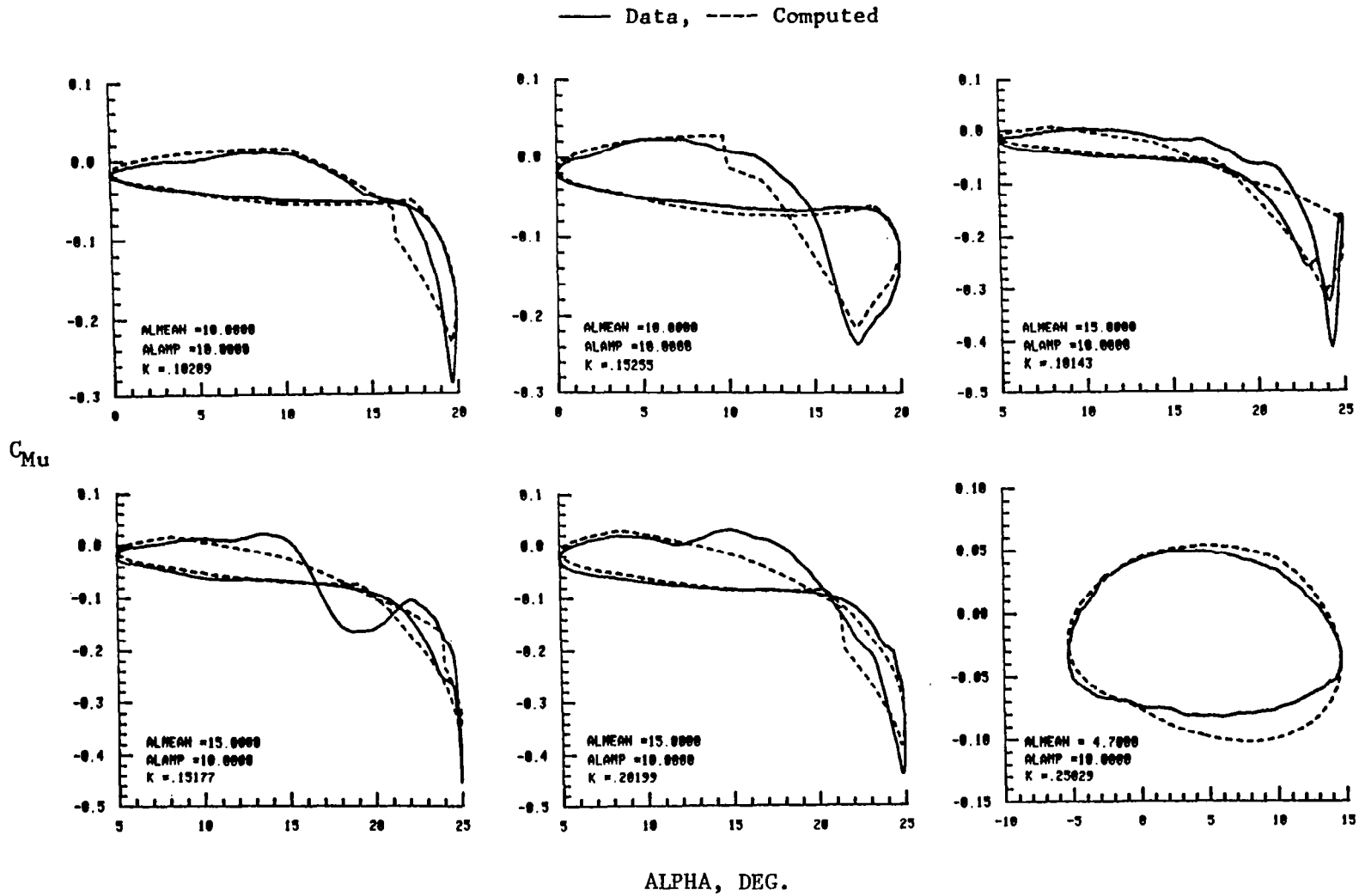

Figure 16b. Comparison Of Synthesized Pitching Moment Coefficient Loops with Test Data

VR-7 Airfoil, M = 0.18, R_n = 2.5 x 10^6, Λ = 0.0 deg

Data Set No. 5 in Table I

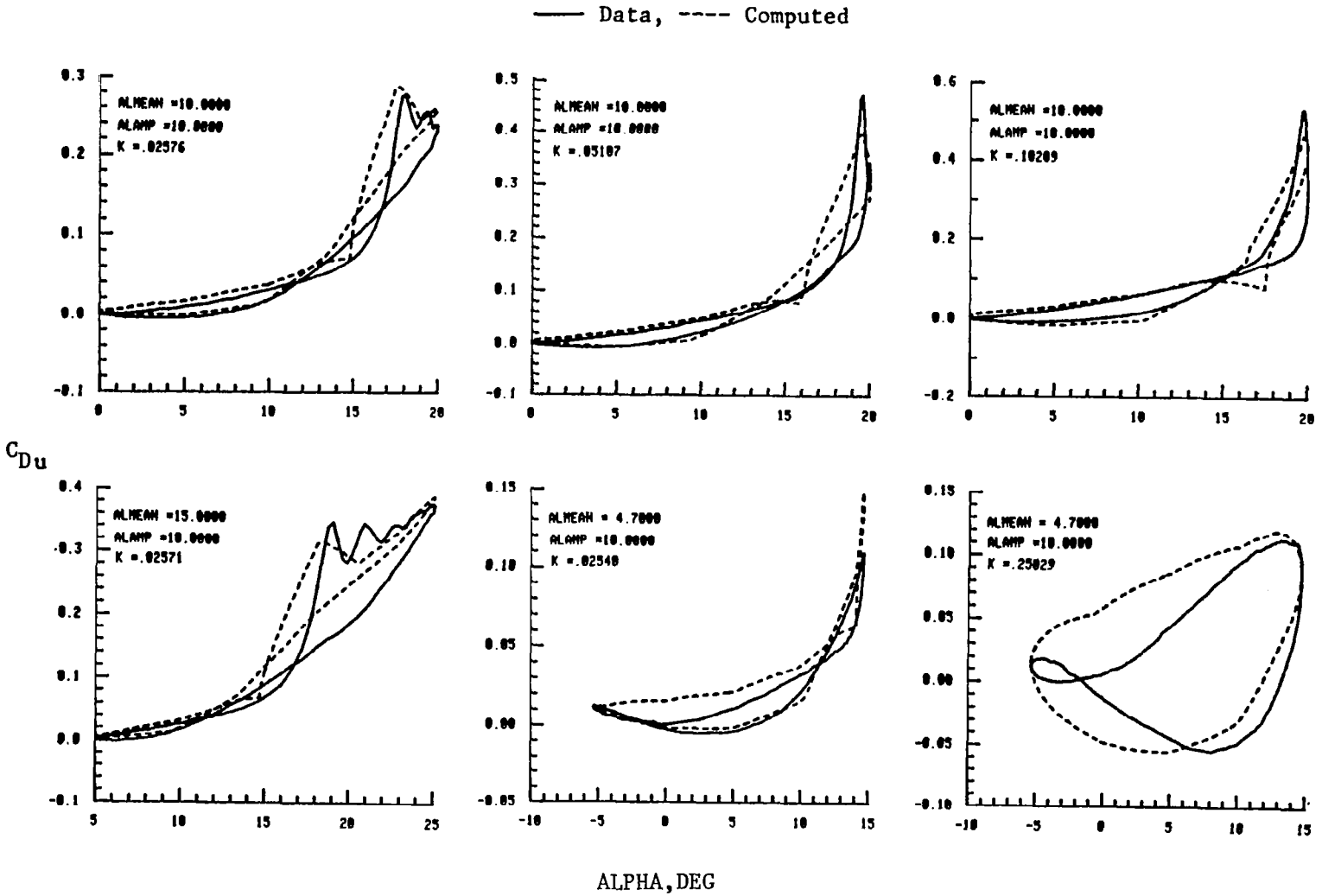

Figure 16c. Comparison Of Synthesized Drag Coefficient Loops with Test Data

VR-7 Airfoil, M = 0.18, R_n = 2.5 x 10^6, Λ = 0.0 deg

Data Set No. 5 in Table I

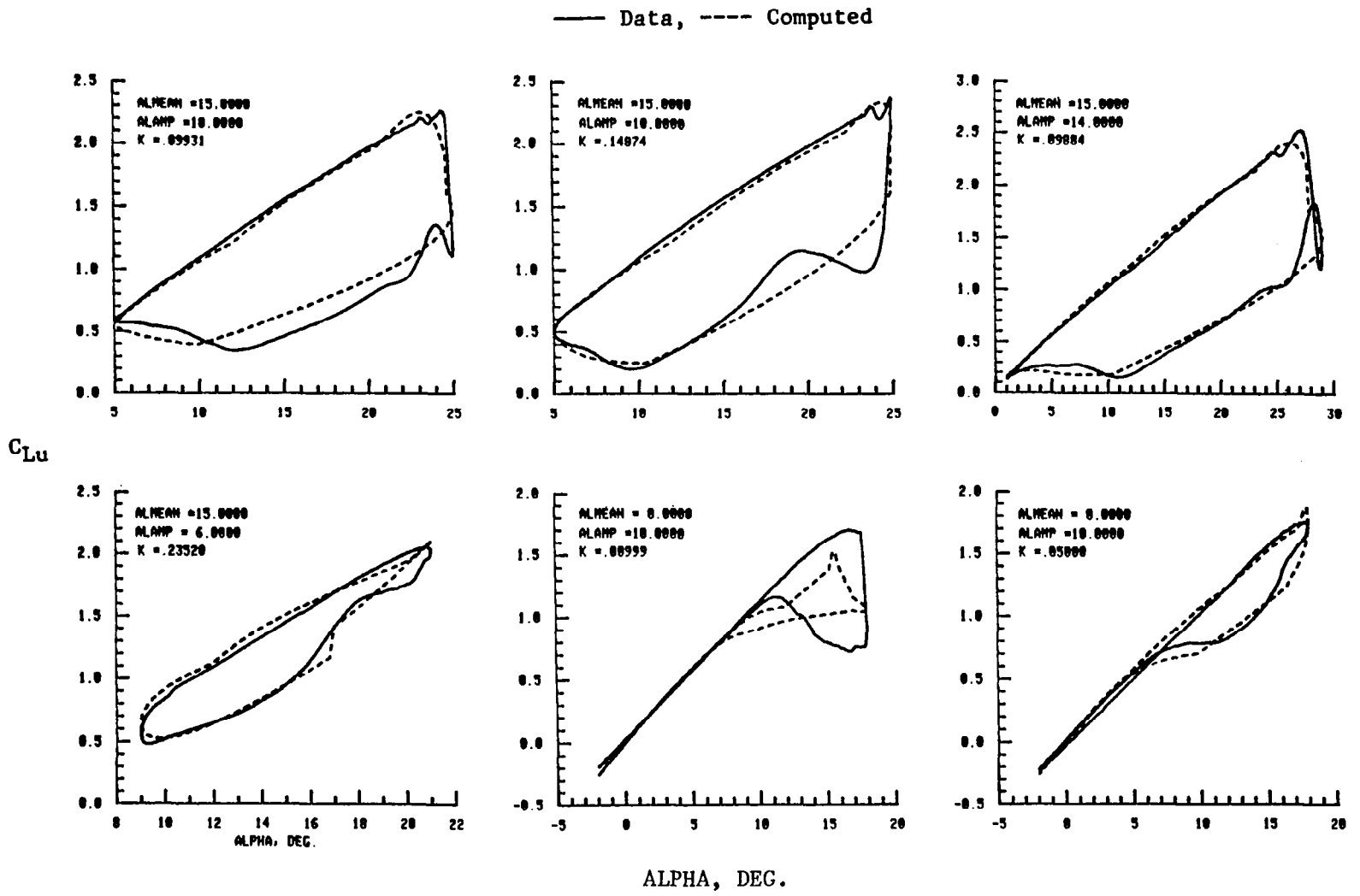

Figure 17a. Comparison of Synthesized Lift Coefficient Loops with Test Data

NACA 0012 Airfoil, M = 0.18, R_n = 2.5 x 10^6, Λ = 0.0 deg

Data Set No. 6 in Table I

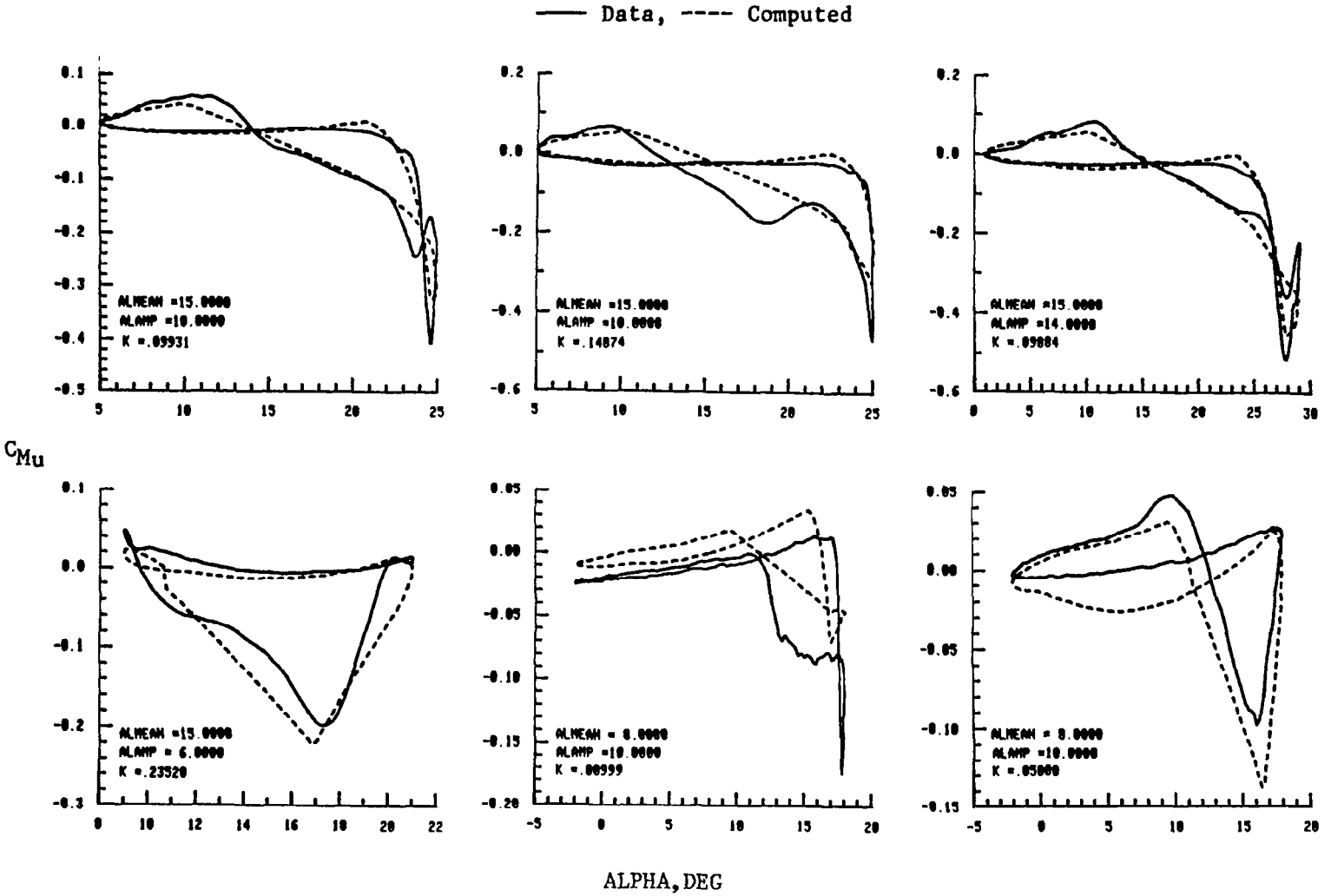

Figure 17b. Comparison Of Synthesized Pitching Moment Coefficient Loops with Test Data

NACA 0012 Airfoil, M = 0.18, R_n = 2.5 x 10^6, Λ = 0.0 deg

Data Set No. 6 in Table I

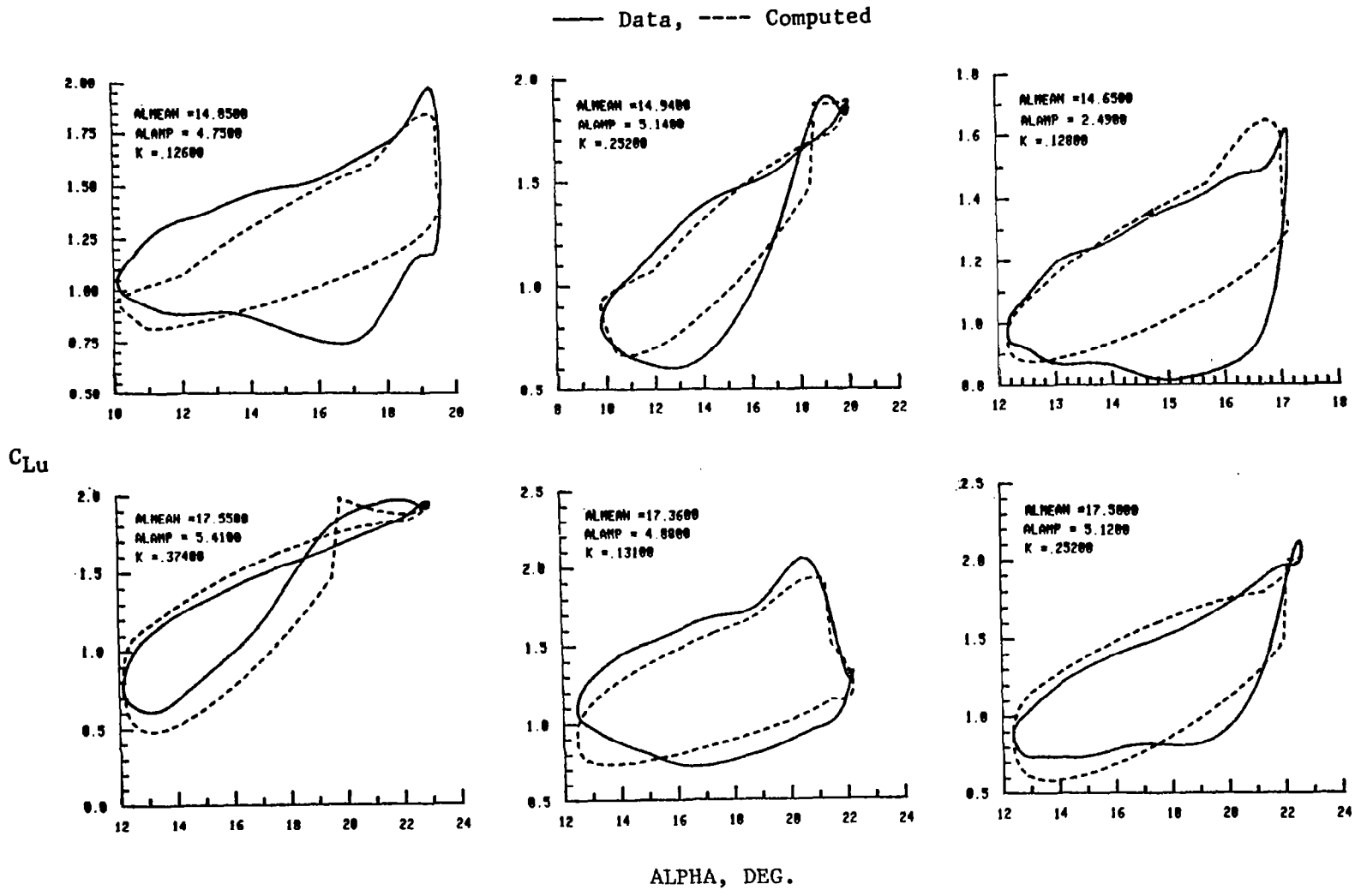

Figure 18a. Comparison of Synthesized Lift Coefficient Loops with Test Data
Vertol 0012 Airfoil, M = 0.20, R_n = 2.6 x 10^6, Λ = 0.0 deg
Data Set No. 7 in Table I

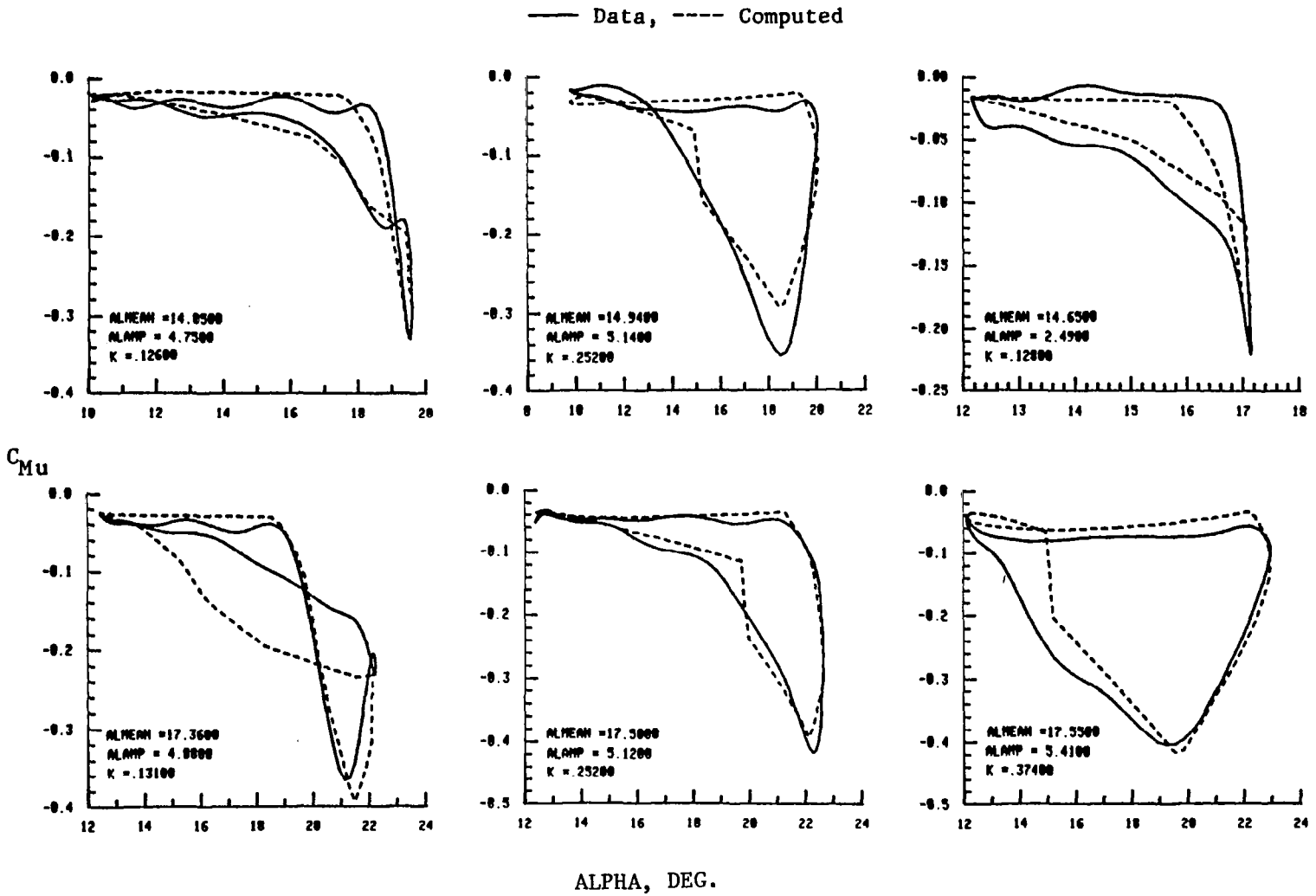

Figure 18b. Comparison Of Synthesized Pitching Moment Coefficient Loops with Test Data

Vertol 0012 Airfoil, M = 0.20, R_n = 2.6 x 10^6, Λ = 0.0 deg

Data Set No. 7 in Table I

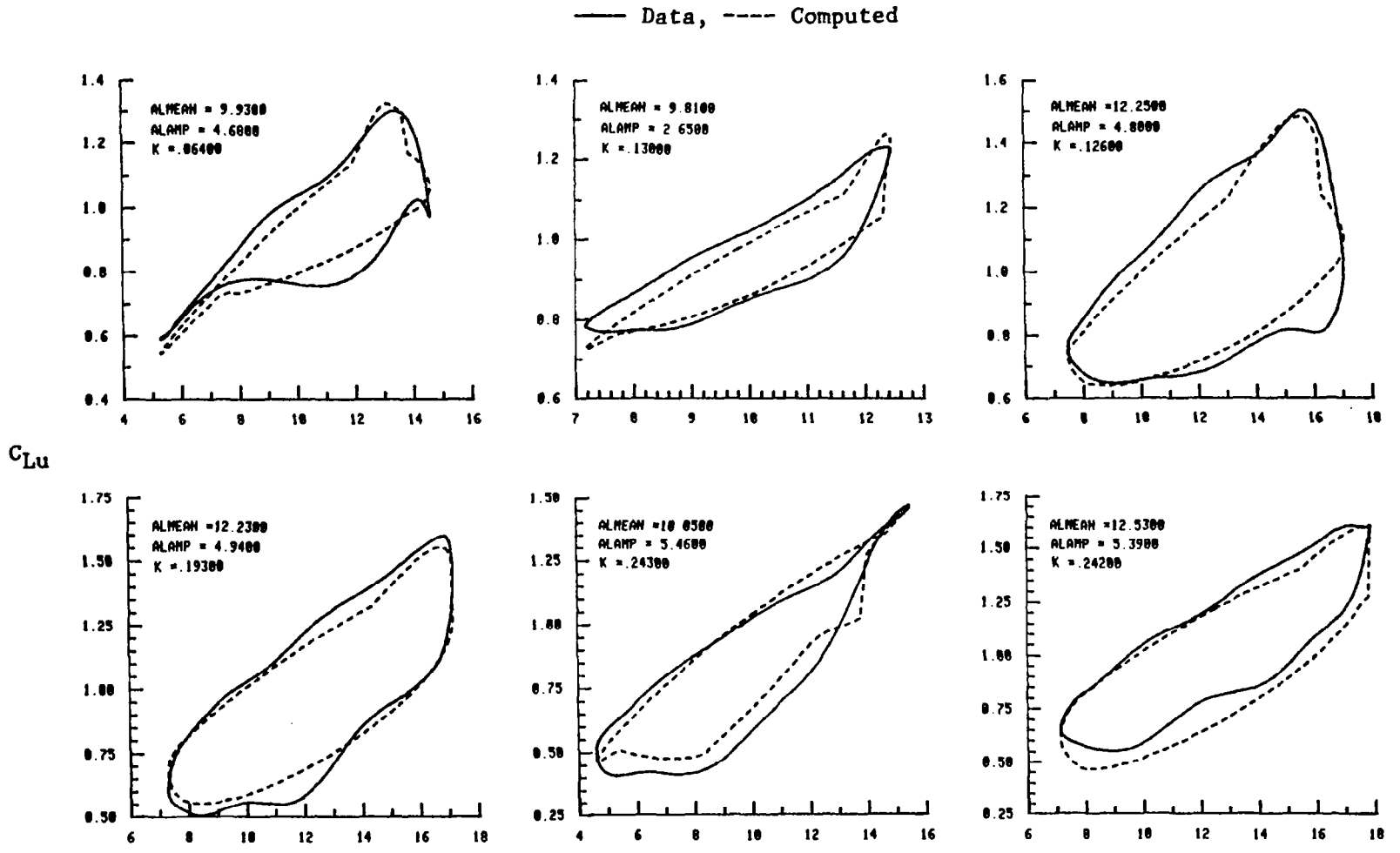

Figure 19a. Comparison of Synthesized Lift Coefficient Loops with Test Data

Vertol 0012 Airfoil, M = 0.40, $R_n = 4.8 \times 10^6$, $\Lambda = 0.0$ deg

Data Set No. 8 in Table I

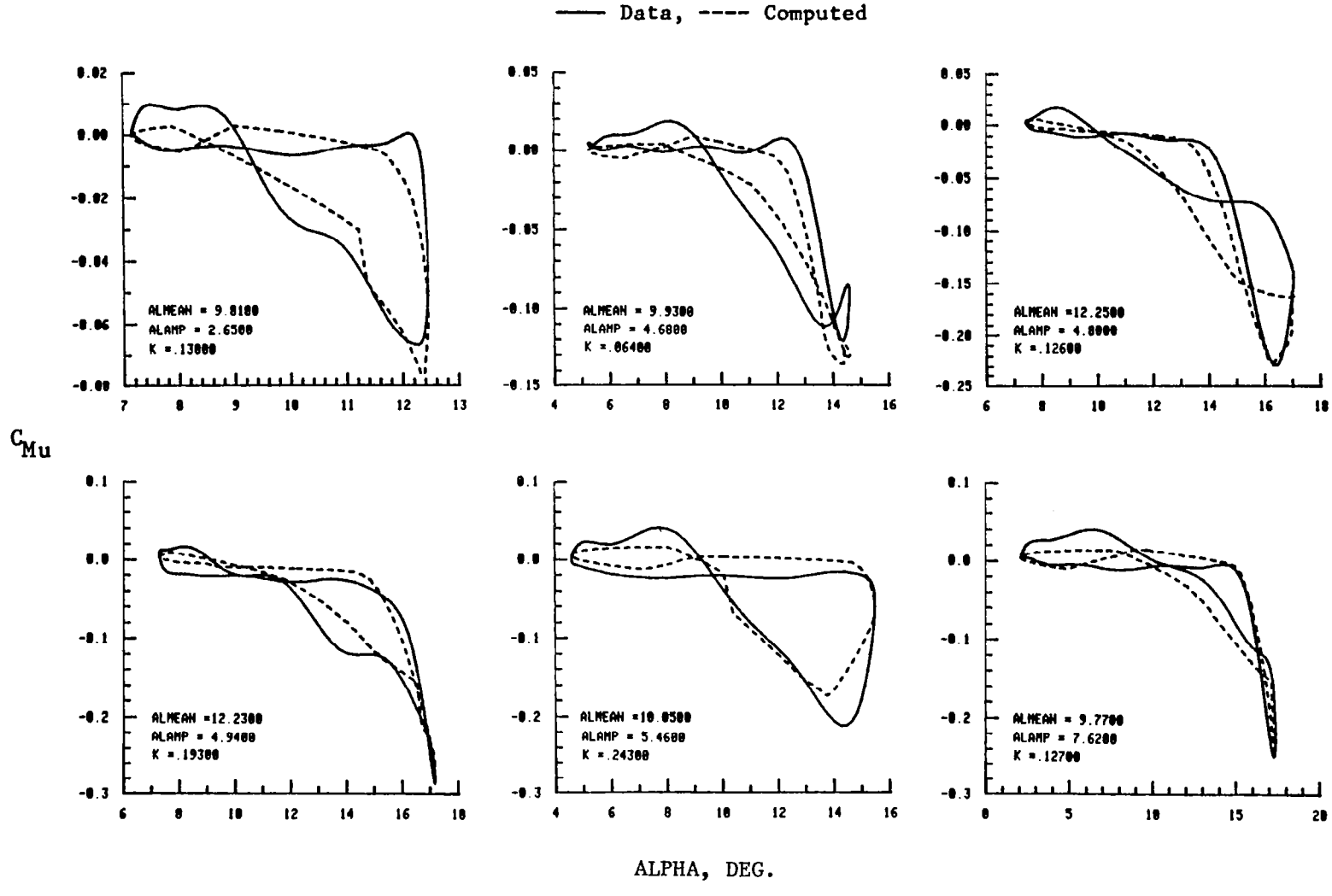

Figure 19b. Comparison Of Synthesized Pitching Moment Coefficient Loops with Test Data

Vertol 0012 Airfoil, M = 0.40, R_n = 4.8 x 10^6, Λ = 0.0 deg

Data Set No. 8 in Table I

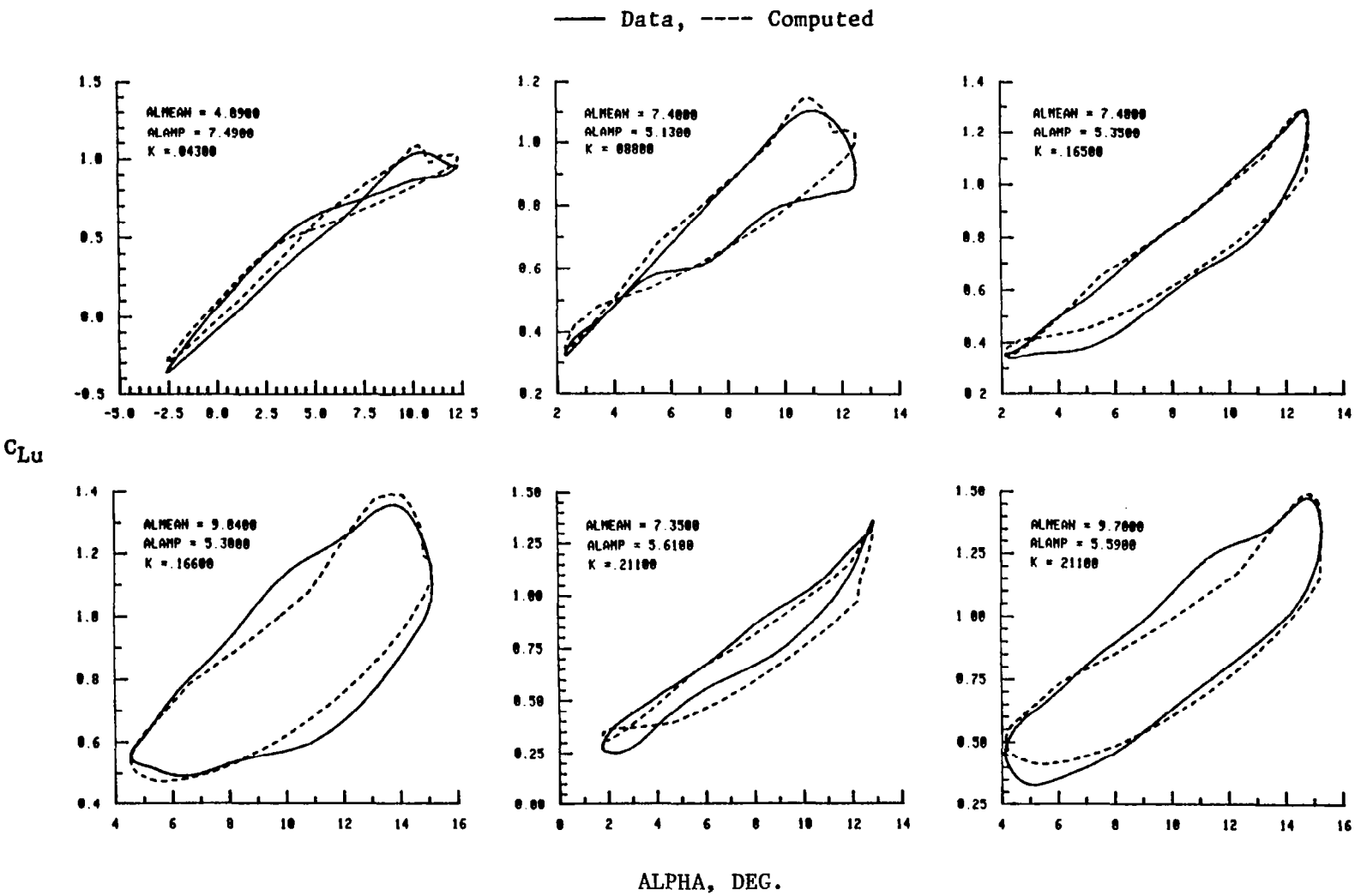

Figure 20a. Comparison of Synthesized Lift Coefficient Loops with Test Data

Vertol 0012 Airfoil, M = 0.60, R_n = 6.2 x 10^6, Λ = 0.0 deg

Data Set No. 9 in Table I

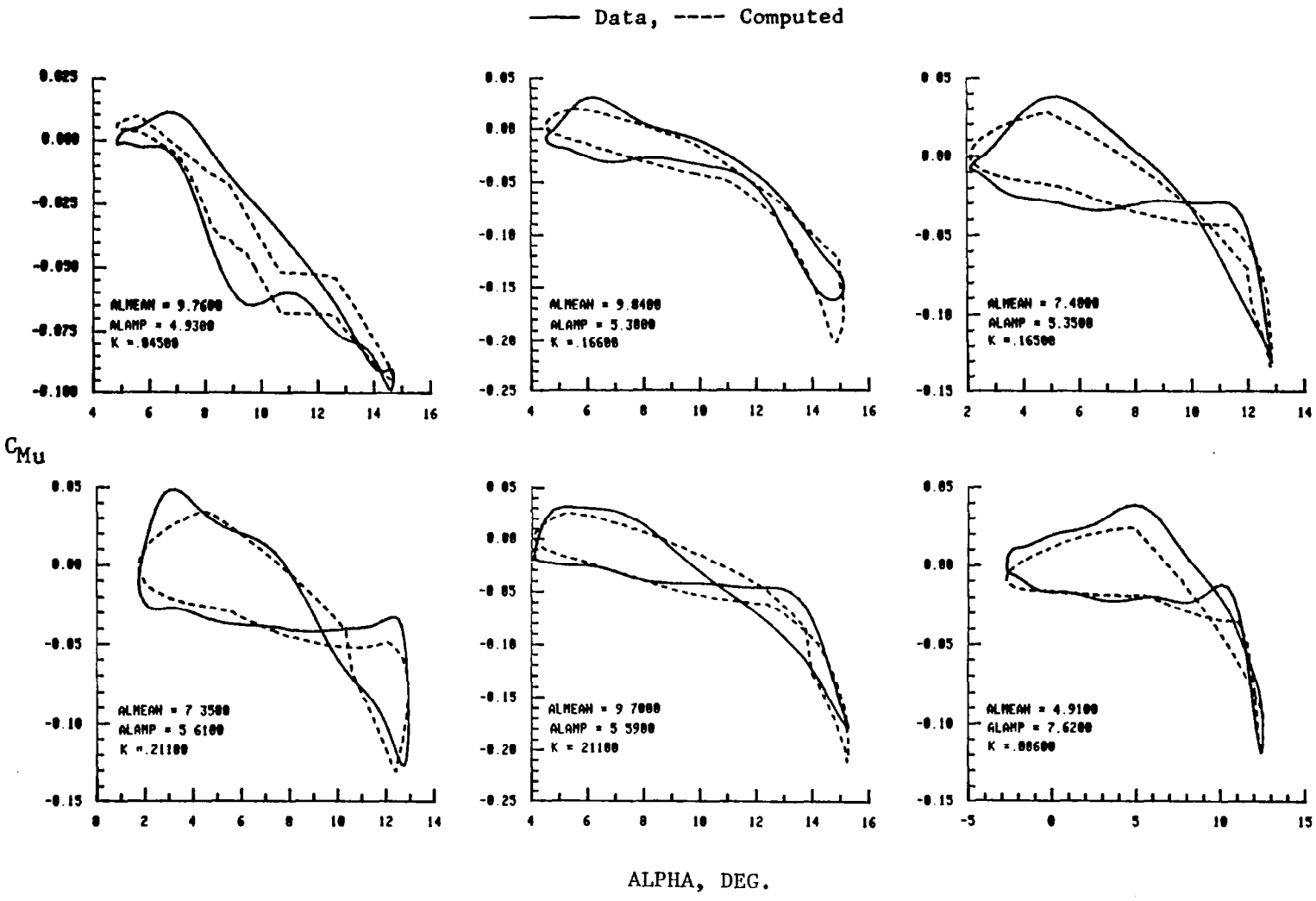

Figure 20b. Comparison Of Synthesized Pitching Moment Coefficient Loops with Test Data

Vertol 0012 Airfoil, M = 0.60, R_n = 6.2 x 10^6, Λ = 0.0 deg

Data Set No. 9 in Table I

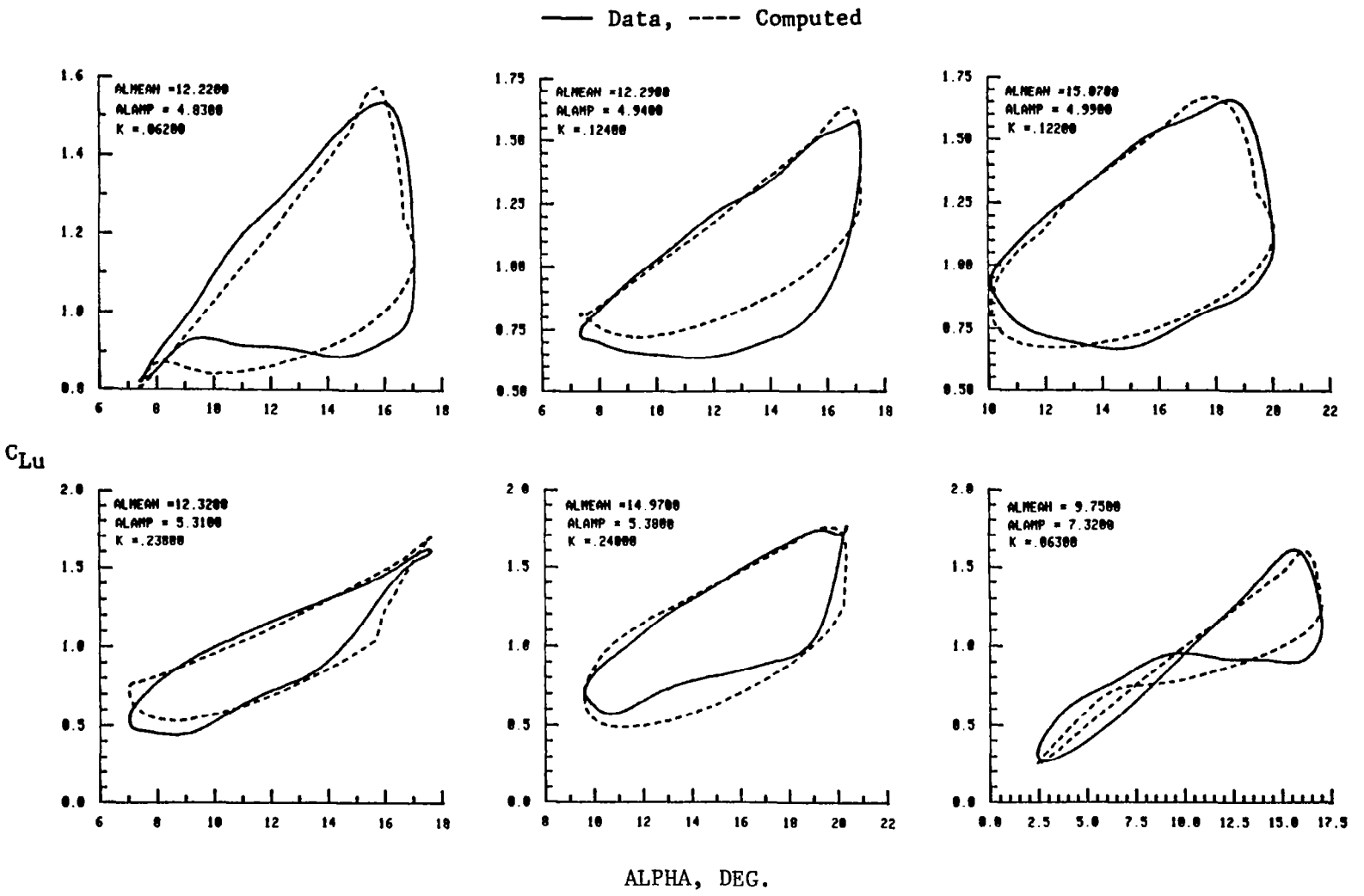

Figure 21a. Comparison of Synthesized Lift Coefficient Loops with Test Data
V2301-1.58 Airfoil, M = 0.40, R_n = 4.8 x 10^6, Λ = 0.0 deg
Data Set No. 10 in Table I

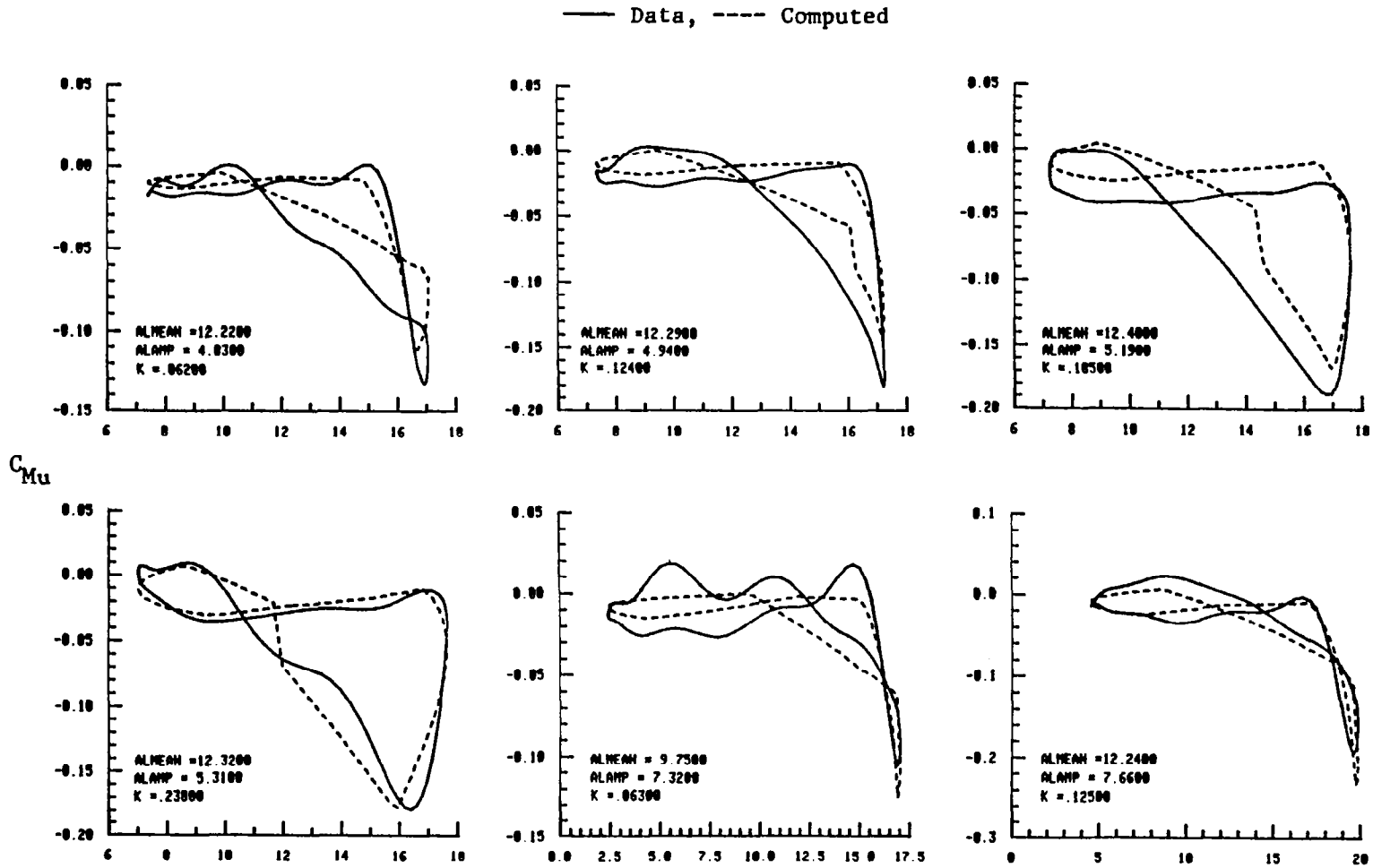

Figure 21b. Comparison Of Synthesized Pitching Moment Coefficient Loops with Test Data V2301-1.58 Airfoil, M = 0.40, R_n = 4.8 x 10^6, Λ = 0.0 deg Data Set No. 10 in Table I

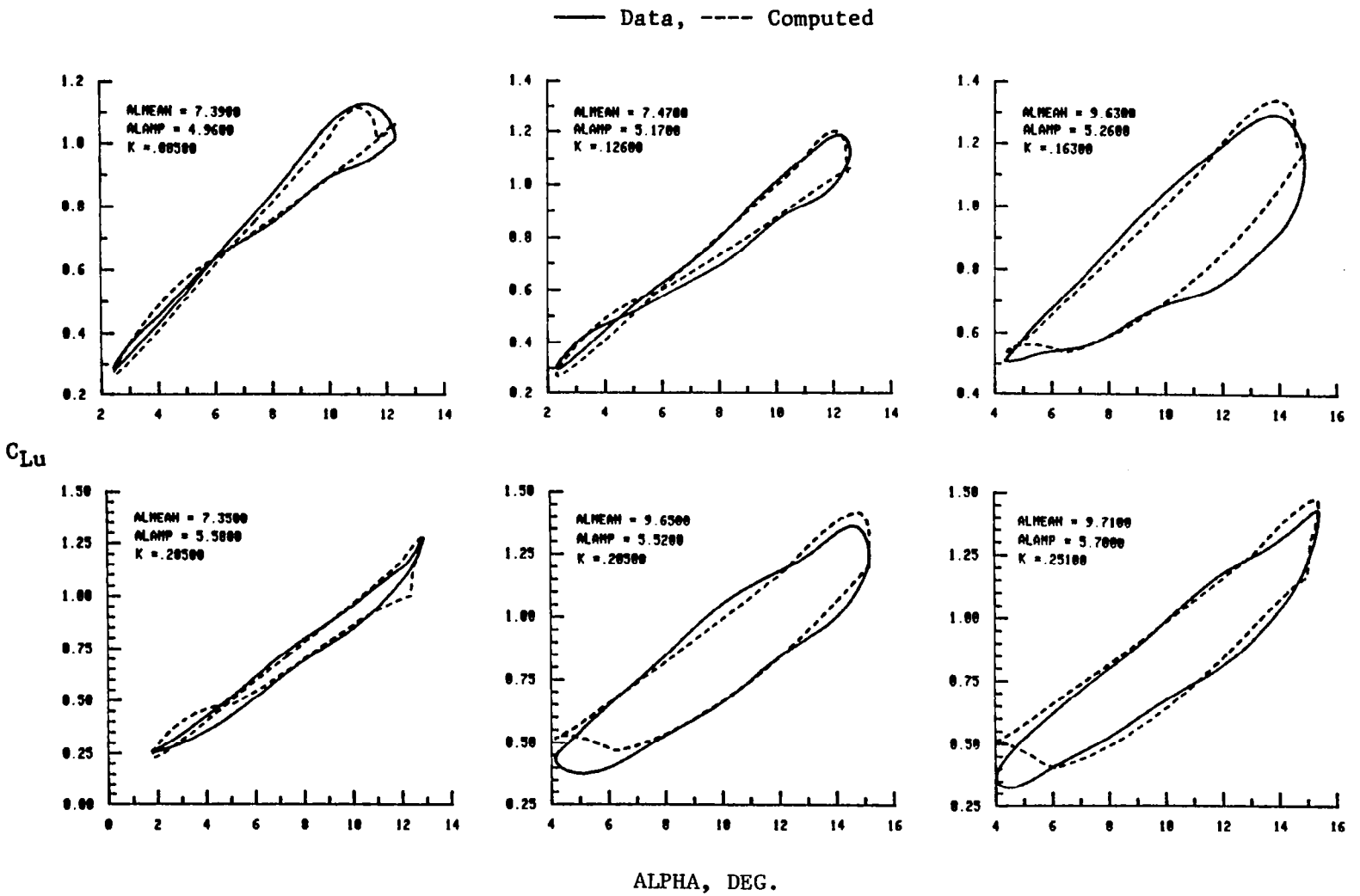

Figure 22a. Comparison of Synthesized Lift Coefficient Loops with Test Data
V2301-1.58 Airfoil, M = 0.60, R_n = 6.2 x 10^6, Λ = 0.0 deg
Data Set No. 11 in Table I

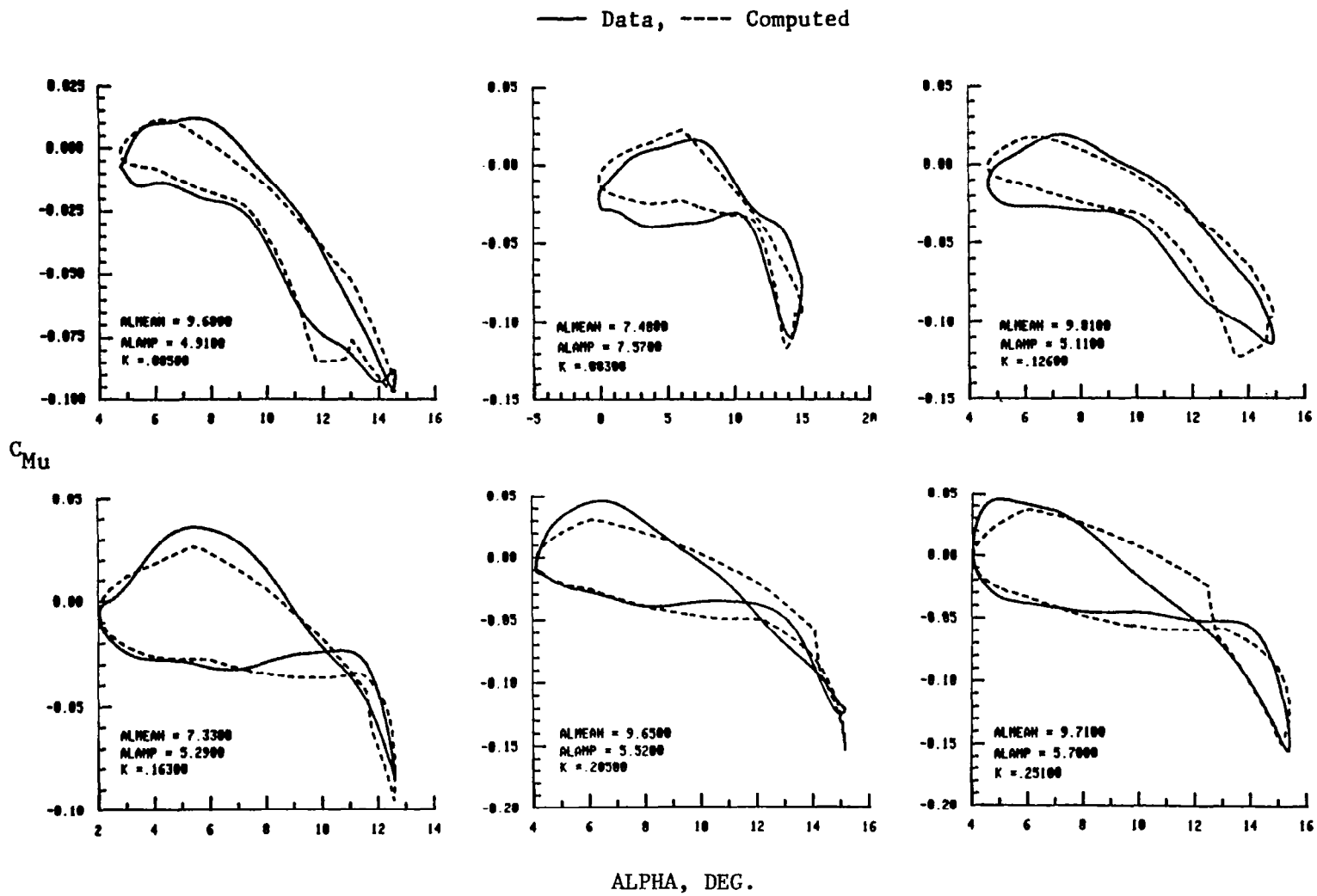

Figure 22b. Comparison Of Synthesized Pitching Moment Coefficient Loops with Test Data

V2301-1.58 Airfoil, M = 0.60, R_n = 6.2 x 10^6, Λ = 0.0 deg

Data Set No. 11 in Table I

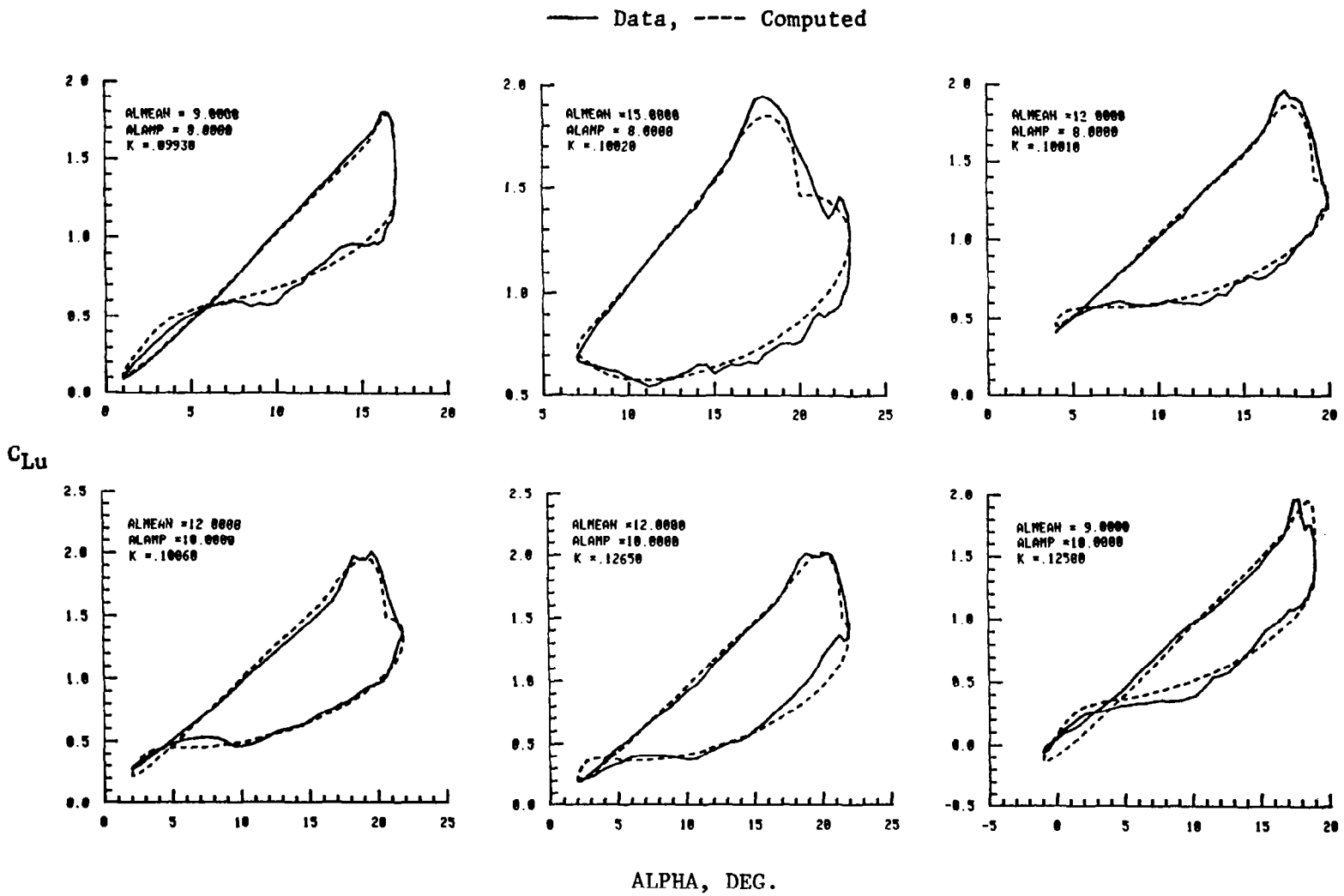

Figure 23a. Comparison of Synthesized Lift Coefficient Loops with Test Data

NACA 0012 Airfoil, M = 0.30, R_n = 2.8 x 10^6, Λ = 0.0 deg

Data Set No. 12 in Table I

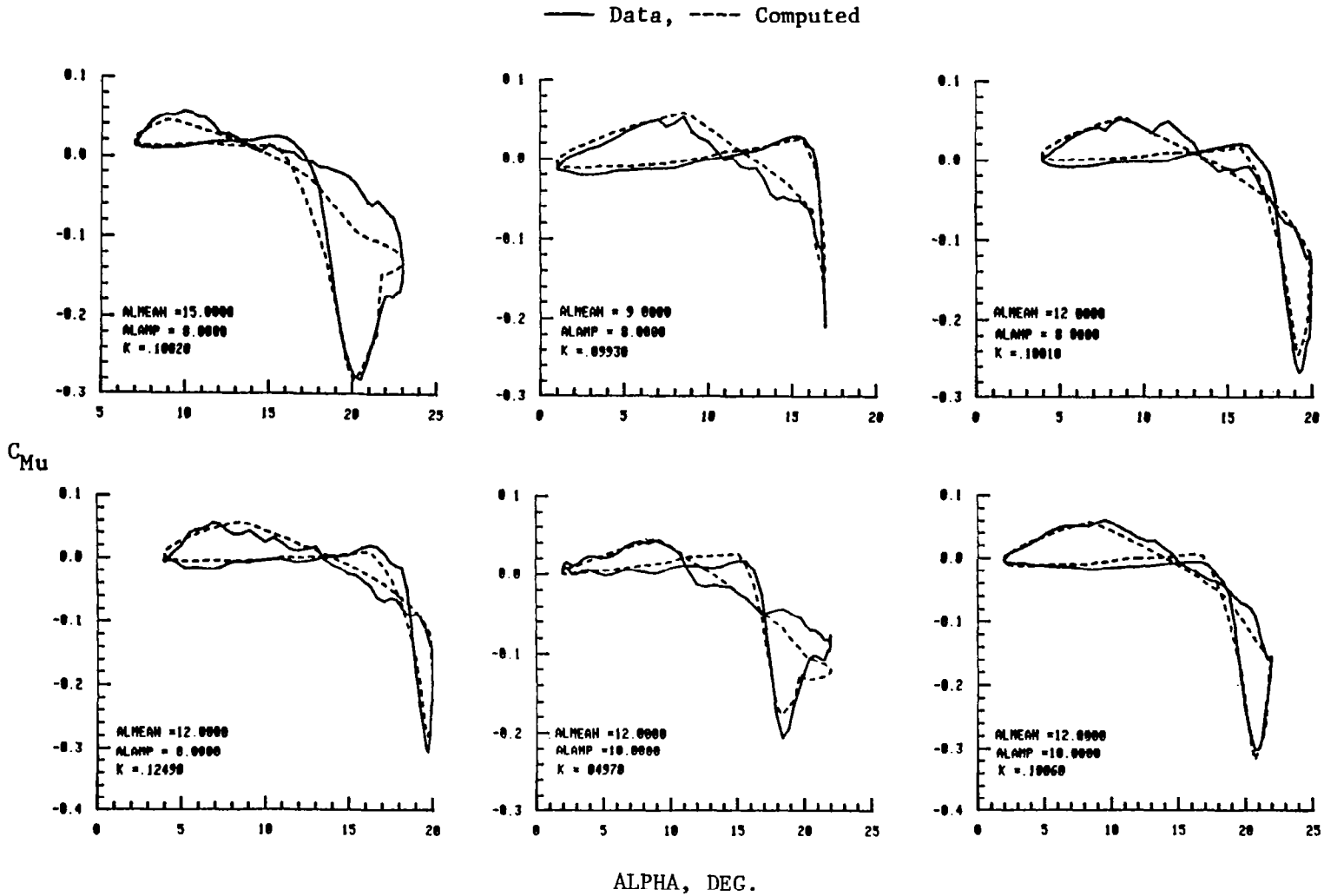

Figure 23b. Comparison Of Synthesized Pitching Moment Coefficient Loops with Test Data

NACA 0012 Airfoil, M = 0.30, R_n = 2.8 x 10^6, Λ = 0.0 deg

Data Set No. 12 in Table I

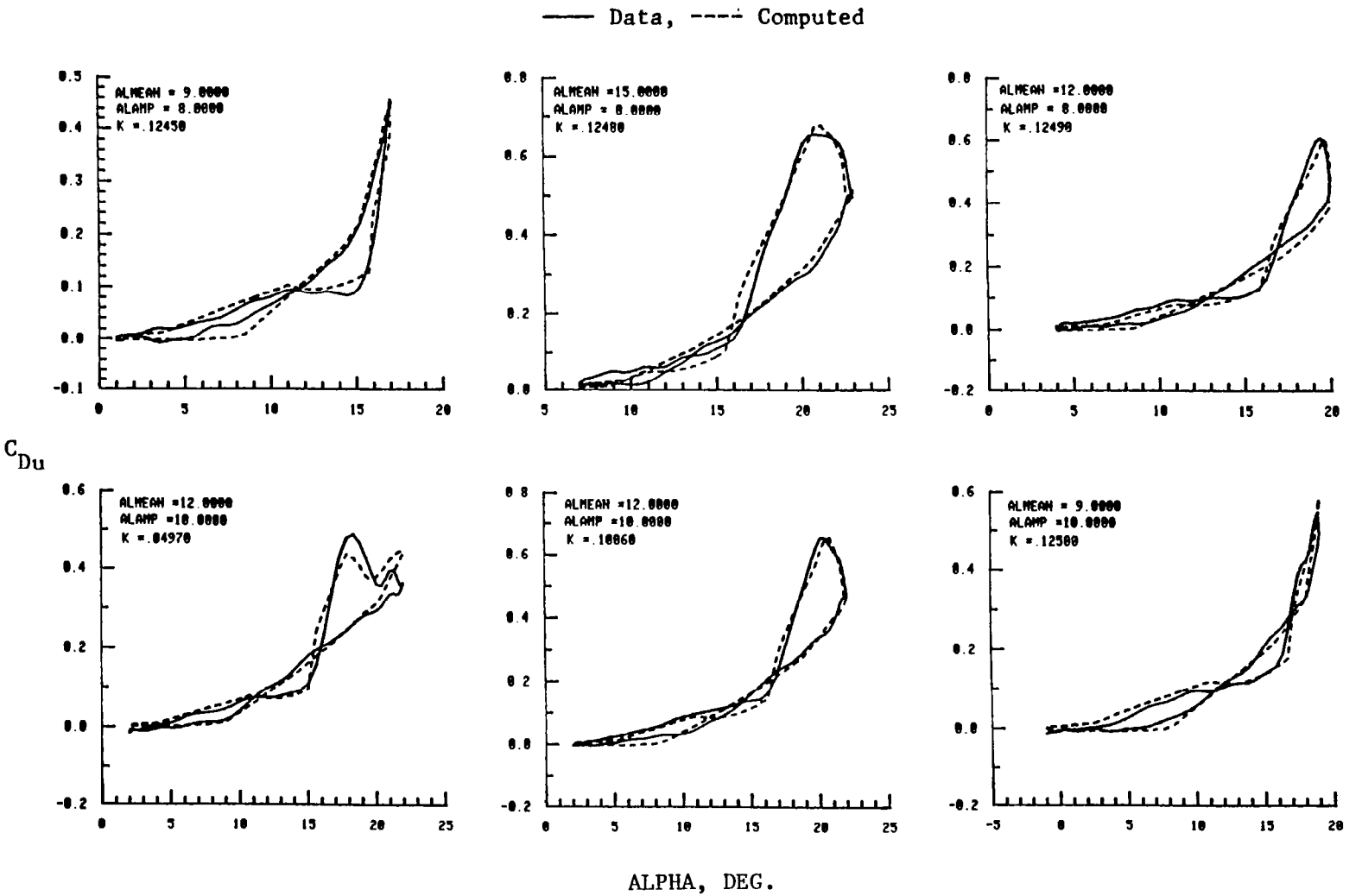

Figure 23c. Comparison Of Synthesized Drag Coefficient Loops with Test Data

NACA 0012 Airfoil, M = 0.30, R_n = 2.8 x 10^6, Λ = 0.0 deg

Data Set No. 12 in Table I

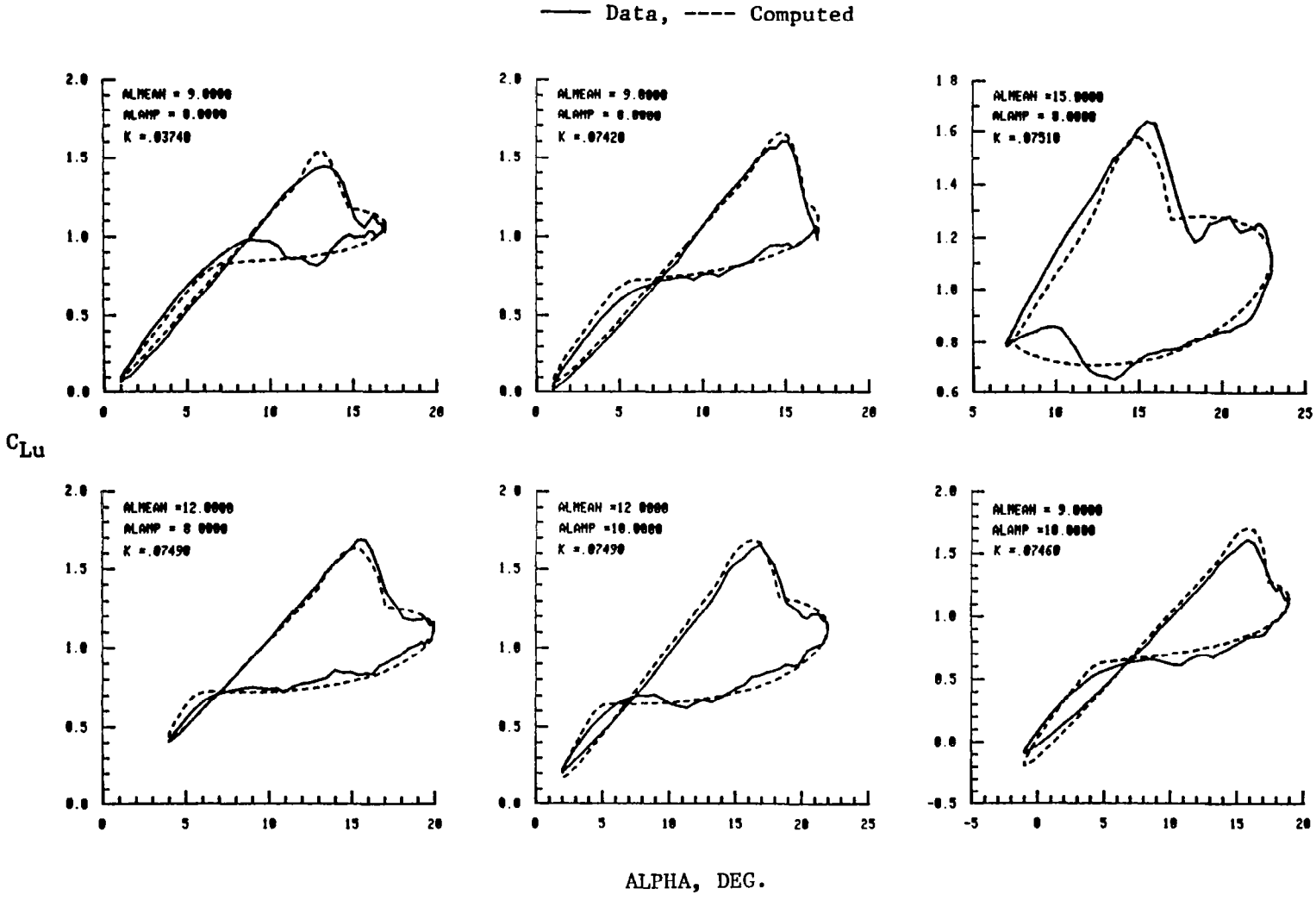

Figure 24a. Comparison of Synthesized Lift Coefficient Loops with Test Data

NACA 0012 Airfoil, M = 0.40, R_n = 3.7 x 10^6, Λ = 0.0 deg

Data Set No. 13 in Table I

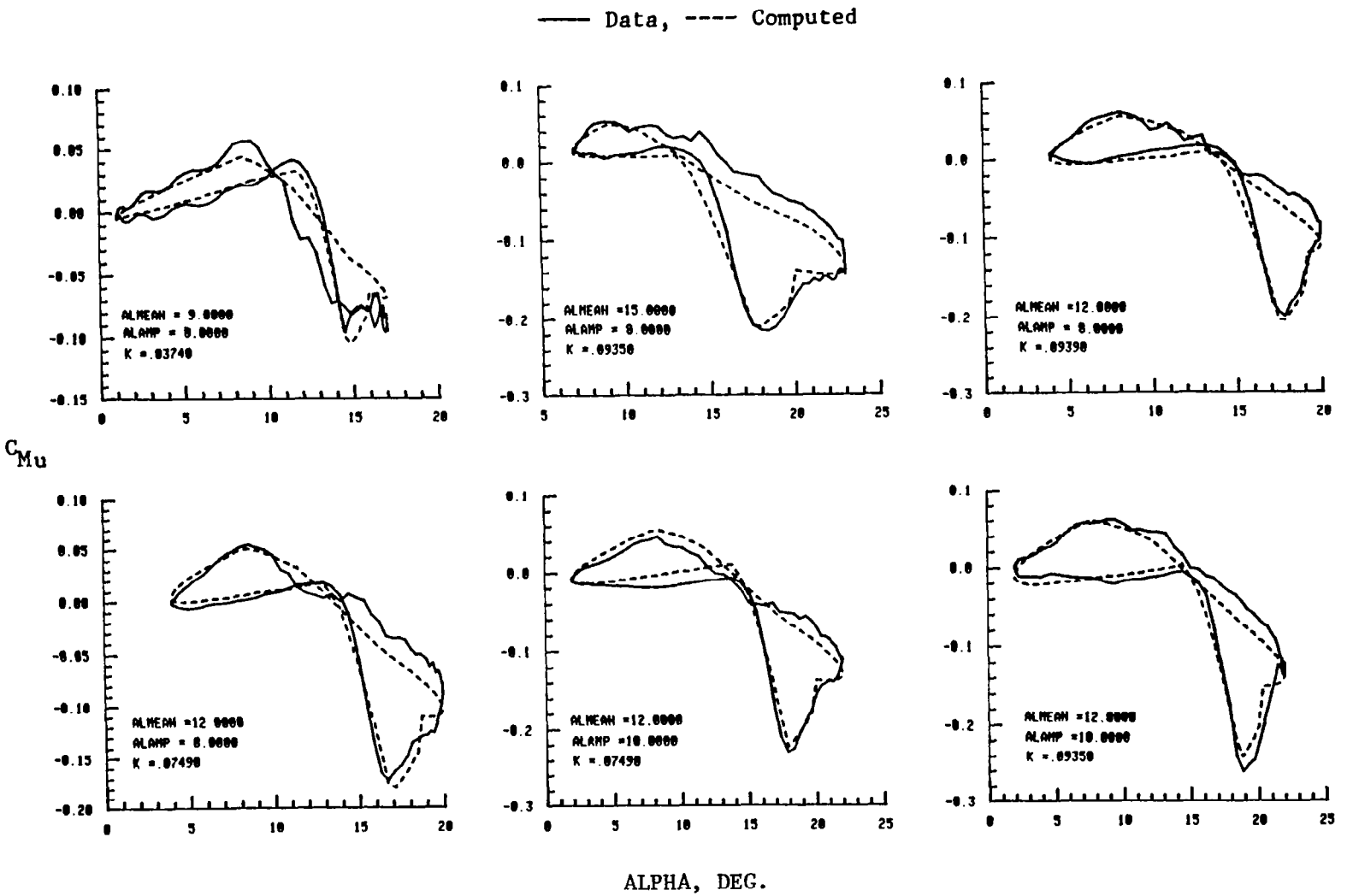

Figure 24b. Comparison Of Synthesized Pitching Moment Coefficient Loops with Test Data

NACA 0012 Airfoil, M = 0.40, R_n = 3.7 x 10^6, Λ = 0.0 deg

Data Set No. 13 in Table I

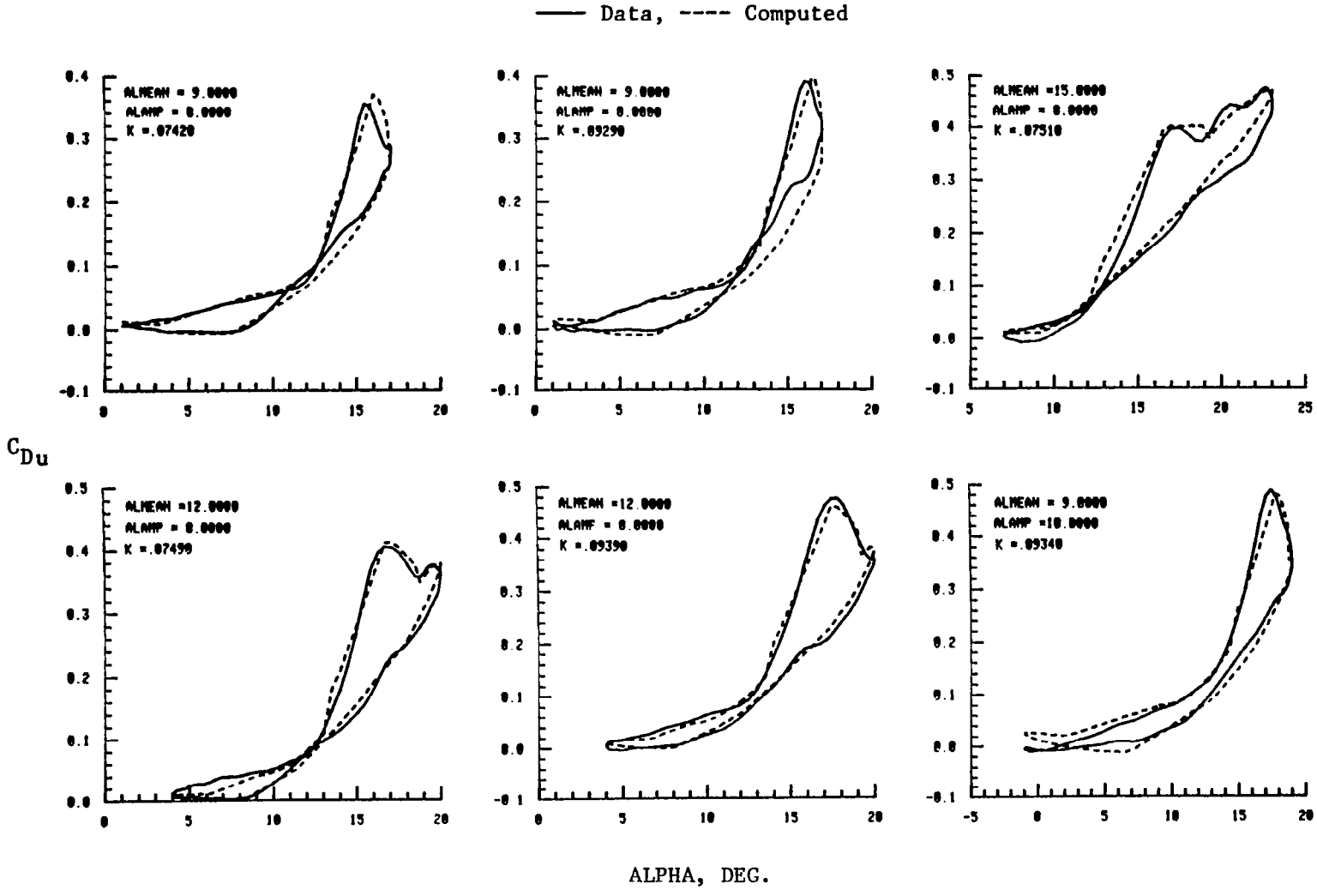

Figure 24c. Comparison Of Synthesized Drag Coefficient Loops with Test Data

NACA 0012 Airfoil, M = 0.40, R_n = 3.7 x 10^6, Λ = 0.0 deg

Data Set No. 13 in Table I

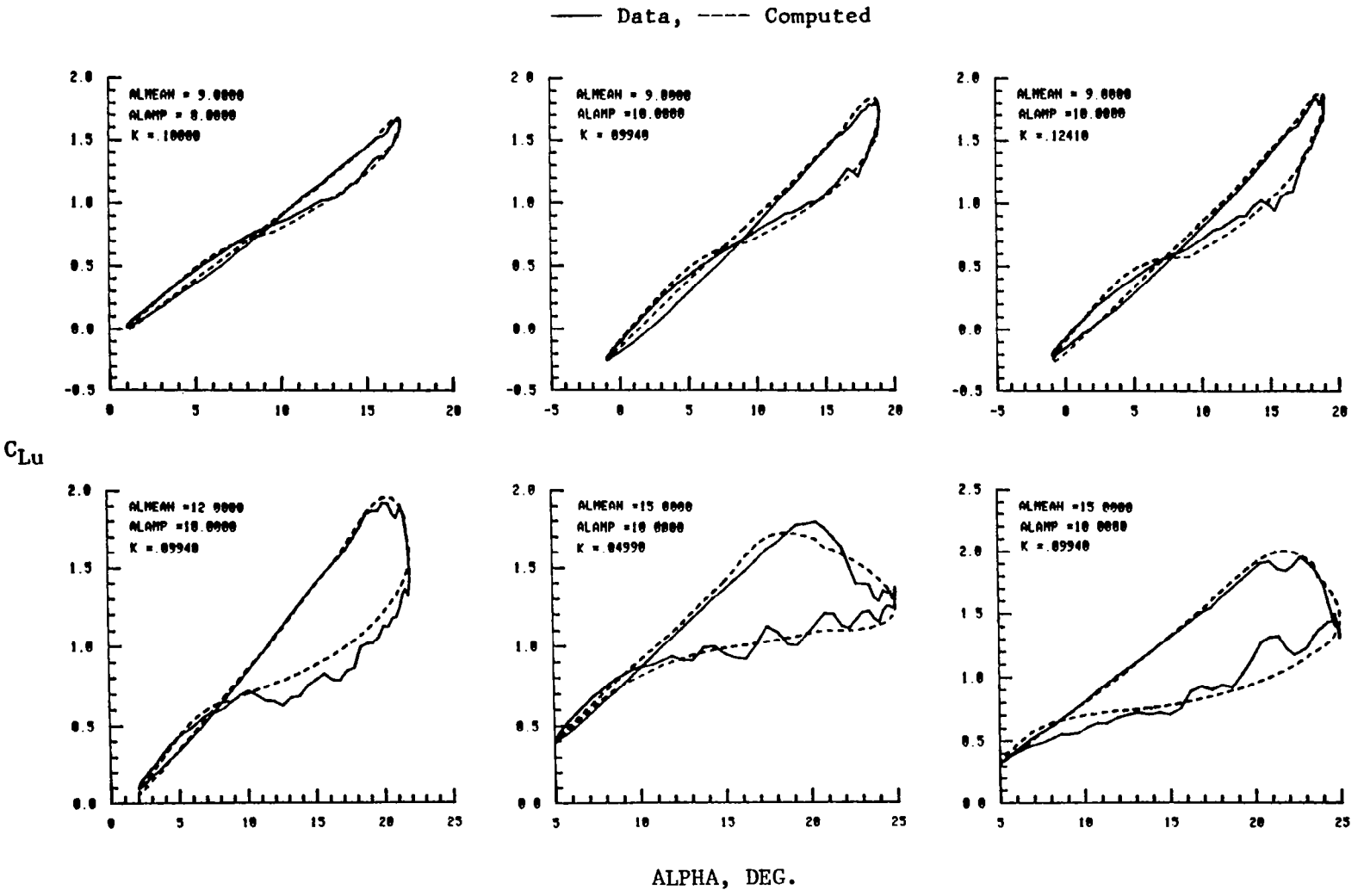

Figure 25a. Comparison of Synthesized Lift Coefficient Loops with Test Data

NACA 0012 Airfoil, M = 0.30, R_n = 3.2 x 10^6, Λ = 30.0 deg

Data Set No. 14 in Table I

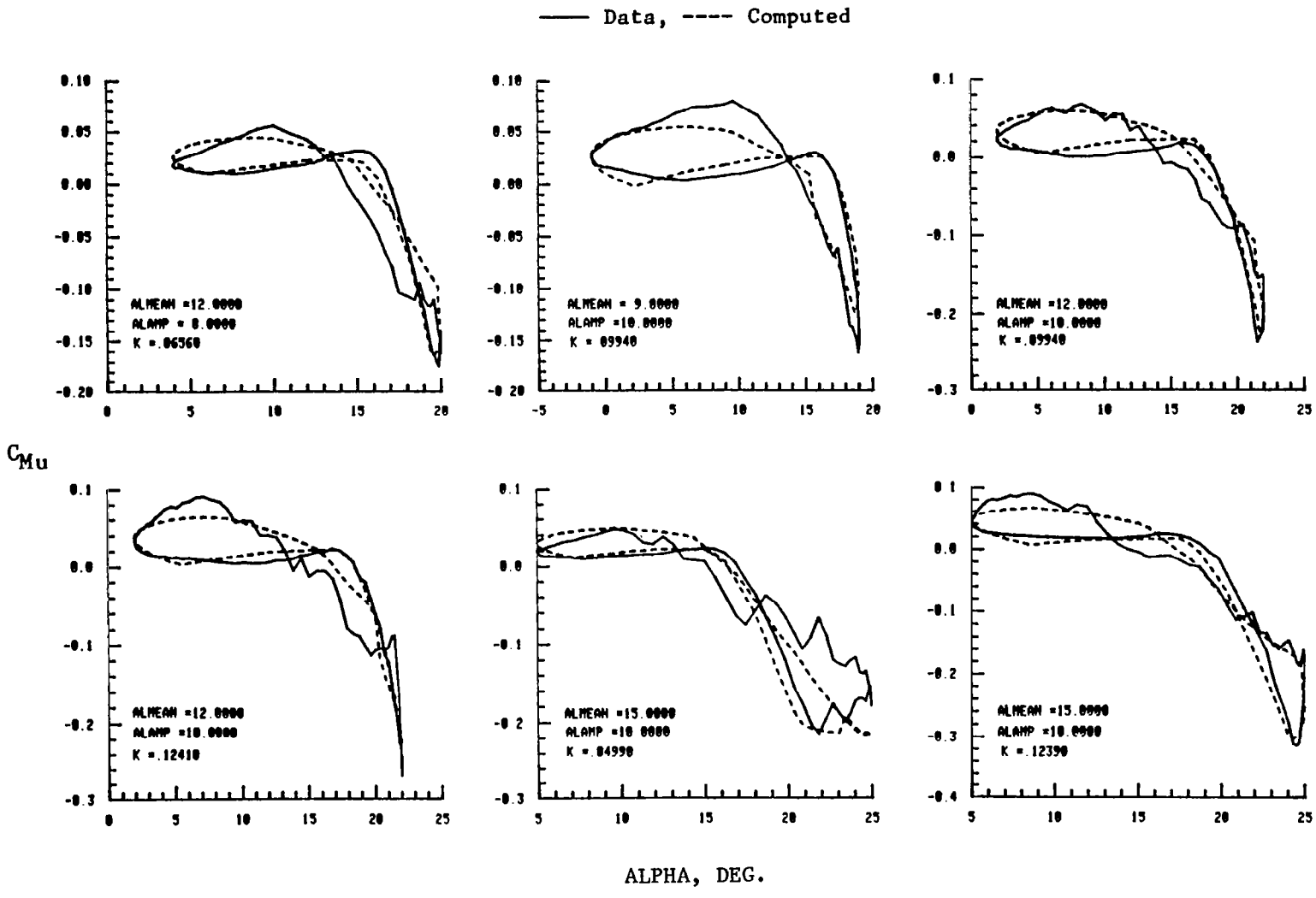

Figure 25b. Comparison Of Synthesized Pitching Moment Coefficient Loops with Test Data

NACA 0012 Airfoil, M = 0.30, R_n = 3.2 x 10^6, Λ = 30.0 deg

Data Set No. 14 in Table I

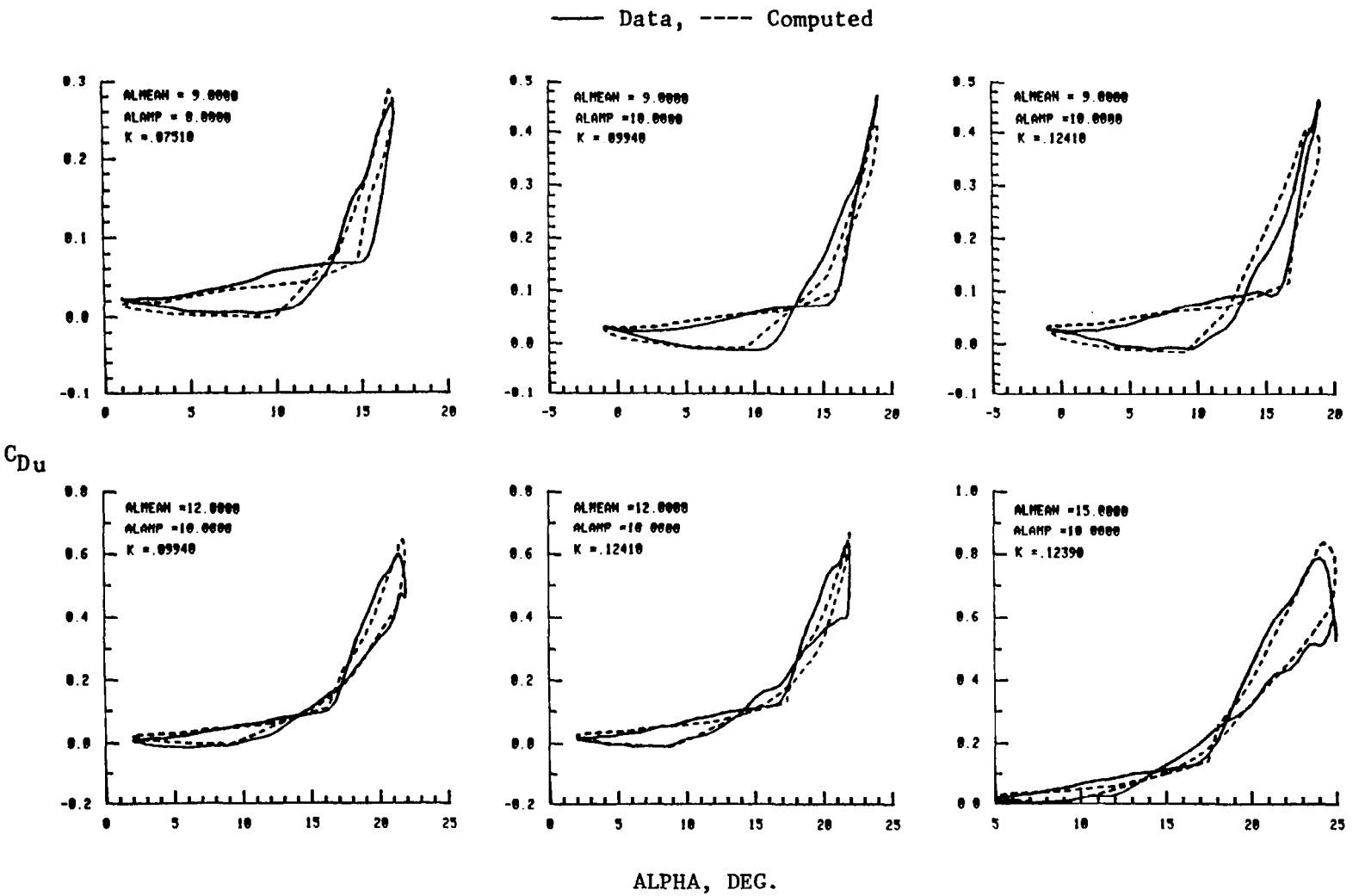

Figure 25c. Comparison Of Synthesized Drag Coefficient Loops with Test Data

NACA 0012 Airfoil, M = 0.30, R_n = 3.2 x 10^6, Λ = 30.0 deg

Data Set No. 14 in Table I

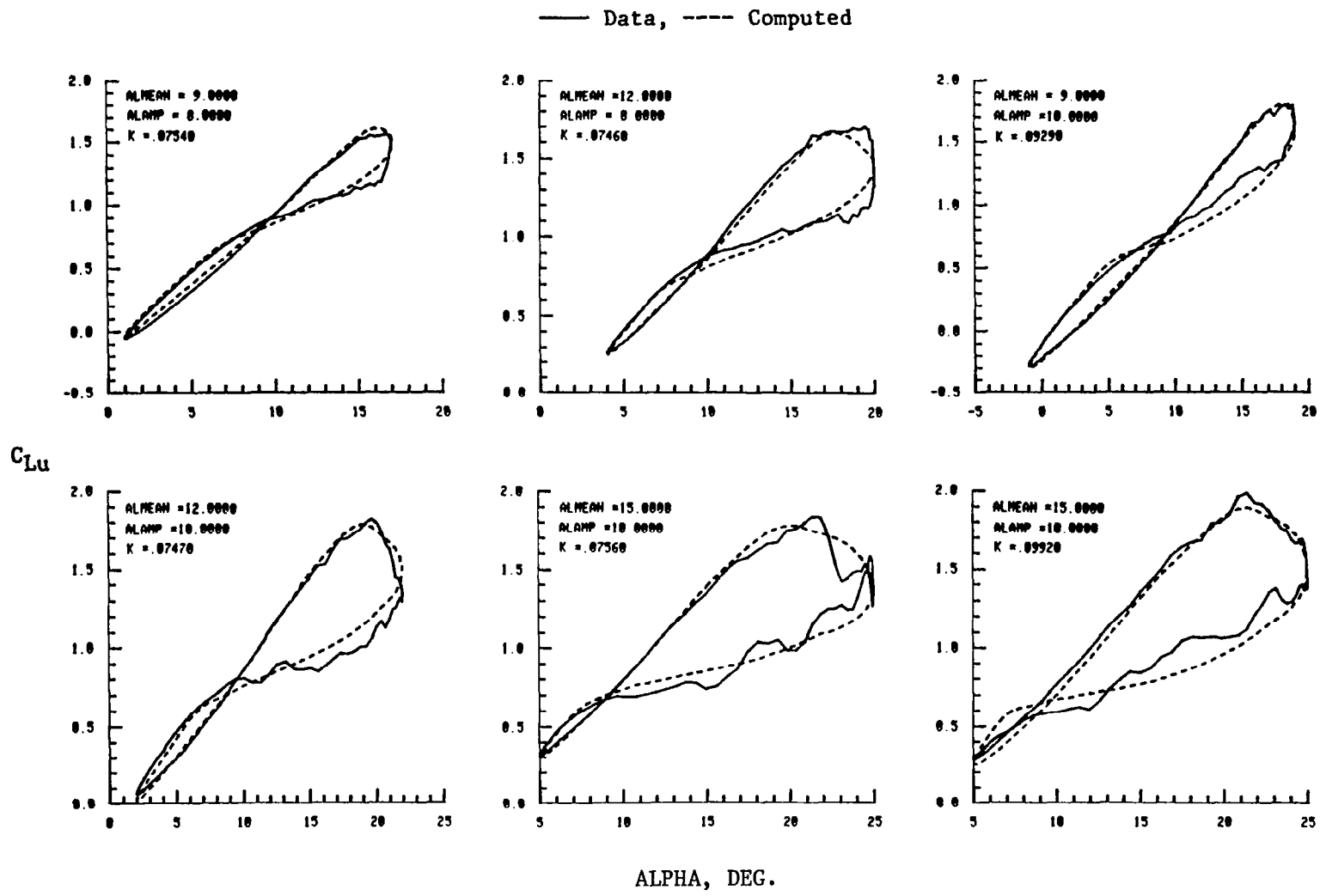

Figure 26a. Comparison of Synthesized Lift Coefficient Loops with Test Data

NACA 0012 Airfoil, M = 0.40, R_n = 4.3 x 10^6, Λ = 30.0 deg

Data Set No. 15 in Table I

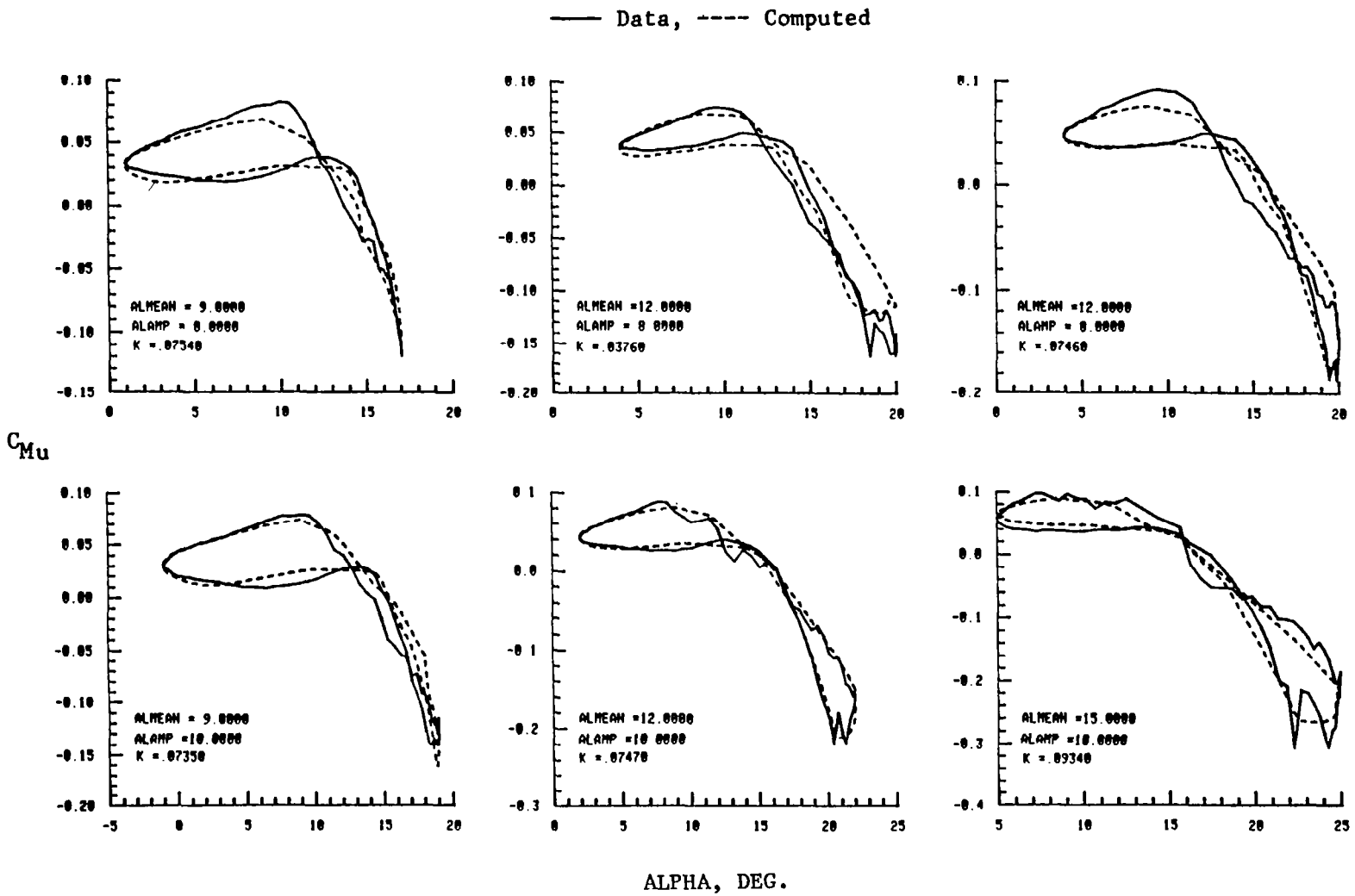

Figure 26b. Comparison Of Synthesized Pitching Moment Coefficient Loops with Test Data

NACA 0012 Airfoil, M = 0.40, R_n = 4.3 x 10^6, Λ = 30.0 deg

Data Set No. 15 in Table I

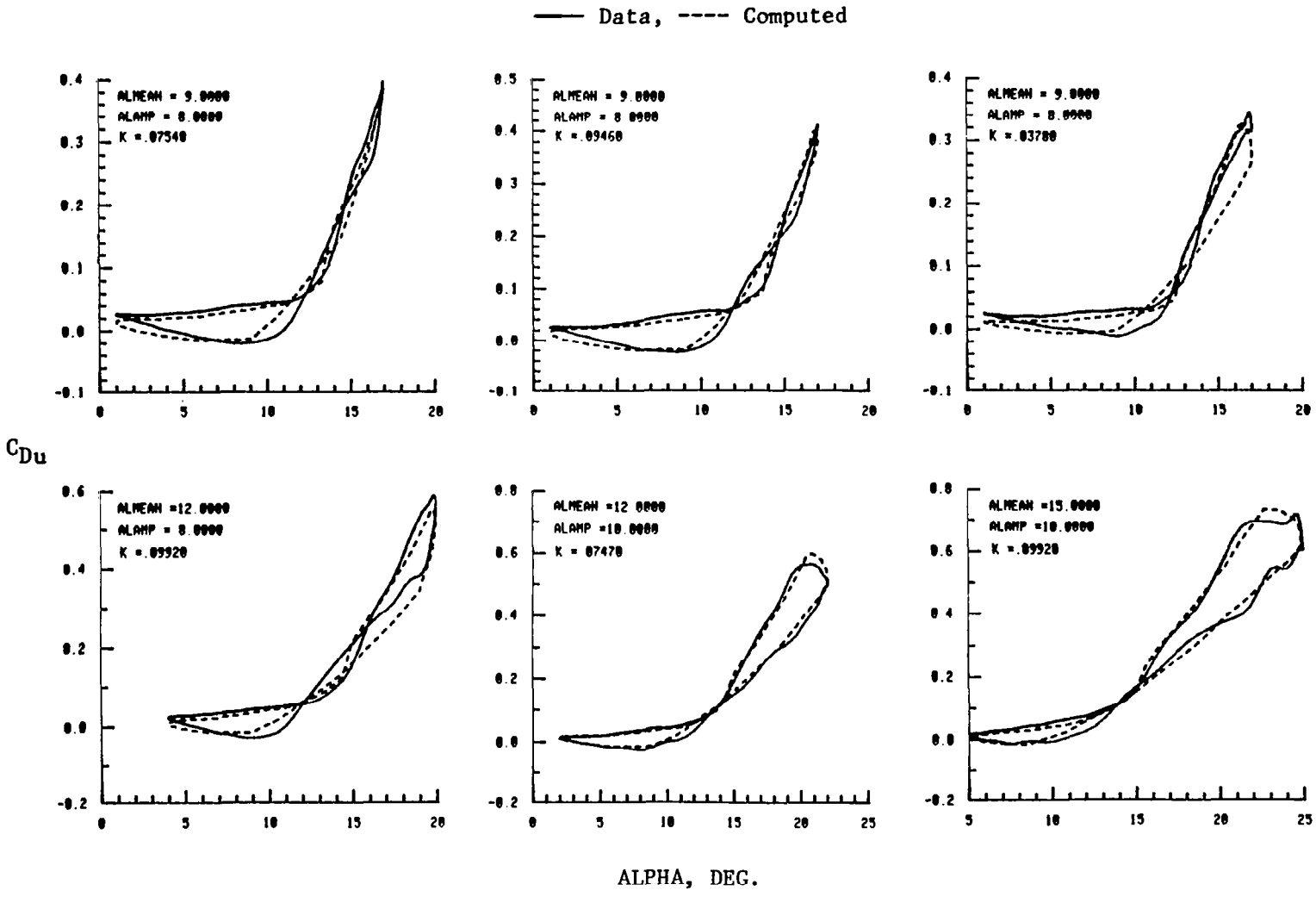

Figure 26c. Comparison Of Synthesized Drag Coefficient Loops with Test Data

NACA 0012 Airfoil, M = 0.40, R_n = 4.3 x 10^6, Λ = 30.0 deg

Data Set No. 15 in Table I

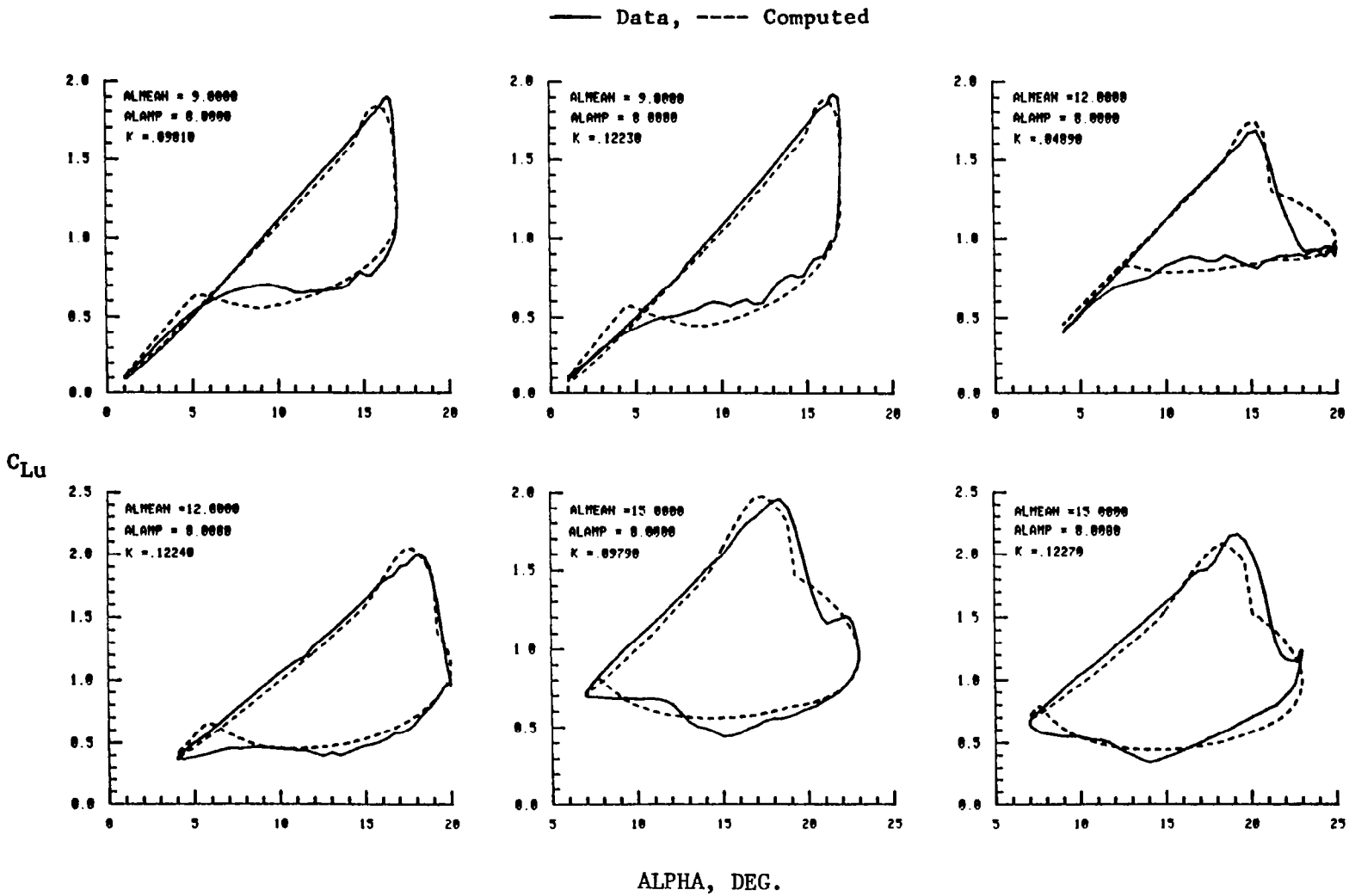

Figure 27a. Comparison of Synthesized Lift Coefficient Loops with Test Data

SC 1095 Airfoil, M = 0.30, R_n = 2.8 x 10^6, Λ = 0.0 deg

Data Set No. 16 in Table I

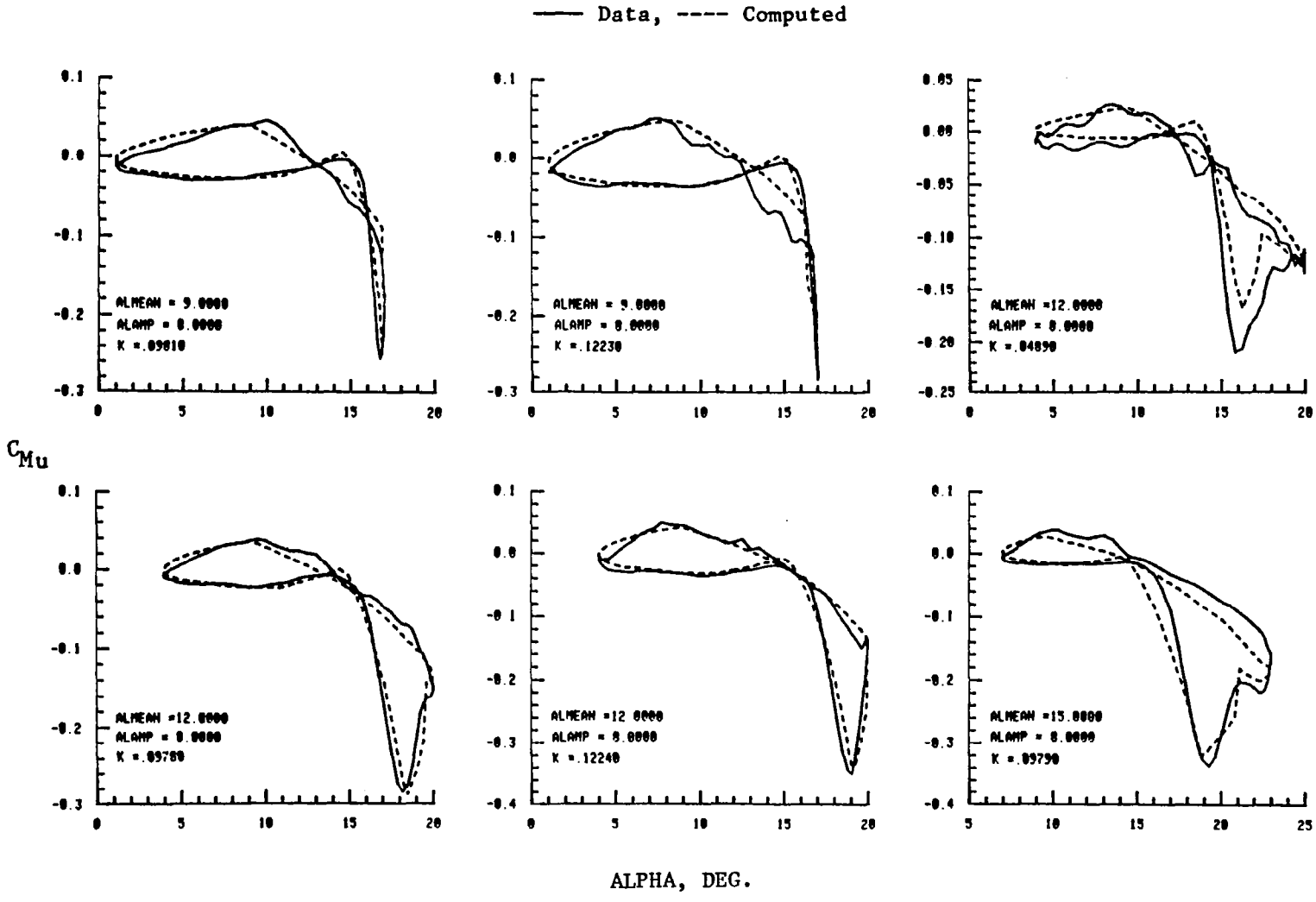

Figure 27b. Comparison Of Synthesized Pitching Moment Coefficient Loops with Test Data

SC 1095 Airfoil, M = 0.30, R_n = 2.8 x 10^6, Λ = 0.0 deg

Data Set No. 16 in Table I

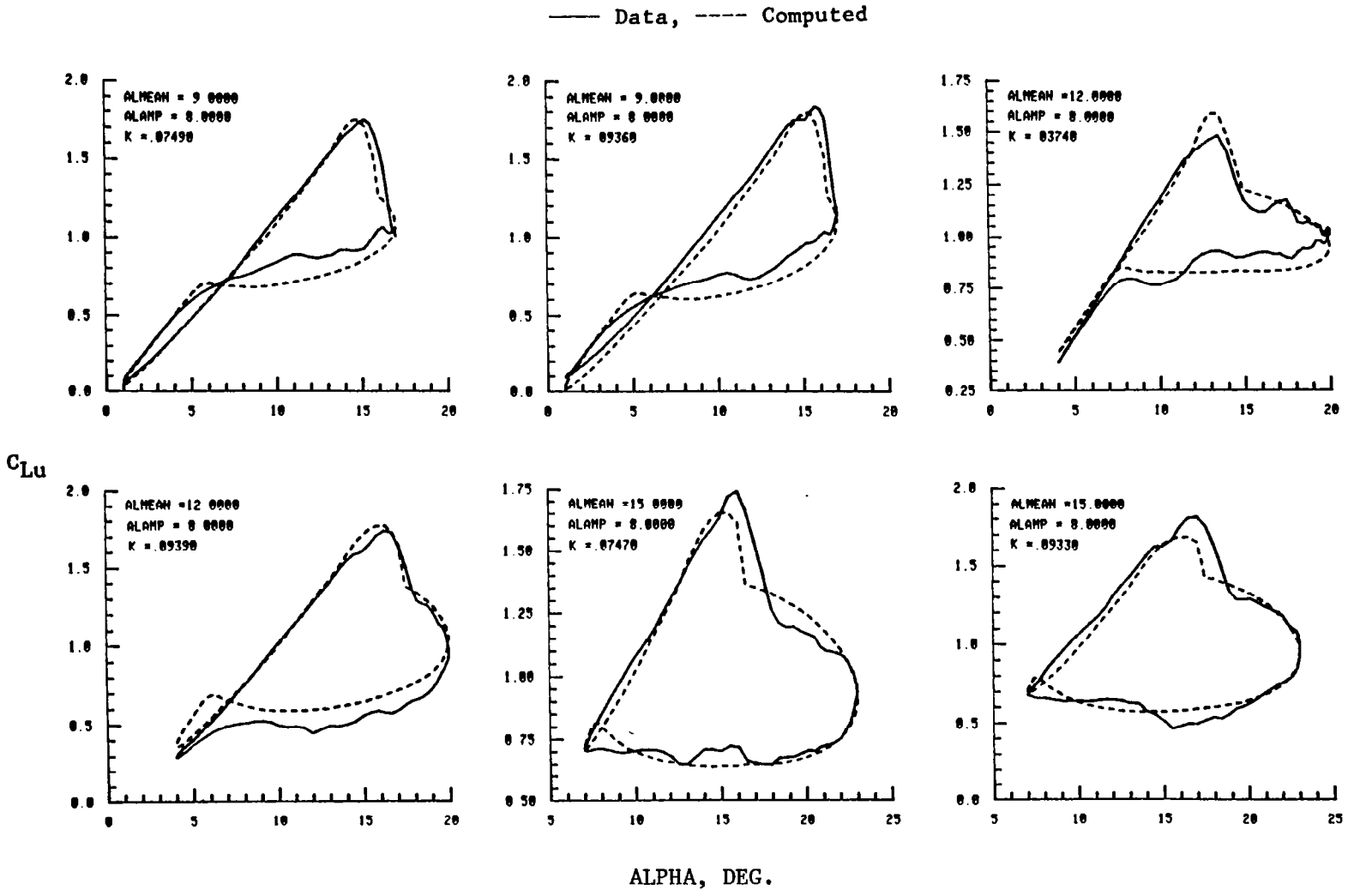

Figure 28a. Comparison of Synthesized Lift Coefficient Loops with Test Data

SC 1095 Airfoil, M = 0.40, R_n = 3.7 x 10^6, Λ = 0.0 deg

Data Set No. 17 in Table I

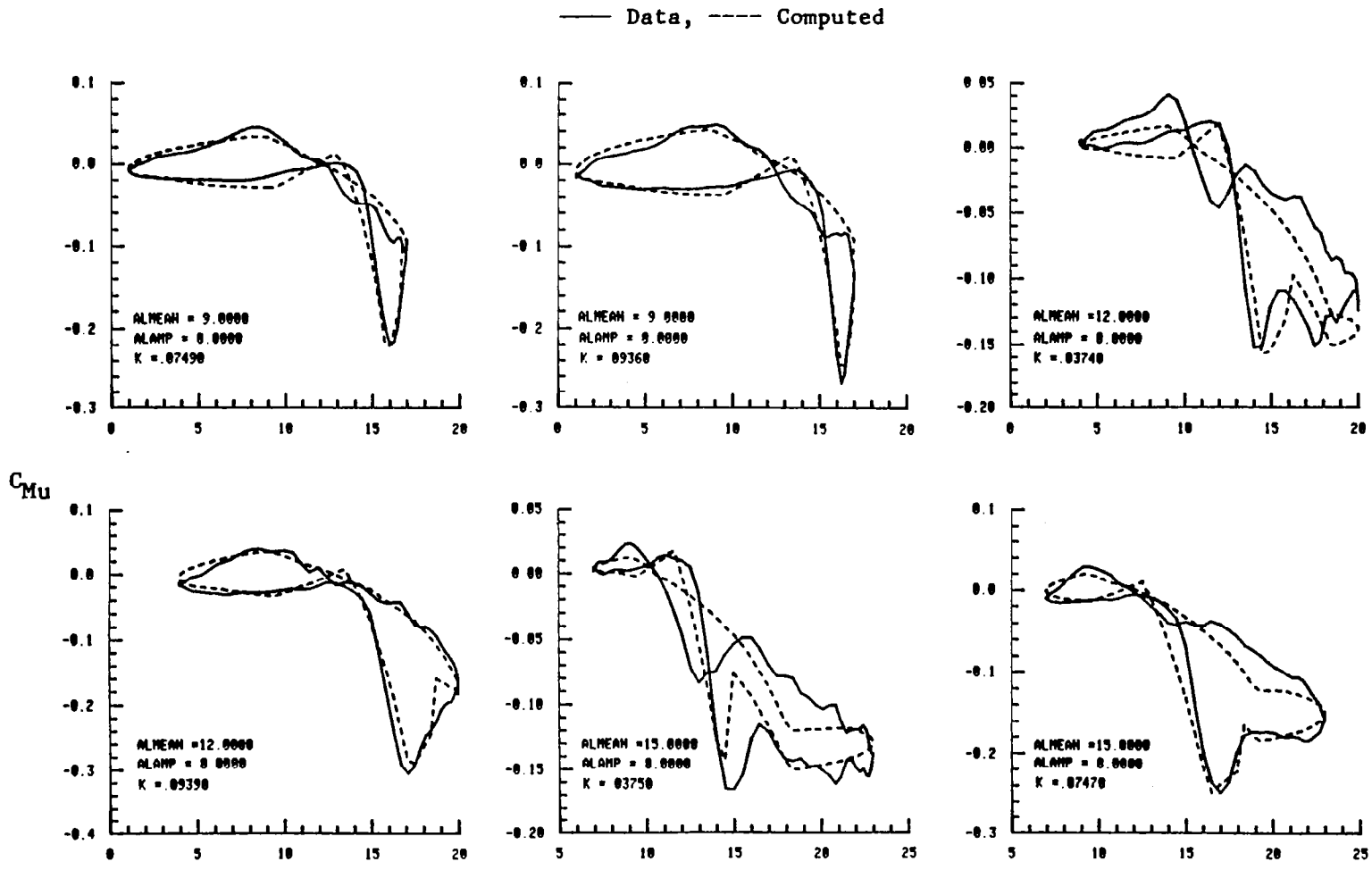

Figure 28b. Comparison Of Synthesized Pitching Moment Coefficient Loops with Test Data

SC 1095 Airfoil, M = 0.40, R_n = 3.7 x 10^6, Λ = 0.0 deg

Data Set No. 17 in Table I

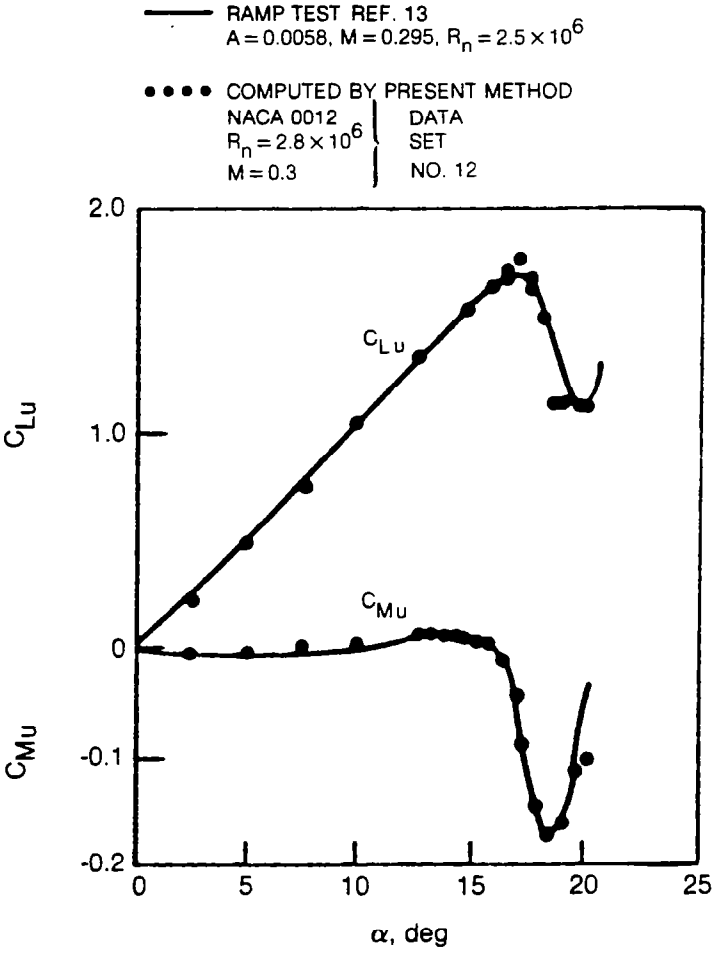

Figure 29. Correlation of Computed Unsteady Data with Test Data for Ramp Function Angle of Attack Distribution

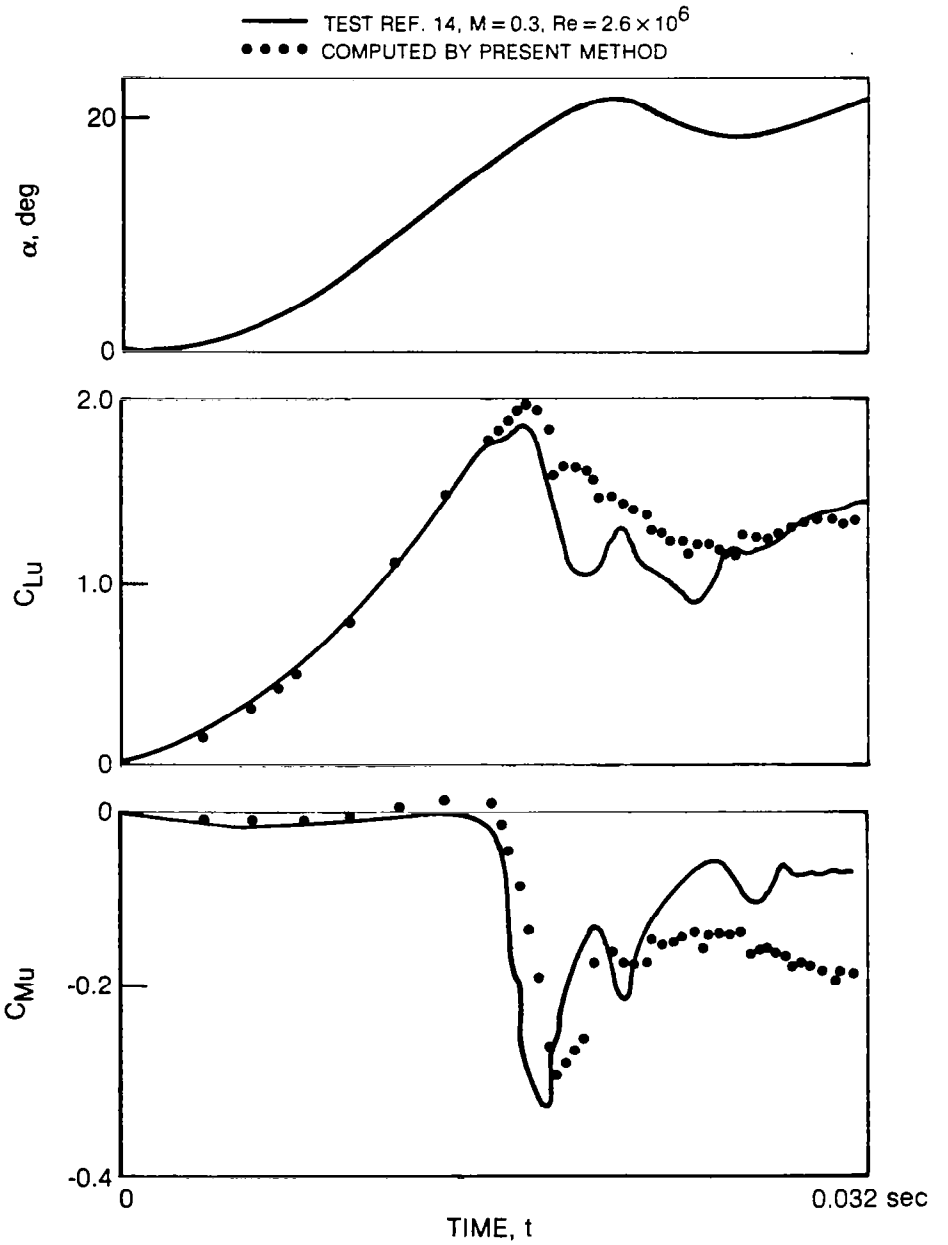

Figure 30. Correlation Between Predicted Results and Test Data for Isolated Airfoil

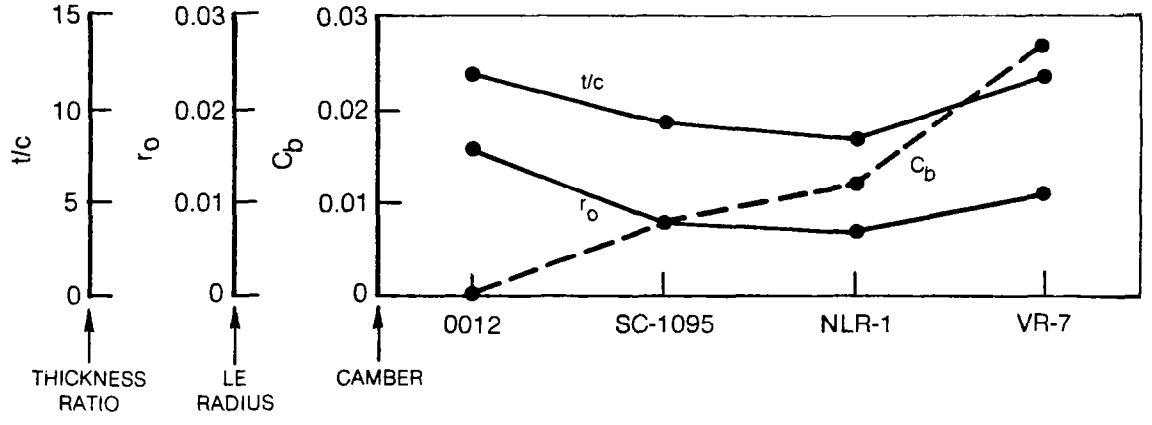

a) GEOMETRIC CHARACTERISTICS

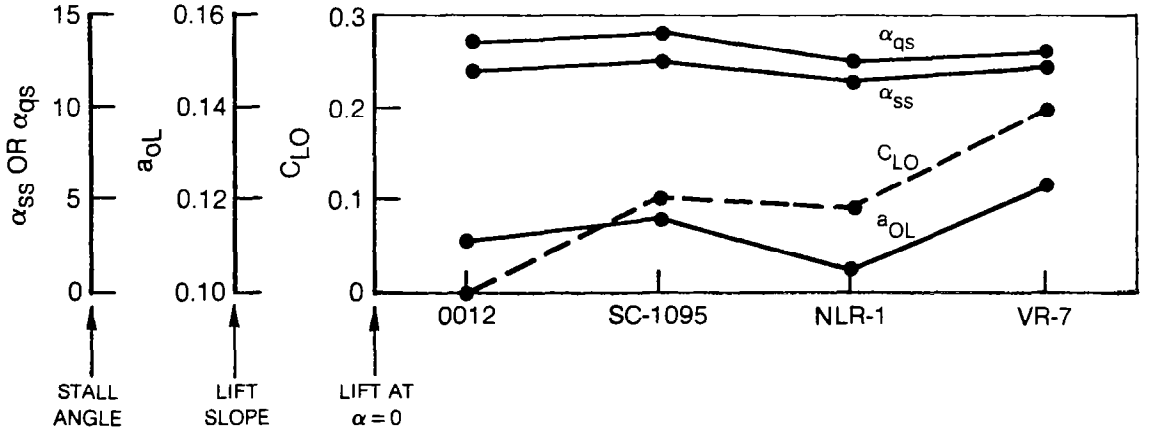

b) AERODYNAMIC CHARACTERISTICS

Figure 31. Variation of Geometric Static and Quasi-static Aerodynamic Characteristics with Airfoil ($M = 0.3$, $R_n = 3.8 \times 10^6$)

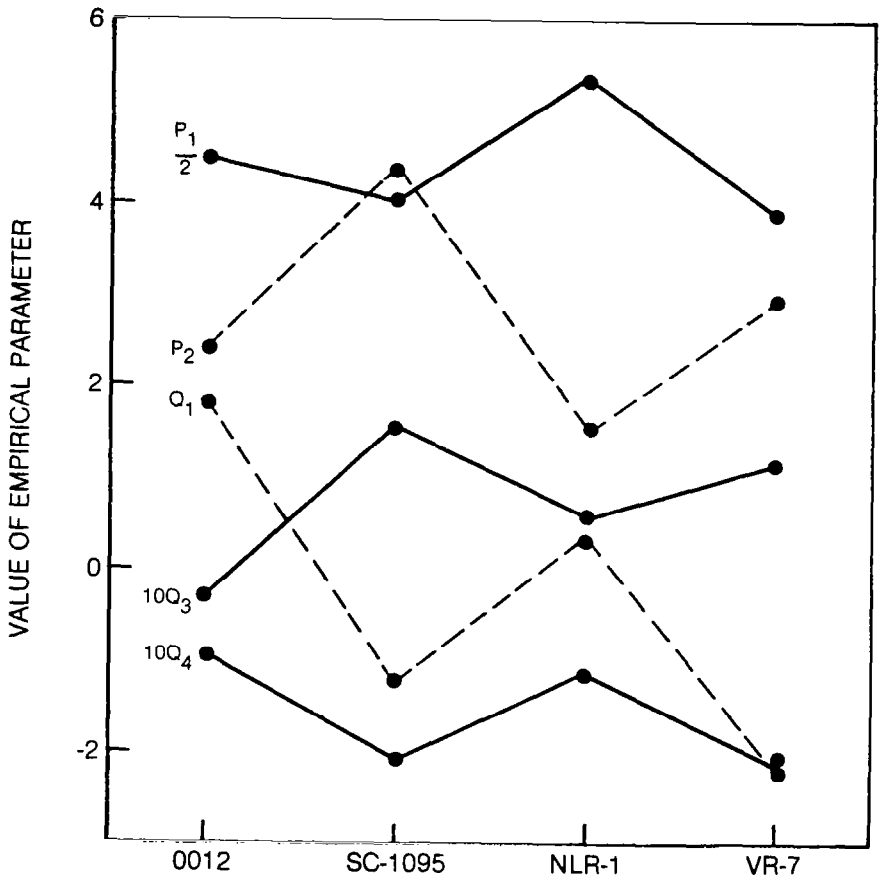

Figure 32a. Variation of Unsteady Lift Empirical Parameters with Airfoil ($M = 0.3$, $R_n = 3.8 \times 10^6$)

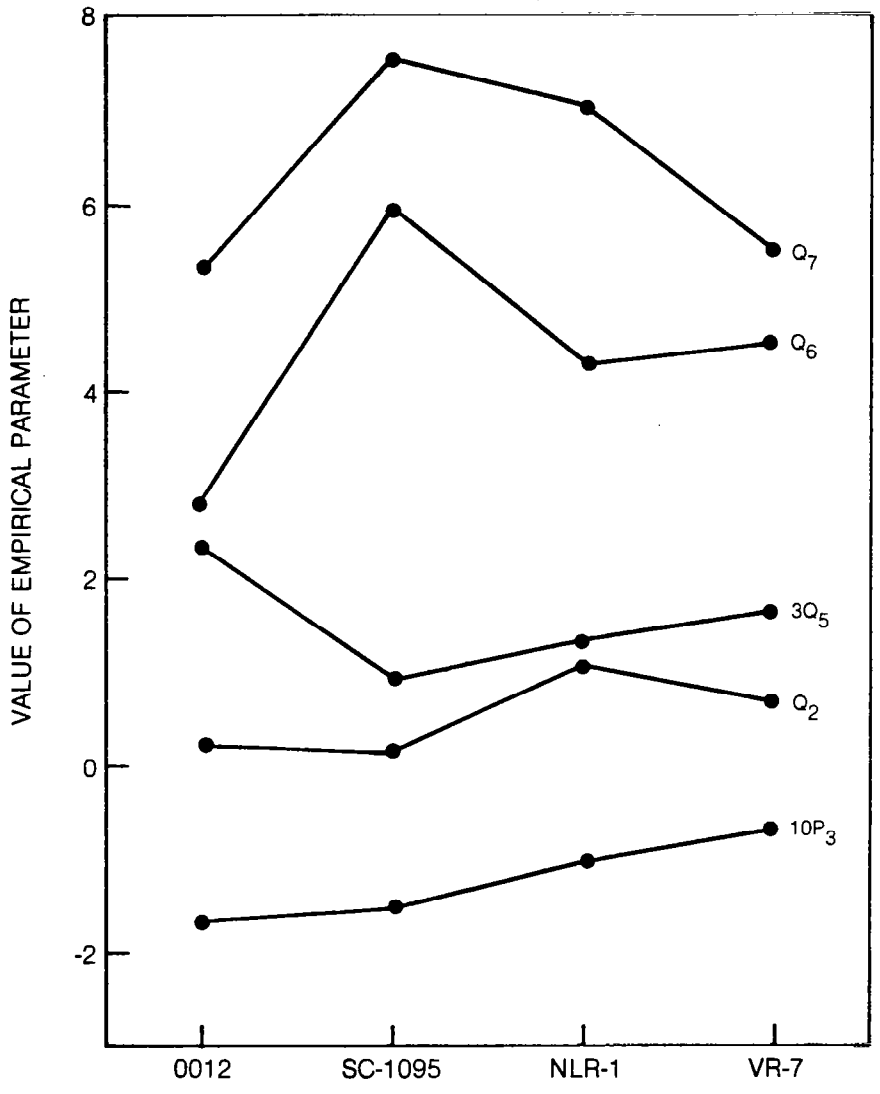

Figure 32b. Variation of Unsteady Lift Empirical Parameters with Airfoil ($M = 0.3$, $R_n = 3.8 \times 10^6$)

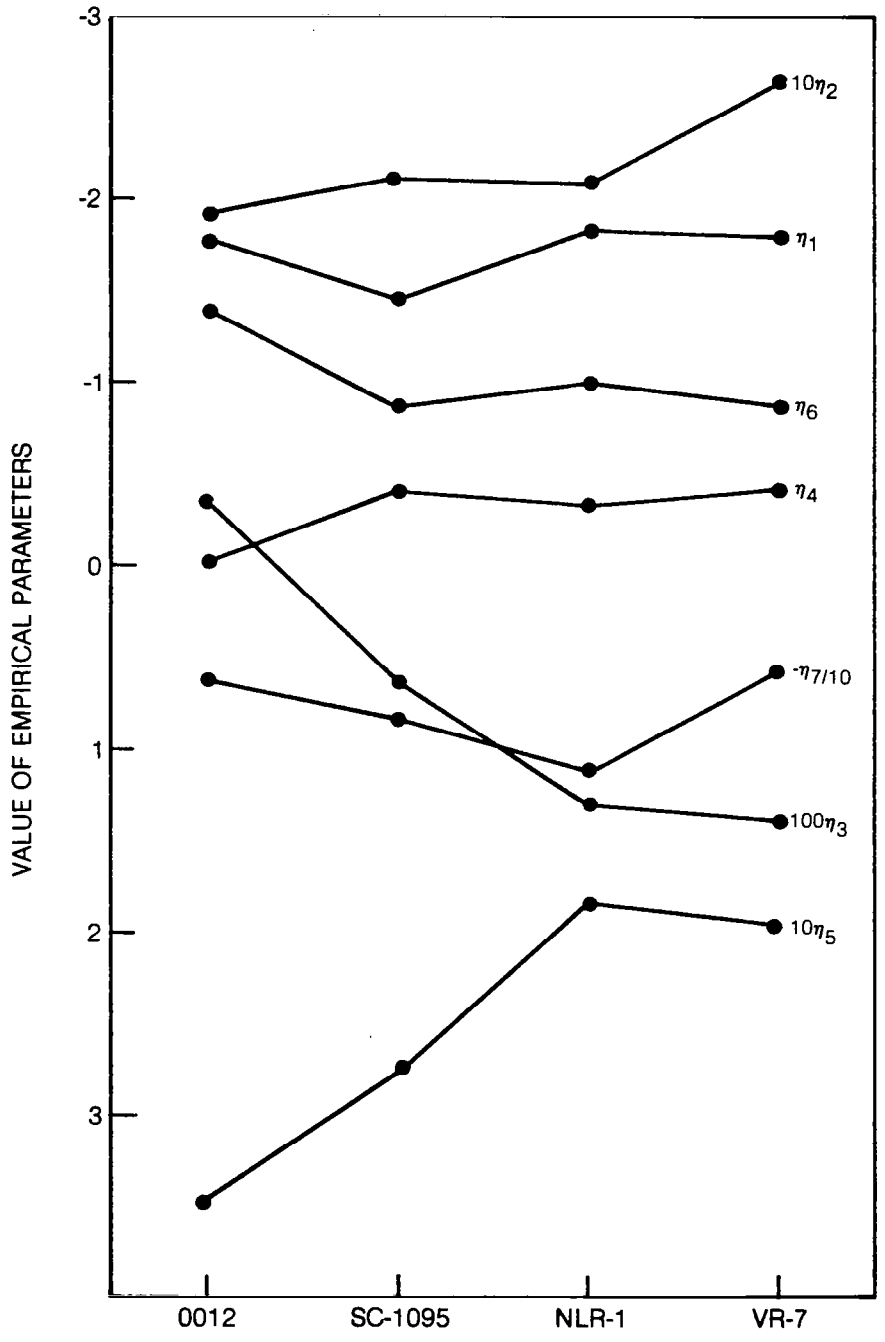

Figure 33. Variation of Unsteady Pitching Moment Empirical Parameters with Airfoil ($M = 0.3$, $R_n = 3.8 \times 10^6$)

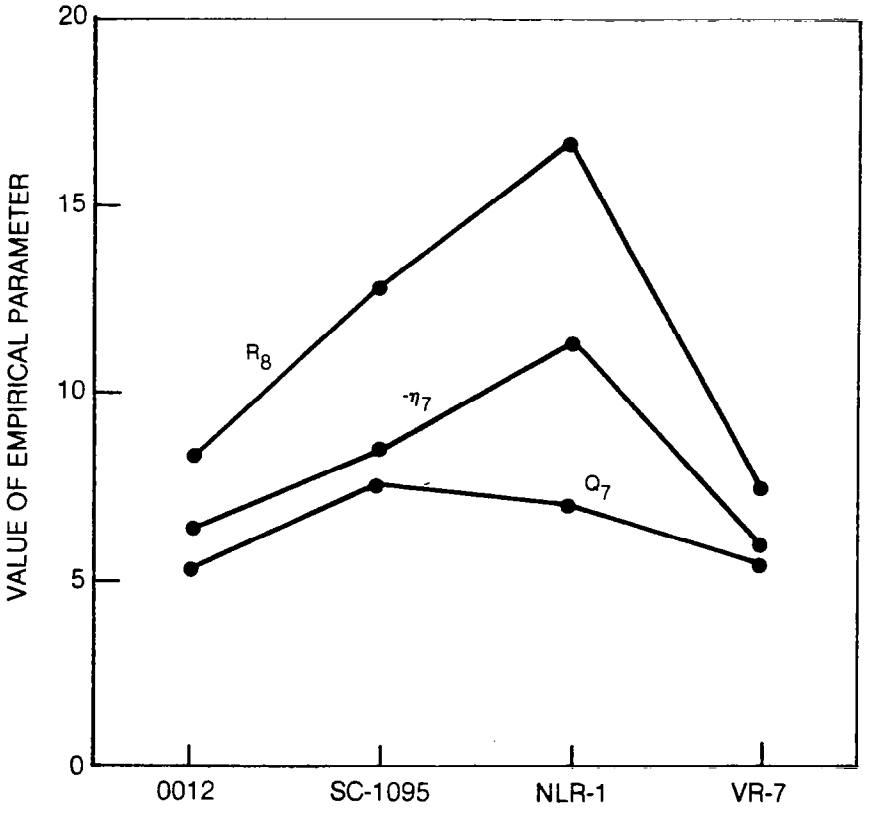

Figure 34. Variation of Leading Edge Stall Vortex-Related Empirical Parameters with Airfoil ($M = 0.3$, $R_n = 3.8 \times 10^6$)

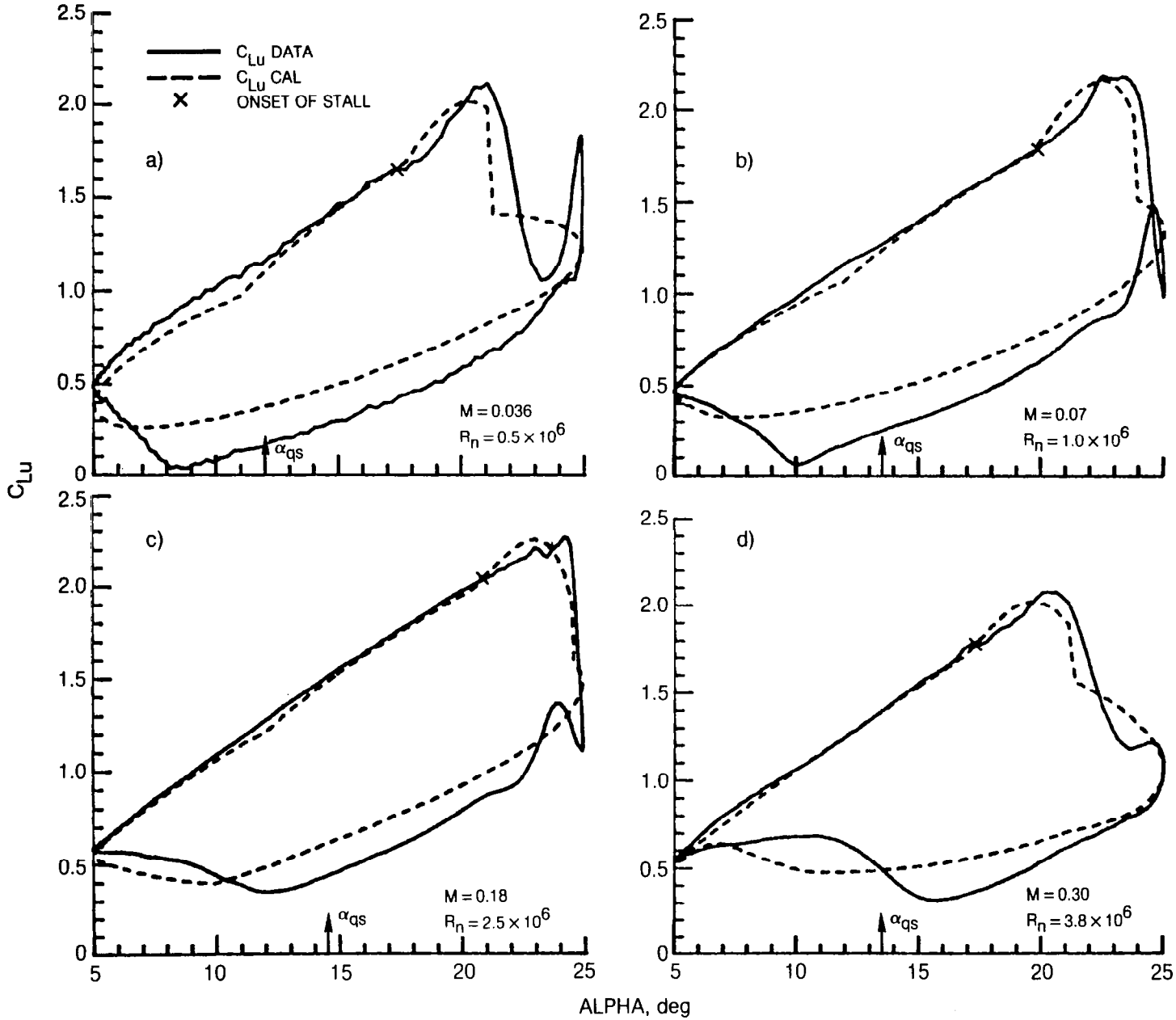

Figure 35. Variation of Unsteady C_{Lu} with Mach Number and Reynolds Number NACA 0012, $\alpha_o = 15$ deg, $\bar{\alpha} = 10$ deg, k = 0.1

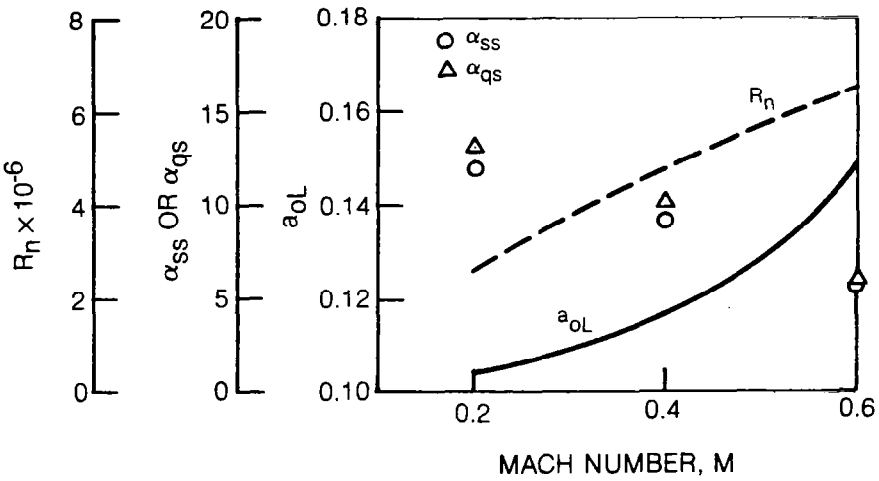

Figure 36. Variation of Static Airfoil Characteristics and Reynolds Number with Mach Number, V0012 Airfoil

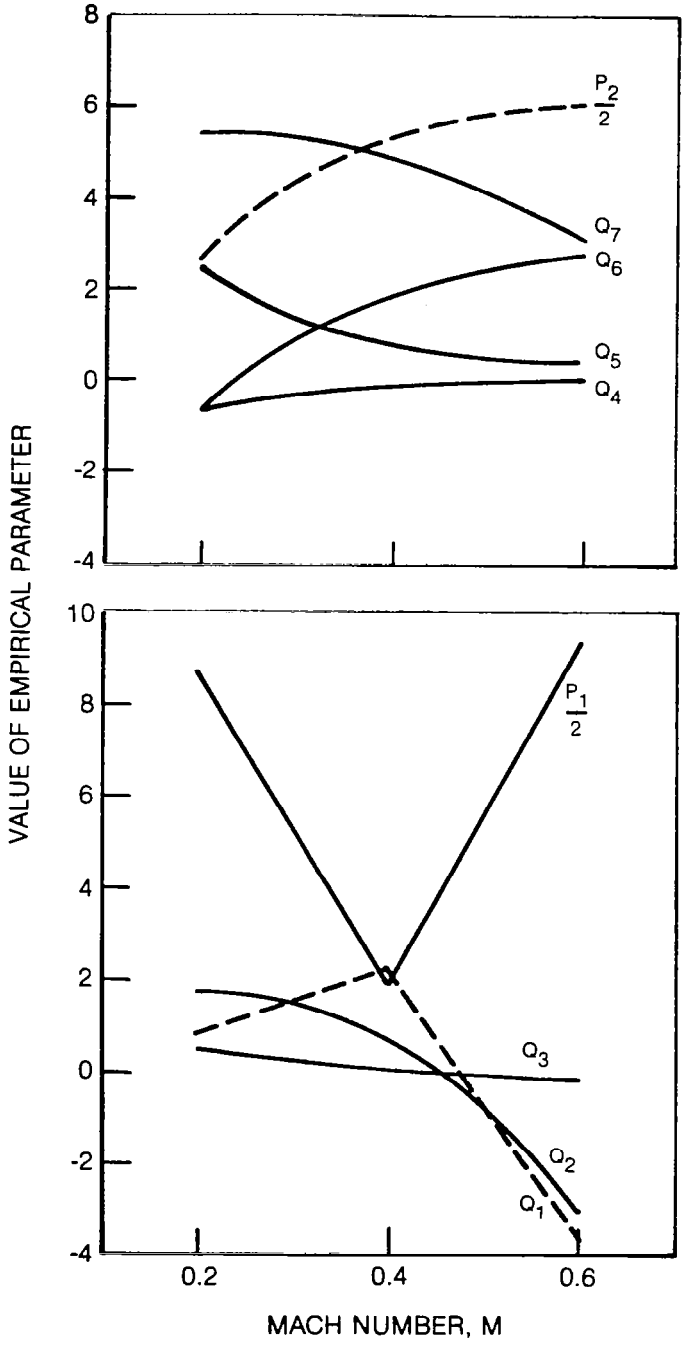

Figure 37. Variation of Unsteady Lift Empirical Parameters with Mach Number and Reynolds Number, V0012 Airfoil

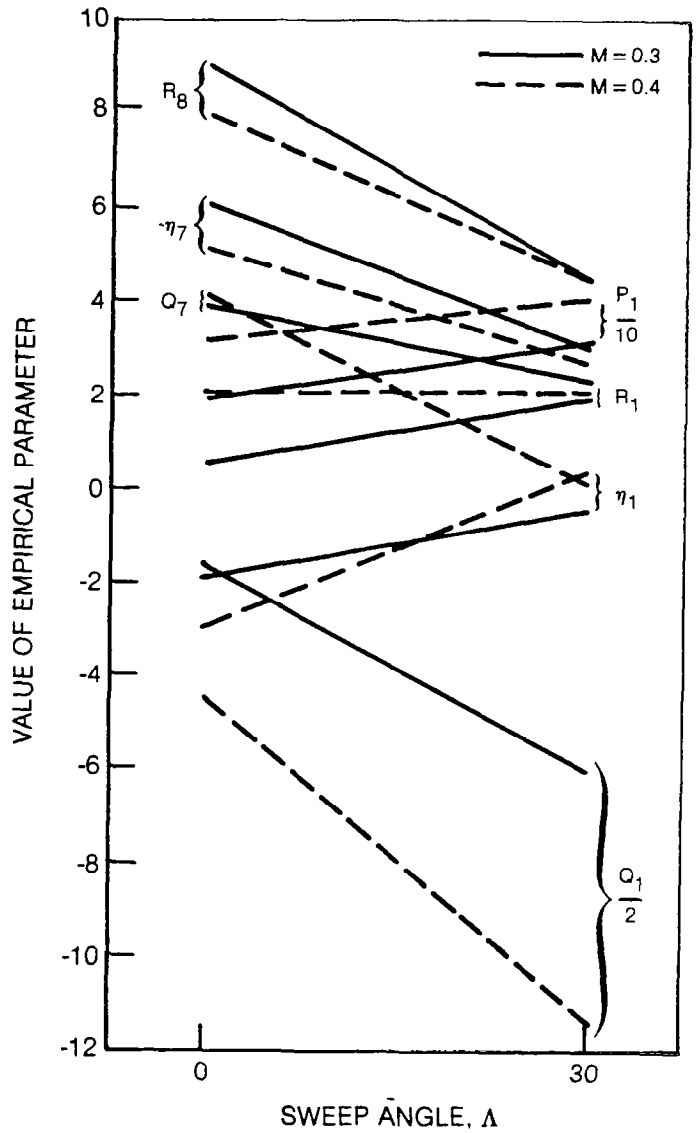

Figure 38. Variation of Unsteady Empirical Parameters with Aerodynamic Sweep (NACA 0012, Data Set Nos. 12-14)

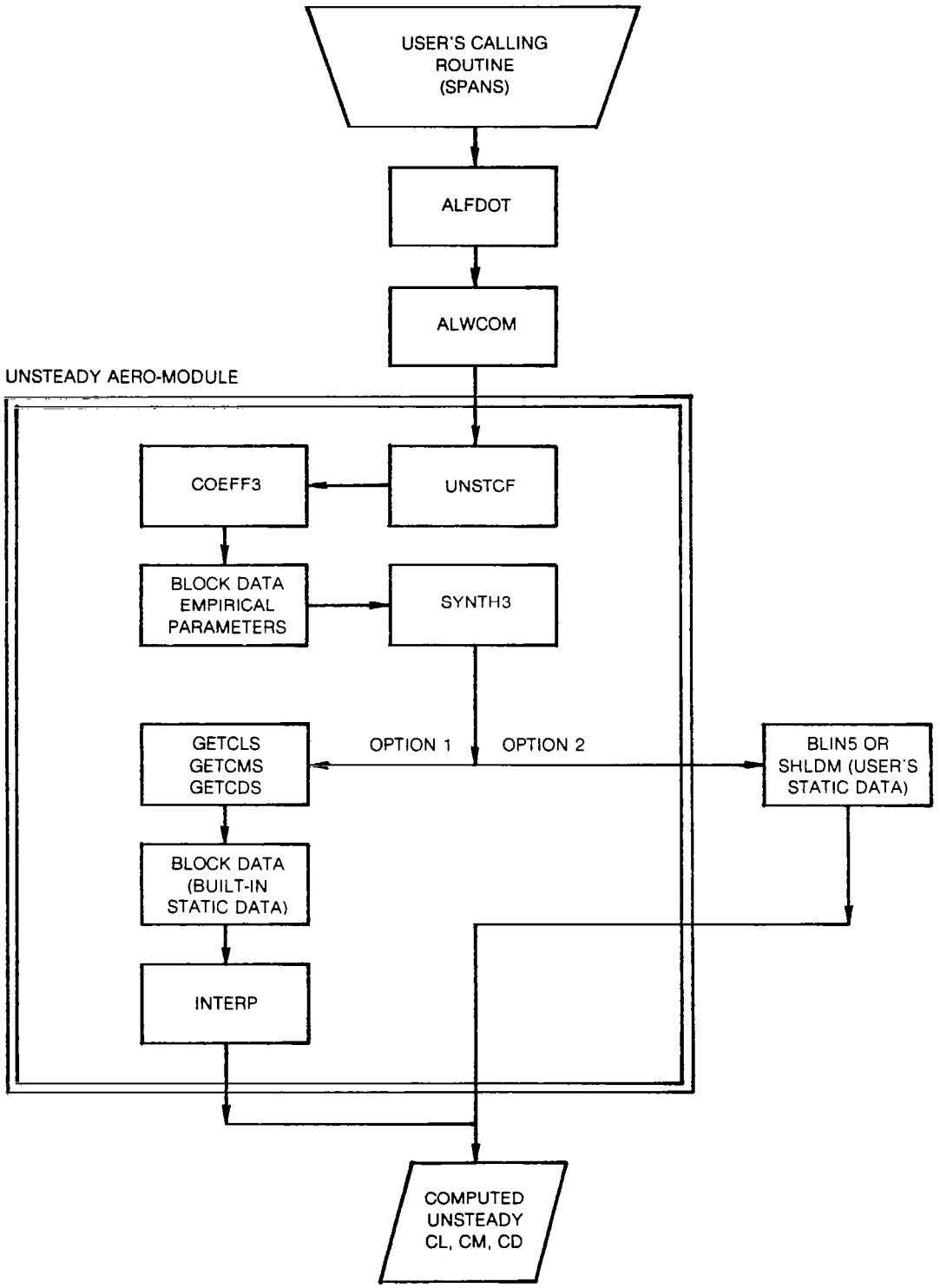

Figure 39. Order of Subroutine Calls for Computation of Unsteady Aerodynamic Coefficients Utilizing UTRC's Synthesized Data Method

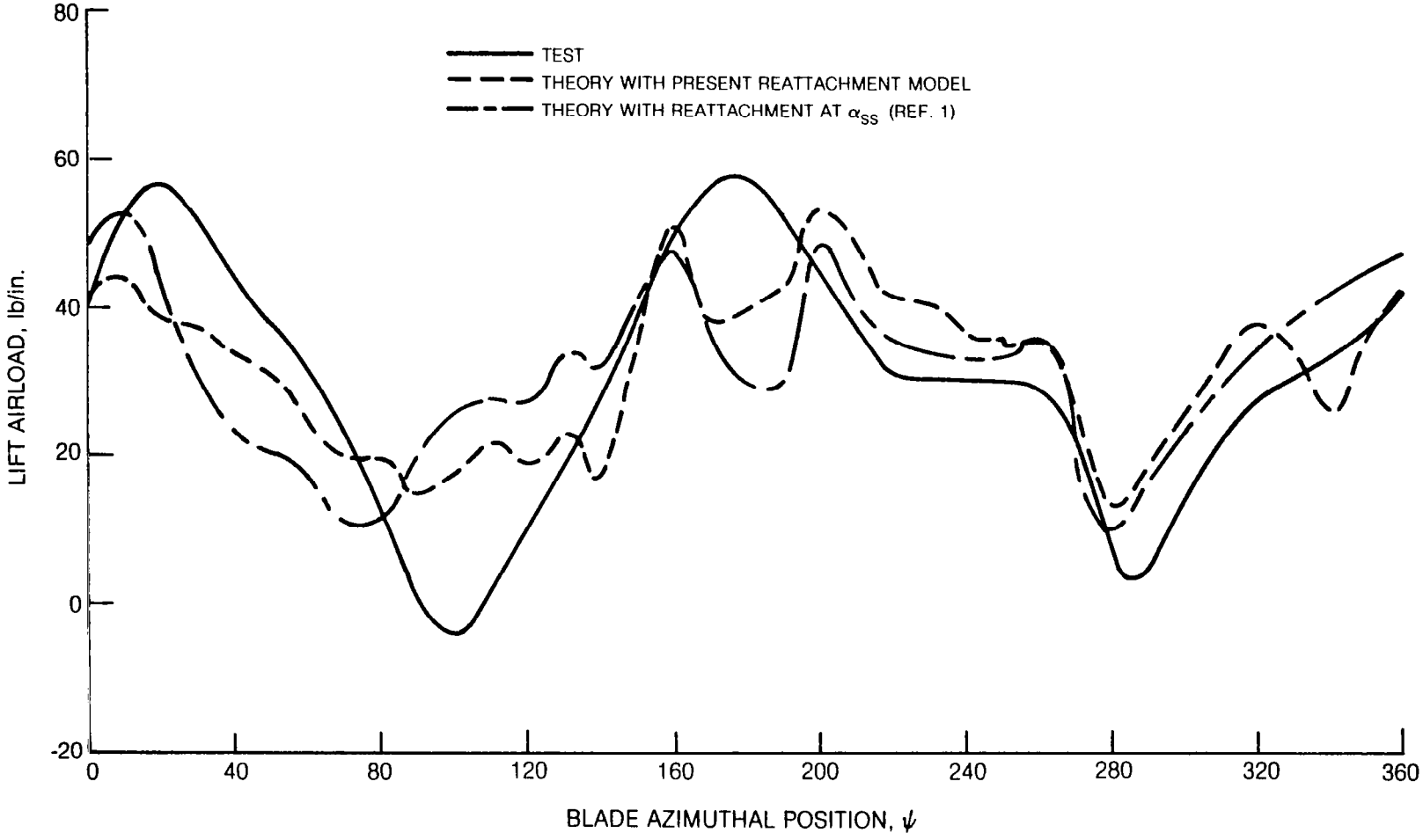

Figure 40. Correlation Between Calculated and Test Airloads at r/R = 0.75, CH-53A Blade for Case 52 (Thrust = 41,000 lbs, $\mu = 0.327$)

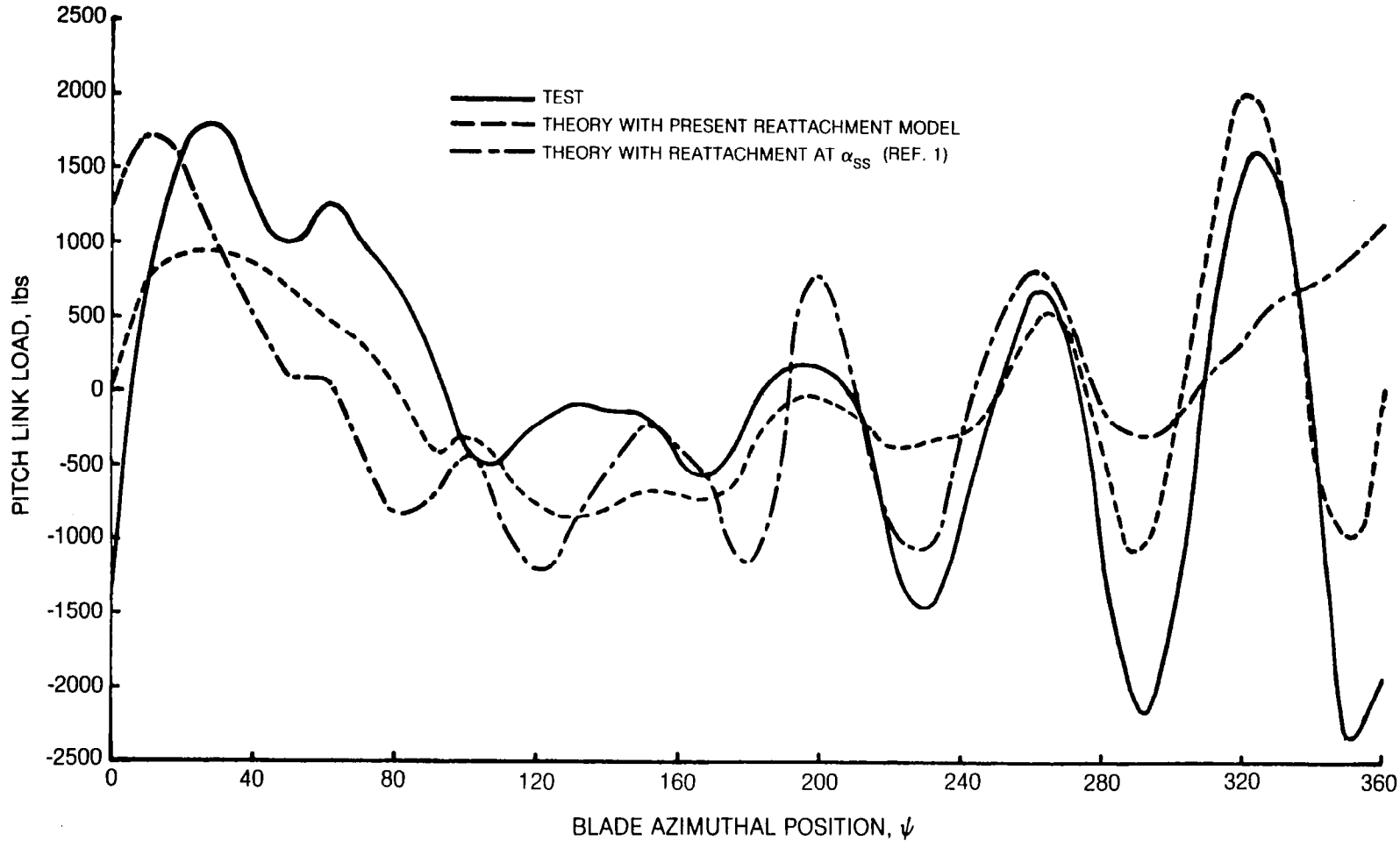

Figure 41. Correlation Between Calculated and Test Pitch Link Loads CH-53A Blade for Case 52 (Thrust = 41,000 lbs, $\mu = 0.327$)

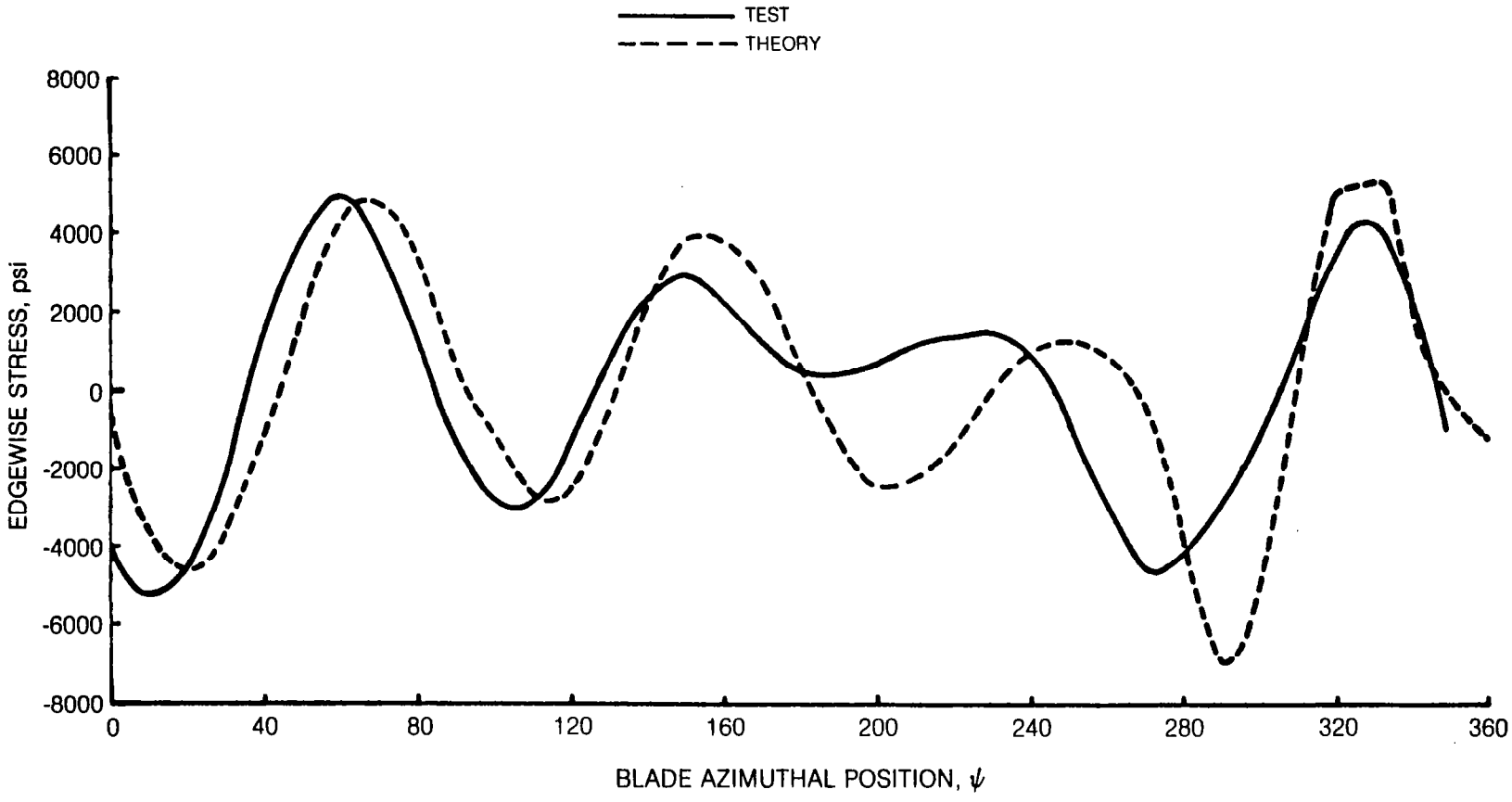

Figure 42a. Correlation between Calculated and Test Edgewise Stresses at r/R = 0.49 CH-53A Blade for Case 52 (Thrust = 41,000 lbs, $\mu = 0.327$)

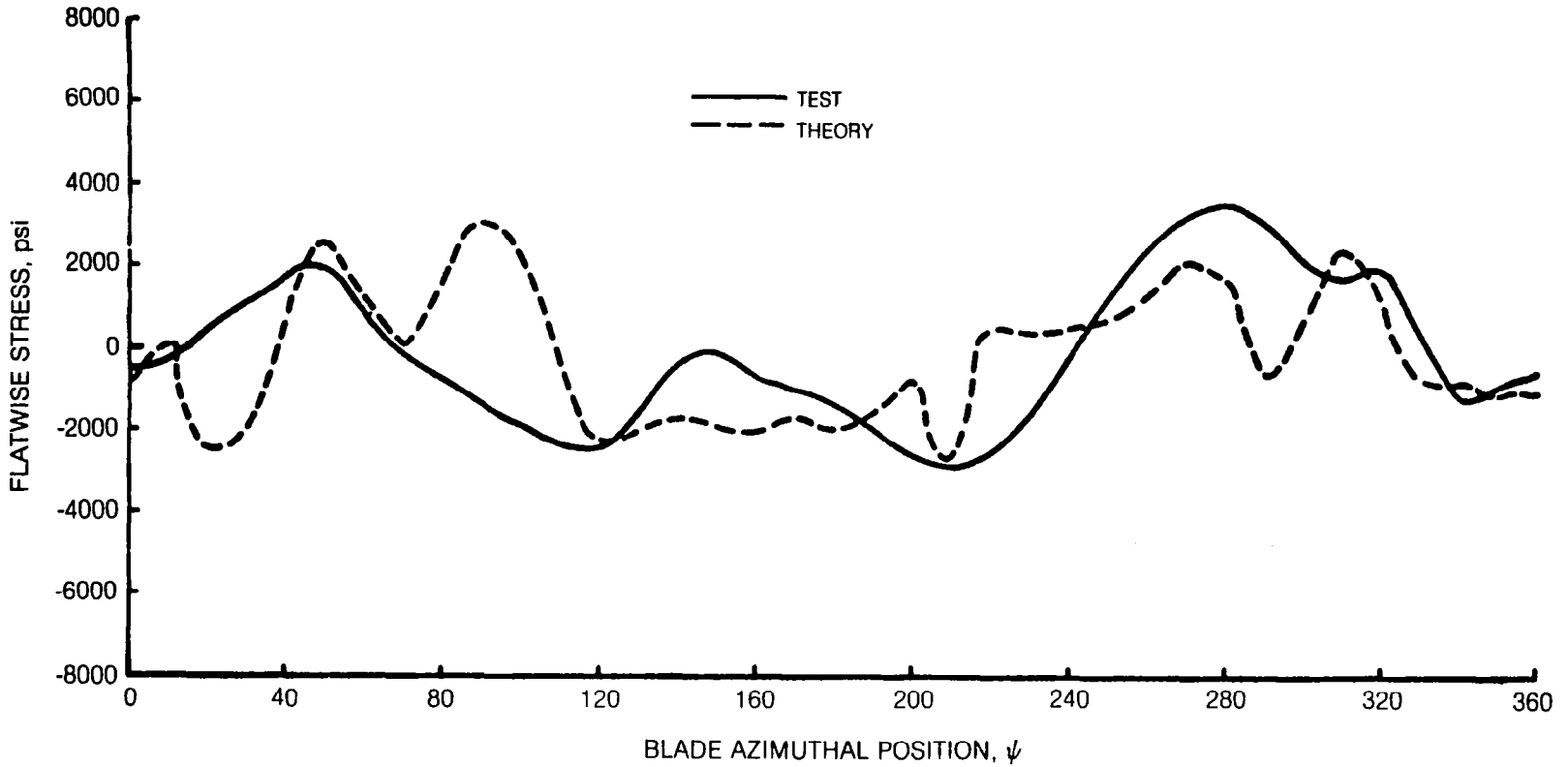

Figure 42b. Correlation between Calculated and Test Flatwise Stresses at r/R = 0.49 CH-53A Blade for Case 52 (Thrust = 41,000 lbs, $\mu = 0.327$)

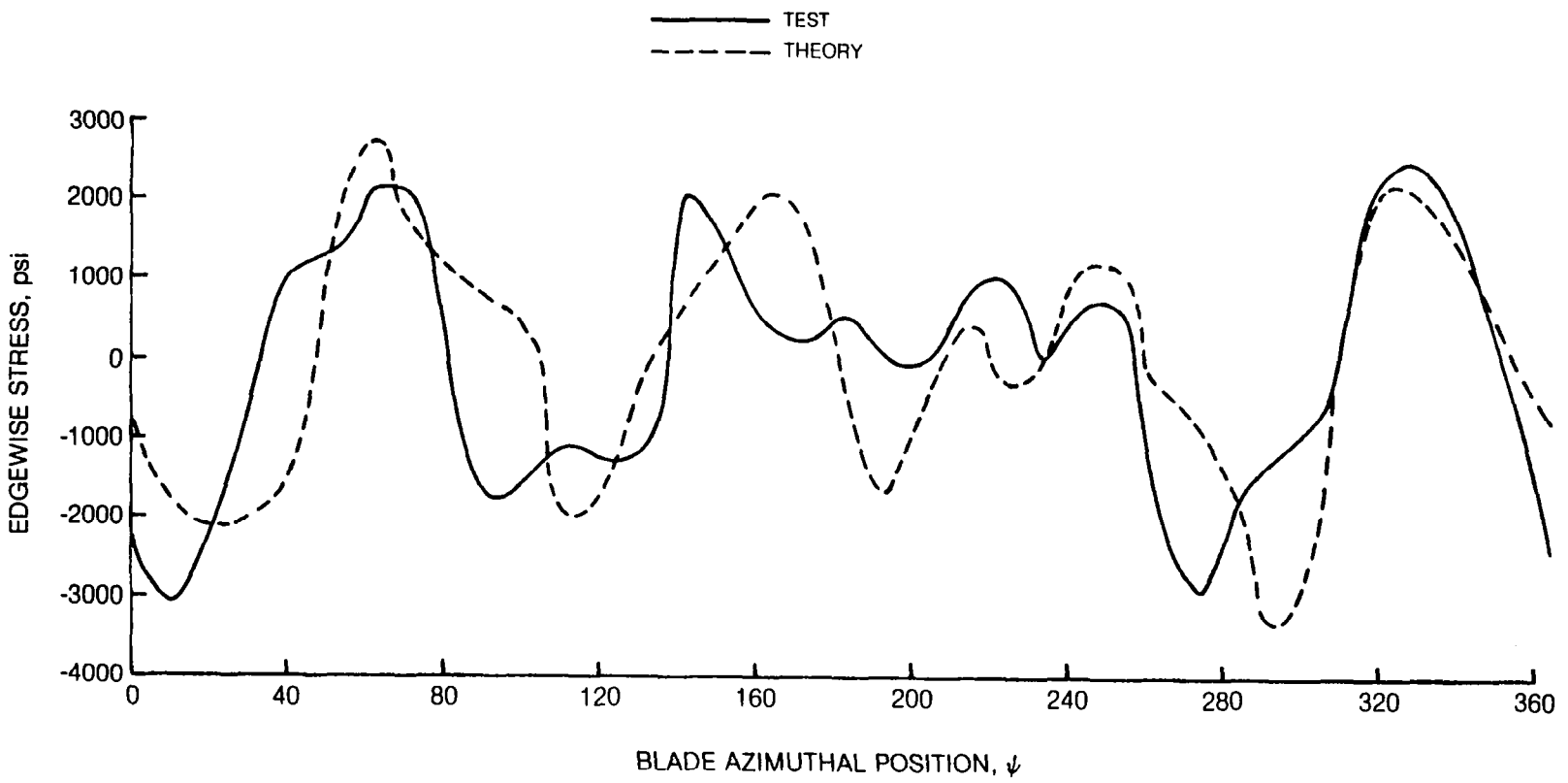

Figure 43a. Correlation between Calculated and Test Edgewise Stresses at r/R = 0.79 CH-53A Blade for Case 52 (Thrust = 41,000 lbs, $\mu = 0.327$)

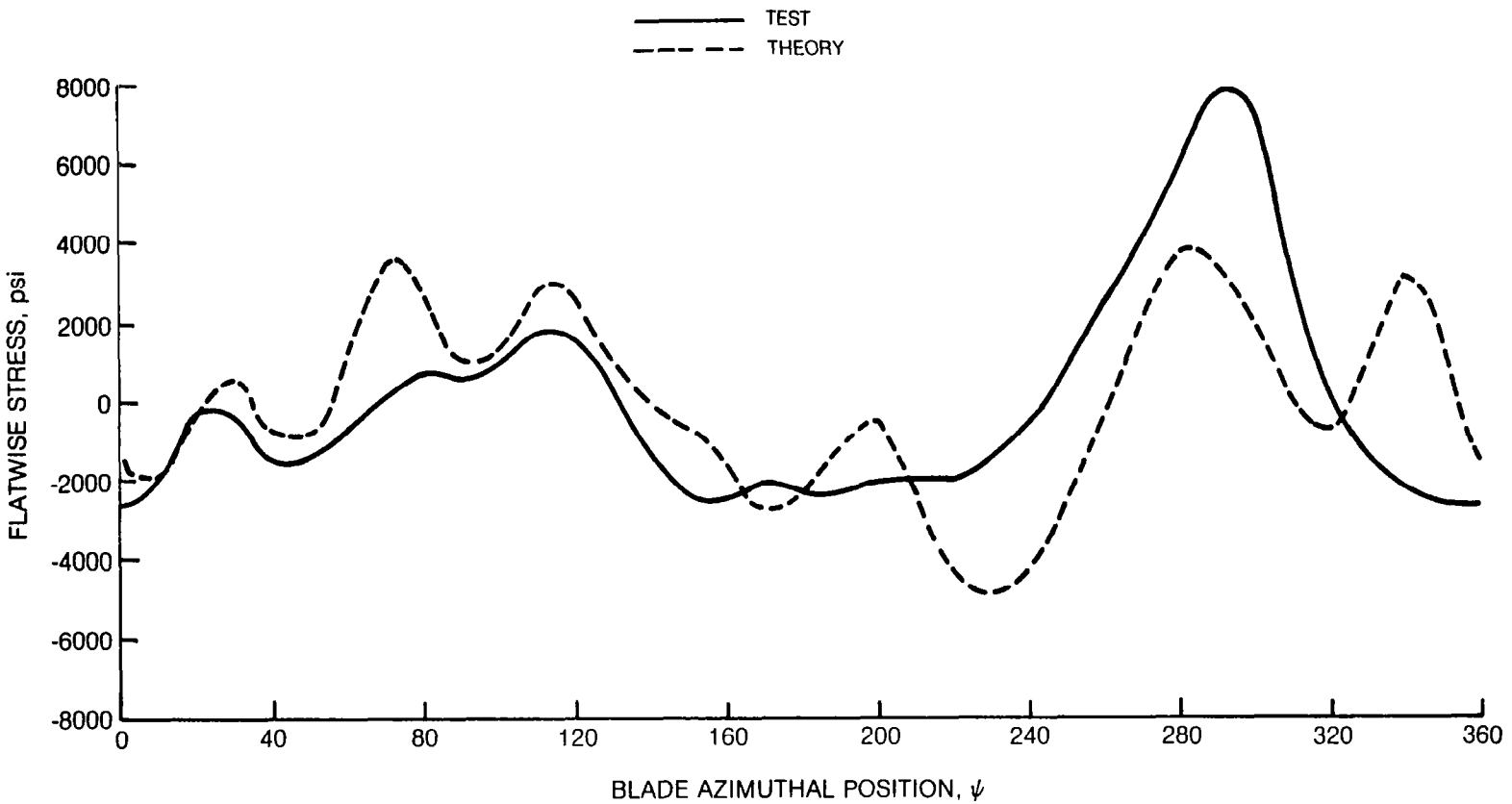

Figure 43b. Correlation between Calculated and Test Flatwise Stresses at r/R = 0.79 CH-53A Blade for Case 52 (Thrust 41,000 lbs, $\mu = 0.327$)

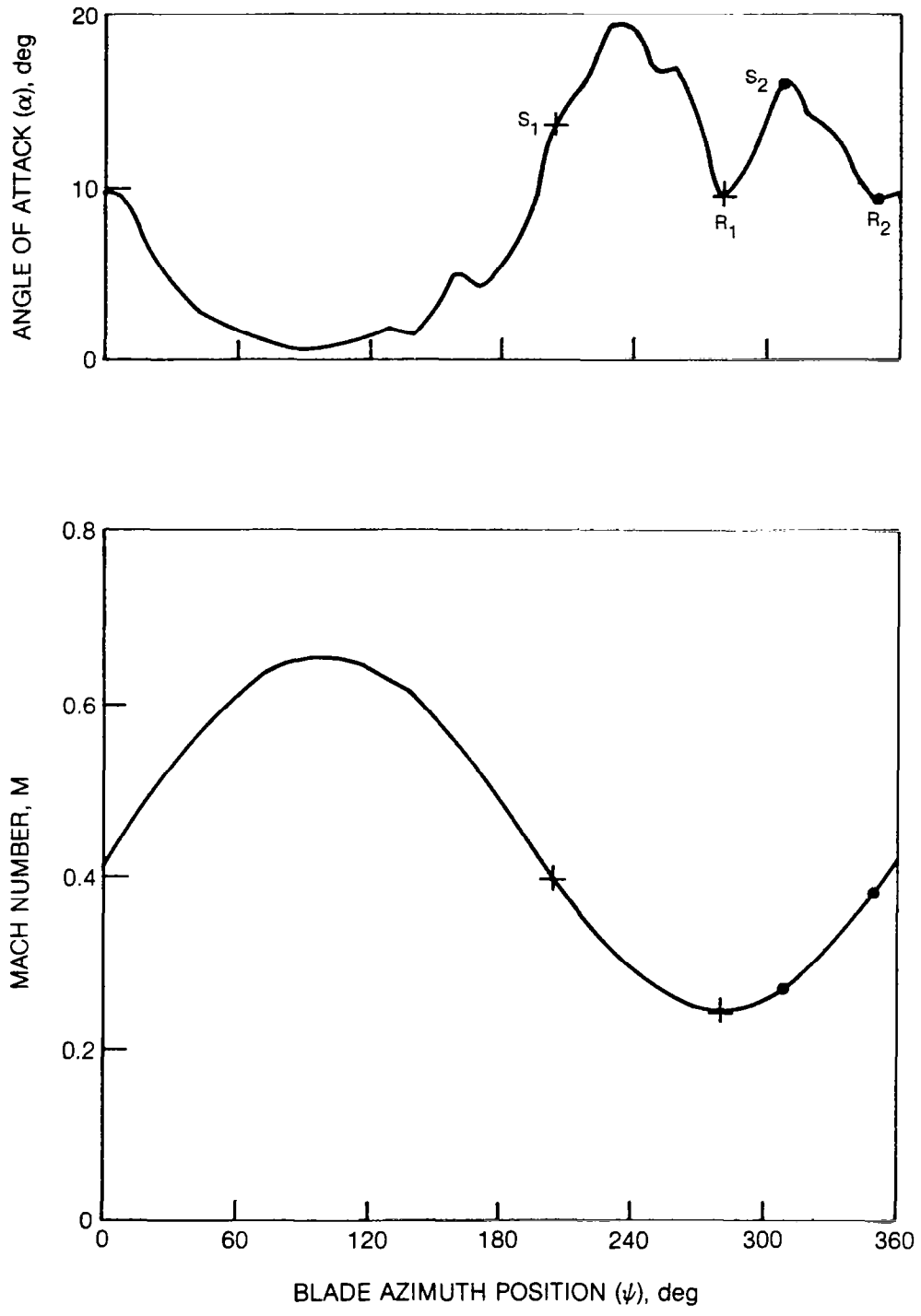

Figure 44. Azimuthal Variation of Computed CH-53A Blade Section (r/R = 0.7) Aerodynamic Parameters. $CT/\sigma = 0.083$, $\mu = 0.327$, $\alpha_s = -2.5$ (Case 52 in Ref. 17)

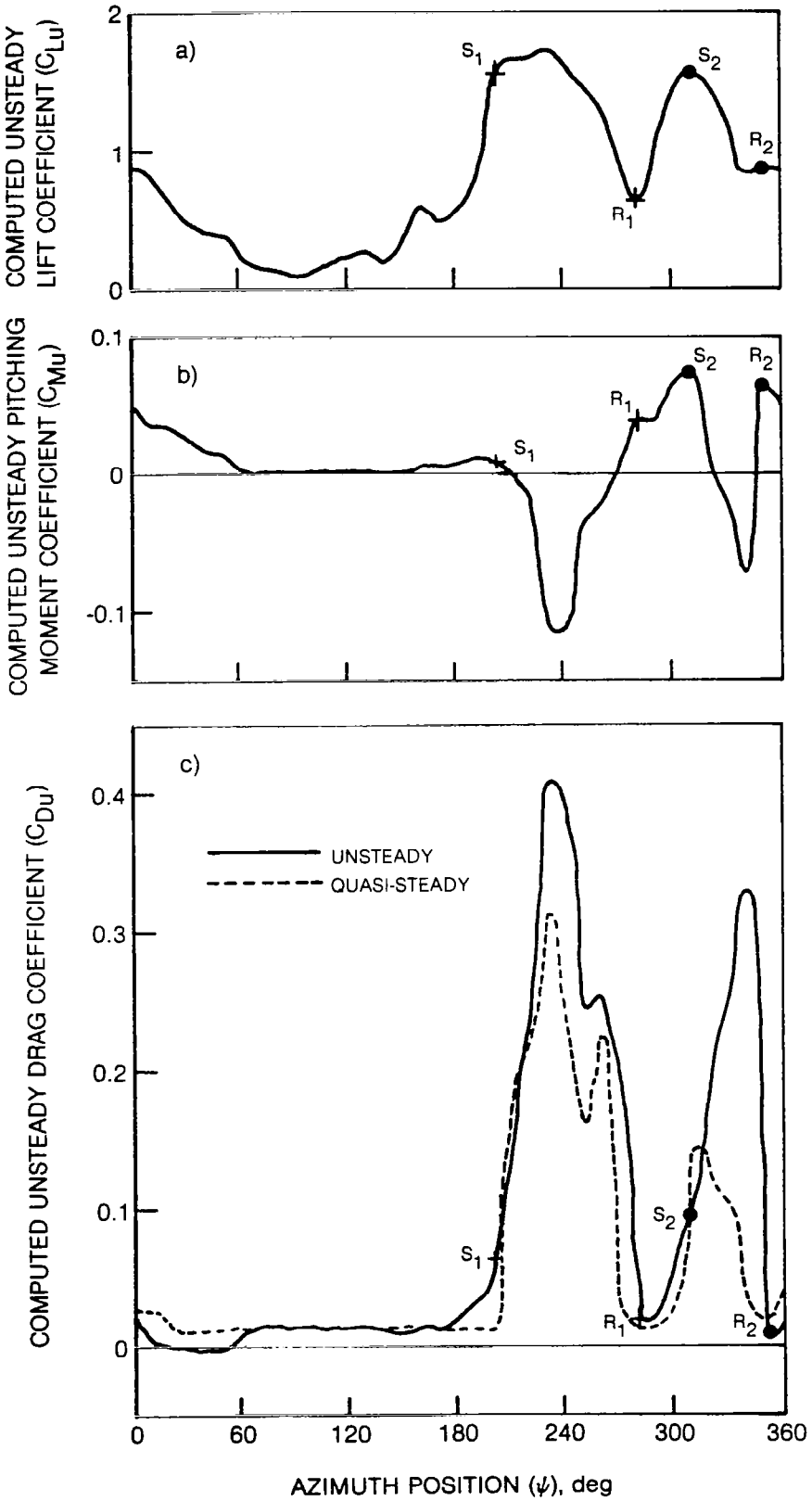

Figure 45. Predicted CH-53A Blade Section (r/R = 0.7) Characteristics. $CT/\sigma = 0.083$, $\mu = 0.327$, $\alpha_s = -2.5$ (Case 52 in Ref. 17)

APPENDIX A

COMPUTATION OF PARAMETER α_w

Applying the convolution theorem (Ref. 19) to Eq. (1), the Laplace transform of Eq. (1) is

$$\tilde{\alpha}_E(\tau) = \tilde{\phi}_c(\tau) \cdot \tau\, \tilde{\alpha}(\tau) \tag{A-1}$$

In the above equation "$\sim$" denotes the Laplace transform defined as follows

$$\tilde{\zeta}(\tau) \equiv \int_0^\infty \zeta(s)\, e^{-\tau s}\, ds \tag{A-2}$$

Taking the Laplace transform of Eq. (4), we obtain

$$\tilde{\phi}_c = \frac{1}{\sqrt{1-M^2}} \left[\frac{1}{\tau} - \frac{A_1}{b_1+\tau} - \frac{A_2}{b_2+\tau} \right] \tag{A-3}$$

where

$$A_1 = 0.165 \tag{A-4}$$

$$A_2 = 0.335 \tag{A-5}$$

$$b_1 = 0.0455\,(1-M^2) \tag{A-6}$$

$$b_2 = 0.3000\,(1-M^2) \tag{A-7}$$

Combining Eqs. (A-1) and (A-3), we get

$$\sqrt{1-M^2}\ \ \tilde{\alpha}_E(\tau) = \left(1.0 - \frac{A_1\tau}{b_1+\tau} - \frac{A_2\tau}{b_2+\tau}\right) \tilde{\alpha}(\tau) \tag{A-8}$$

By definition (also see Eq. (3) for the case of M = 0.0), we have

$$\tilde{\alpha}_w \equiv \tilde{\alpha} - \sqrt{1-M^2}\ \tilde{\alpha}_E \tag{A-9}$$

Or, from Eq. (A-8), we have

$$\tilde{\alpha}_w = \frac{A_1\tau}{b_1+\tau}\ \tilde{\alpha} + \frac{A_2\tau}{b_2+\tau}\ \tilde{\alpha} \tag{A-10}$$

Now let

$$\tilde{x} = \frac{A_1\tau}{b_1+\tau}\ \tilde{\alpha} \tag{A-11}$$

$$\tilde{y} = \frac{A_2\tau}{b_2+\tau}\ \tilde{\alpha} \tag{A-12}$$

Then Eq. (A-10) becomes

$$\tilde{\alpha}_w = \tilde{x} + \tilde{y} \tag{A-13}$$

Next, Eq. (A-11) can be rewritten

$$\tau\tilde{x} + b_1\,\tilde{x} = A_1\,\tau\tilde{\alpha} \tag{A-14}$$

Taking the inverse Laplace transform of Eq. (A-14) gives the following first order differential equation for X,

$$\frac{dx}{ds} + b_1 x = A_1 \frac{d\alpha}{ds} \tag{A-15}$$

Applying the similar procedure to Eq. (A-12), we have

$$\frac{dy}{ds} + b_2 y = A_2 \frac{d\alpha}{ds} \tag{A-16}$$

The inverse transform of Eq. (A-13), along with the appropriate solution of Eqs. (A-15) and (A-16) are used to compute the parameter α_w.

The homogeneous solution (X_h) of Eq. (A-15) is

$$x_h = c_1 e^{-b_1 s} \tag{A-17}$$

and if the particular solution (X_p) of Eq. (A-15) is assumed to be

$$x_p = D(s)\, e^{-b_1 s} \tag{A-18}$$

then by variation of parameters (Ref. 19), we have

$$e^{-b_1 s} \frac{d}{ds}\left[D(s)\right] = A_1 \frac{d}{ds}(\alpha) \tag{A-19}$$

or

$$D(s) = \int_0^s A_1 \left(\frac{d\alpha}{du}\right) e^{b_1 u}\, du \tag{A-20}$$

Therefore, the general solution of Eq. (A-15) is

$$x = e^{-b_1 s}\left[c_1 + \int_0^s A_1 e^{b_1 u}\frac{d\alpha}{du}\,du\right] \tag{A-21}$$

Sinusoidal Airfoil Oscillations

For the sinusoidally oscillating airfoil, we have

$$\alpha = \alpha_0 + \bar{\alpha}\,\sin ks \tag{A-22}$$

or

$$\frac{d\alpha}{ds} = k\bar{\alpha}\,\cos ks \tag{A-23}$$

Substitution of above expression for $d\alpha/ds$ in Eq. (A-21) and evaluation of the resulting integral gives

$$x = c_1 e^{-b_1 s} + A_1\left[\frac{b_1 k\,\bar{\alpha}\cos ks}{k^2 + b_1^2} + \frac{k^2\bar{\alpha}\,\sin ks}{k^2 + b_1^2}\right] \tag{A-24}$$

Since data from the oscillating airfoil tests are normally obtained after all the transients have died out, the first term in Eq. (A-24) is essentially equal to zero. Thus,

$$x = \frac{A_1 b_1}{k^2 + b_1^2}\,k\bar{\alpha}\cos ks + \frac{A_1 k^2}{k^2 + b_1^2}\,\bar{\alpha}\sin ks \tag{A-25}$$

Similarly, the solution of Eq. (A-16) is

$$y = \frac{A_2 b_2}{k^2 + b_2^2}\,k\bar{\alpha}\cos ks + \frac{A_2 k^2}{k^2 + b_2^2}\,\bar{\alpha}\sin ks \tag{A-26}$$

Therefore, from Eq. (A-13), we have

$$\alpha_w = \gamma_1(k,M)\ k\bar{\alpha}\cos ks + \gamma_2(k,M)\ \bar{\alpha}\sin ks \tag{A-27}$$

with

$$\gamma_1(k,M) = \frac{A_1 b_1}{k^2+b_1^2} + \frac{A_2 b_2}{k^2+b_2^2} \tag{A-28}$$

and

$$\gamma_2(k,M) = \frac{A_1 k^2}{k^2+b_1^2} + \frac{A_2 k^2}{k^2+b} \tag{A-29}$$

Nonsinusoidal Airfoil Oscillations

For the nonsinusoidal case (for example, the rotor blade), the parameter α_w is computed numerically. The homogeneous solution (Eq. (A-17)) and the particular solution (Eq. (A-18)) at step n are given by

$$(x_h)_n = (x_h)_{n-1}\, e^{-b_1(s_n - s_{n-1})} \tag{A-30}$$

$$(x_p)_n = D\,(s_n)\, e^{-b_1 s_n} \tag{A-31}$$

If step size $(s_n - s_{n-1})$ is small enough, then by Taylor series expansion, we have

$$(x_p)_n = \left[D(s_{n-1}) + \frac{dD}{ds}\bigg|_{s_n}(s_n - s_{n-1})\right]\ e^{-b_1 s_n} \tag{A-32}$$

Use of Eq. (A-19) in the above equation gives

$$(x_p)_n = (x_p)_{n-1} e^{-b_1 (s_n - s_{n-1})} + A_1 \quad (\alpha_n - \alpha_{n-1}) \tag{A-33}$$

Therefore, if we combine Eqs. (A-30) and (A-33), we have

$$(x)_n = (x)_{n-1} e^{-b_1 (s_n - s_{n-1})} + A_1 (\alpha_n - \alpha_{n-1}) \tag{A-34}$$

Similarly,

$$(Y)_n = (Y)_{n-1} e^{-b_2 (s_n - s_{n-1})} + A_2 (\alpha_n - \alpha_{n-1}) \tag{A-35}$$

Finally, we have

$$(\alpha_w)_n = (x)_n + (Y)_n \tag{A-36}$$

APPENDIX B

DERIVATION OF EQUATIONS FOR α_{Dm}

The general relationship governing the dynamic stall has been expressed as (Eq. (17))

$$\alpha_{Em} = F\ (\alpha_{ss},\ A_m,\ \alpha_{Dm}) \tag{B-1}$$

Or from Eq. (3),

$$\alpha_{Dm} - \alpha_{wm} = F\ (\alpha_{ss},\ A_m,\ \alpha_{Dm}) \tag{B-2}$$

The above equation implies that the dynamic stall angle has been assumed to vary as follows

$$\alpha_{Dm} = \zeta\ (\alpha_{ss},\ A_m,\ \alpha_{wm}) \tag{B-3}$$

Next, consider a dynamic condition where the reduced frequency is very small (quasi-steady), and the corresponding dynamic parameters at stall are A_{mo} and α_{wmo}.

Using the two-dimensional Taylor formula for expansion around quasi-steady conditions, and retaining only the linear terms, it follows

$$\begin{aligned}\alpha_{Dm} = \zeta\ (\alpha_{ss},\ A_{mo},\ \alpha_{wmo}) + (A - A_{mo})\ \frac{\partial \zeta}{\partial A_m}\ (\alpha_{ss},\ A_{mo},\ \alpha_{wmo}) \\ + (\alpha_{wm} - \alpha_{wmo})\ \frac{\partial \zeta}{\partial \alpha_{wm}}\ (\alpha_{ss},\ A_{mo},\ \alpha_{wmo})\end{aligned} \tag{B-4}$$

Now, if we let the reduced frequency tend to zero (quasi-steady case) we have both A_{mo} and α_{wmo} going to zero. Also, $\zeta(\alpha_{ss},\ A_{mo},\ \alpha_{wmo})$ goes to quasi-steady stall angle or α_{qs}. Thus, we get

$$\alpha_{Dm} = \alpha_{qs} + \bar{C}_A\ A_m + \bar{C}_w\ \alpha_{wm} \tag{B-5}$$

Here we have

$$\bar{C}_A = \frac{\partial \zeta}{\partial A_m} (\alpha_{ss}, A_{mo}, \alpha_{wmo}) \tag{B-6}$$

and

$$\bar{C}_w = \frac{\partial \zeta}{\partial \alpha_{wm}} (\alpha_{ss}, A_{mo}, \alpha_{wmo}) \tag{B-7}$$

The parameters α_{qs}, $\bar{C}_A$ and $\bar{C}_w$ depend on only the steady state or quasi-steady characteristics of an airfoil and in general vary with Mach number, Reynolds number, sweep angle and airfoil shape. Finally, for convenience, Eq. (B-5) is rewritten in the following form (also see Eq. (18))

$$\alpha_{Dm} = (1 + \epsilon + C_{Am} A_m + C_{wm} \alpha_{wm}) \alpha_{ss} \tag{B-8}$$

The comparison of Eq. (B-8) with Eq. (B-5) gives

$$\epsilon = (\alpha_{qs} - \alpha_{ss}) / \alpha_{ss} \tag{B-9}$$

1. Report No.	2. Government Accession No.	3. Recipient's Catalog No.
NASA CR-3672		

4. Title and Subtitle	5. Report Date
SYNTHESIZED AIRFOIL DATA METHOD FOR PREDICTION OF DYNAMIC STALL AND UNSTEADY AIRLOADS	February 1983
	6. Performing Organization Code
7. Author(s)	8. Performing Organization Report No.
Santu T. Gangwani	
	10. Work Unit No.
9. Performing Organization Name and Address	
United Technologies Research Center 400 Main Street East Hartford, CT 06108	11. Contract or Grant No. NAS1-16803
	13. Type of Report and Period Covered Contractor Report
12. Sponsoring Agency Name and Address	
National Aeronautics and Space Administration Washington, DC 20546 and U.S. Army Aviation Research and Development Command St. Louis, MO 63166	14. Army Project No. 1L161102AH45 NASA Code 505-42-23-06

15. Supplementary Notes

Technical Monitor for Langley Research Center (Structures Laboratory) was Warren H. Young, Jr. Monitor at Ames Research Center (Aeromechanics Laboratory) was H. Andrew Morse.

16. Abstract

A detailed analysis of dynamic stall experiments has led to a set of relatively compact analytical expressions, called synthesized unsteady airfoil data, which accurately describe in the time-domain the unsteady aerodynamic characteristics of stalled airfoils. An analytical research program was conducted to expand and improve this synthesized unsteady airfoil data method using additional available sets of unsteady airfoil data. The primary objectives were to reduce these data to synthesized form for use in rotor airload prediction analyses and to generalize the results.

Under the present study, unsteady drag data were synthesized which provided the basis for successful expansion of the formulation to include computation of the unsteady pressure drag of airfoils and rotor blades. Also, an improved prediction model for airfoil flow reattachment was incorporated in the method. Application of this improved unsteady aerodynamics model has resulted in an improved correlation between analytic predictions and measured full scale helicopter blade loads and stress data.

17. Key Words (Suggested by Author(s))	18. Distribution Statement
Unsteady Aerodynamics Airfoil Aerodynamics Rotor Aeroelasticity Rotor Aerodynamics	FEDD Distribution Subject Category 02

19. Security Classif. (of this report)	20. Security Classif. (of this page)	21. No. of Pages	22. Price*
Unclassified	Unclassified	136	